UNIVERSITY OF PADUA
DEPARTMENT OF CIVIL, ENVIRONMENTAL AND ARCHITECTURAL ENGINEERING

Master's degree in environmental engineering
Soil protection and water management

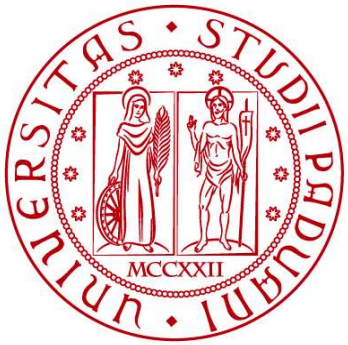

MASTER THESIS

Morphological analysis of an alpine stream using drone photogrammetry

Thesis advisor:

Chiar.mo Prof. Gianluca Botter

Research supervisor:

Dott. Nicola Durighetto

Candidate: Andrea Burbello

Mat: 2010614

ACADEMIC YEAR 2021-2022

Abstract

The morphological analysis of an alpine stream can represent a real challenge, given the geomorphological and hydrological complexity of the area. However it is of fundamental importance as the various topographical characteristics of the main stream and its tributaries provide useful information in order to evaluate phenomena such as runoff, CO_2 emissions and sediment transport.

The survey sites, examined in this thesis work, belong to the Valfredda basin located in the north-east of Italy and include some areas of the main stream and some of its tributaries. The research was conduced under the scope of the "ERC DyNET" (Dynamical river network: climatic controls and biogeochemical function) project.

As a survey methodology, drone photogrammetry was used with the support of a ground GPS antenna in "Cinematic Stop & Go" mode with RTK correction.

The images captured by the drone and the GPS data were processed within Agisoft Metashape in order to obtain a 3D model of the various areas and finally DEM, orthophotos were extracted using the same software and then processed in QGIS for the purpose of an optimal morphological understanding of the area.

The methodologies used made it possible to obtain high-precision models containing morphological data such as slopes and elevations. This confirmed the robustness of the chosen methodology.

Through the use of a Matlab algorithm it was possible to identify the steps in the stream beds and their spatial and geometric configuration; making it possible to observe an inverse proportionality between the mean step distance and the slope of the reach under examination. The procedure for determining the steps presents issues linked to the DEM, interference and morphological complexity of mountain torrents, but with appropriate arrangements made during the survey phase the result can be improved.

The results obtained in this thesis refer to the year of the measurement campaigns, thus providing the opportunity to lay the foundations for future comparative studies on the morphology of the area.

Acknowledgements

I use this space to be thank all those people who have allowed me to be here today to achieve this important goal.

In particular, I would like to thank Professor Gianluca Botter, of the Department of Civil and Environmental Engineering, University of Padua, for assigning me this thesis work by accommodating my needs and allowing me to propose ideas for the achievement of the final results.

I would also like to thank Dr. Nicola Durighetto, who supervised me in the survey operations and was always willing to support me, encouraging me to give my best.

I would also like to thank all my colleagues and friends who have eased and made this path of study much more enjoyable, and without them I most likely would not be here today.

A “Thank You” also to my family who allowed me to earn my degree without having to have any thoughts financially and have always been there for me in both the good and bad times of this path.

A “thank you” also goes to my girlfriend who, like my family, has always supported me and stood by me

Index

Figures Index

Tables Index

1. Introduction

This Master's Thesis Project aims to perform the morphological study of some streams of the Valfredda creek and its tributaries for the purpose of the "ERC DyNET" (Dynamical River Network: climatic controls and biogeochemical function) project.

This study is relevant not only for the extrapolation of data regarding the geometry and structure of the area, at the time of the survey, but also for the determination of run-off, CO_2 emission in correspondence of riverbed jumps, solid transport, geomorphological evolution of an area, and all those physical and chemical phenomena that are grounded in morphology. In particular, the alpine environment is highly subject to change due to climatic events, so it is necessary to provide a good basis for the description of the important physical process taking place along the stream to acquire such data with the right degree of precision.

The main focus of this thesis will be to determine the geometry and structure of the area by reporting as significant information the elevations, slopes and number of steps in each of the five reaches placed under observation.

Carozzani A. Master's Thesis ("Quantifying the role of steps in carbon dioxin emission in a mountain headwater stream", 2021) highlights how characterizing the morphology of a watercourse is important for the purpose of assessing CO_2 emissions at the basin scale, as step-pool system may be "invisible" hotspot of CO_2 emission in mountain headwater streams.

An initial brief chapter will give an overview of the study area, providing information regarding the location of the basin and its geological structure, placing special focus on the areas subject to survey.

It will proceed with a theoretical discussion of the methodologies used in the study, in order to motivate the various choices made in the Data Acquisition and Processing procedures.

A survey methodology consisting of 2 phases was employed during the field data acquisition procedure:

- an initial survey devoted to the determination of the Markers on the ground, which is done by means of a GPS antenna used in stop-and-go kinematic mode with RTK signal acquisition from the Permanent GPS Network of the Veneto Region;
- a subsequent aerophotogrammetric acquisition based on SAPR technology, using a multirotor drone.

This combination was chosen because treating vast mountainous areas, such as those involved in this study, with classical topography would require too much time in the data acquisition phase and also field operations would be complicated due to the terrain conformation. The use of GPS and SAPR allows are to move easily between steep slopes and obtain good accuracies in the results.

At the end of the survey operations 3D data will be produced, which are, useful for the construction of three-dimensional models of the areas within the Agisoft Metashape photogrammetric processing software and further products such as Orthophotos, Dem, that allow us to derive the desired morphological information of each area.

Finally, further processing will be carried out in QGIS and MatLab to obtain additional information and graphical outputs to facilitate the representation of the result. Among the information extracted in this last phase the most interesting one is the number of steps-pools present along the various stretches, their location will be investigated through the texture processed in Metashape and DEM, and then the mean step spacing will be plotted in relation to the average slope of the various river rods to verify the goodness of the data obtained.

1.1. Step and pools

Mountain streams are classified based on the work of Montgomery and Buffington (1997) who propose the following subdivision:

- **Waterfalls**: small and large, they are typical of where water flows over a steep rocky substrate.
- **Cascades**: are generally found in spring regions of alpine environments and are therefore mostly associated with small channels. Their slopes range from 3 percent to 20 percent (Montgomery and Buffington, 1997). The bed is formed by thick material that allows the formation of small waterfalls followed by pools. The pattern is characterized by a lack of regular shapes.
- **Steps and pools**: are most often found downstream of the waterfall sections (Montgomery and Buffington, 1997) and are also relatively narrow. They are characterized by regular spacing of pools (varying from 1 to 4 channel widths) and significant variations in water velocity.
- **Shallow and deep rapids:** are characterized by slopes below 4% and by a lack of bedforms such as stone clusters and bars (Turcotte and Morse, 2013).
- **Wandering riffle-pools:** represent the transition between high (riffle segments) and low gradient channels (pool segments). The bed is typically composed of small gravel, with the slope usually varying between 0.3% and 2.0% while the distance between pools can vary from 5 to 7 channel widths. The terminology "wandering" is used to describe the sinuosity of the thalweg, while the channel itself is purely straight.

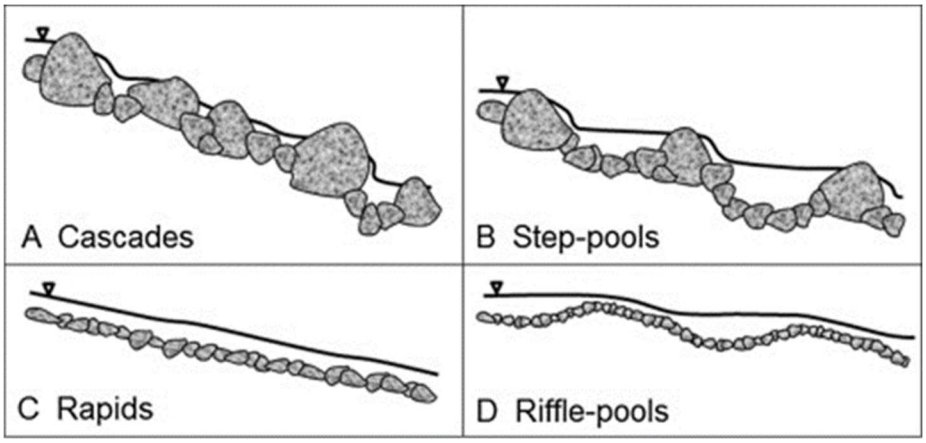

Figure 1: Channel Longitudinal profiles (Turcotte and Morse, 2013)

The configuration of particular interest in this Thesis is the step-pool. This conformation causes channel beds that assume a longitudinal step-pool profile when slopes are in the range of 2% and 20%, where the size of bed materials, including vegetative debris, are found to be larger than the size of the channel (Richardson and Carling, 2021).

Step-pools are found in a wide range of hydroclimatic environments, from wet streams to desert ephemeral systems, also occurring in intermediate semi-arid environments up to the coldest regions of Japan (Chin and Wohl, 2005)

Step-pools consist of relatively large grains accommodated against a "keystone" structure formed by the largest grains available in the channel. The step-pools are modified by infrequent flows that can drag the keystones of the steps, with estimated return intervals of 15-50 years or more. The typical structural conformation, of this geomorphological feature, allows finer material to be stored in the pools and transported as a bedload on rough, stable material that forms a bed during moderate floods (Richardson and Carling, 2021).

Water flows over and through the large elements of roughness that form the steps and then plunges into the pools below, this process causes a distinct decrease in the elevation of the free water surface and creates a tumbling flow in which much of the flow energy is dissipated by eddies. There is an oscillation between subcritical flow in the pool and supercritical flow in the step (Church and Zimmermann, 2007), which reduces the amount of kinetic energy and also potential energy, which if not dissipated would remain available for conversion to kinetic energy, along the longitudinal component, affecting erosion and sediment transport.

Theories on the origin of step-pools can be divided into three main groups:

- Those involving hydraulic control over the position and/or spacing of steps;
- Those that propose substrate control;
- That based on the jammed state hypothesis which proposes a joint bedload and channel width control;

There are also several theories regarding the geometric relationships of step-pools including those that support the following empirical evidence:

- Inverse relationship between step spacing L and channel slope;
- Relationship between step spacing and channel width or to drainage area;
- dependence between step height H and the size of the particles forming the step, which would increase with particle diameter D_k;
- Linear dependence of step height on step spacing;
- Correlation between step height and channel slope;
- Relationship between step spacing and step particle size;

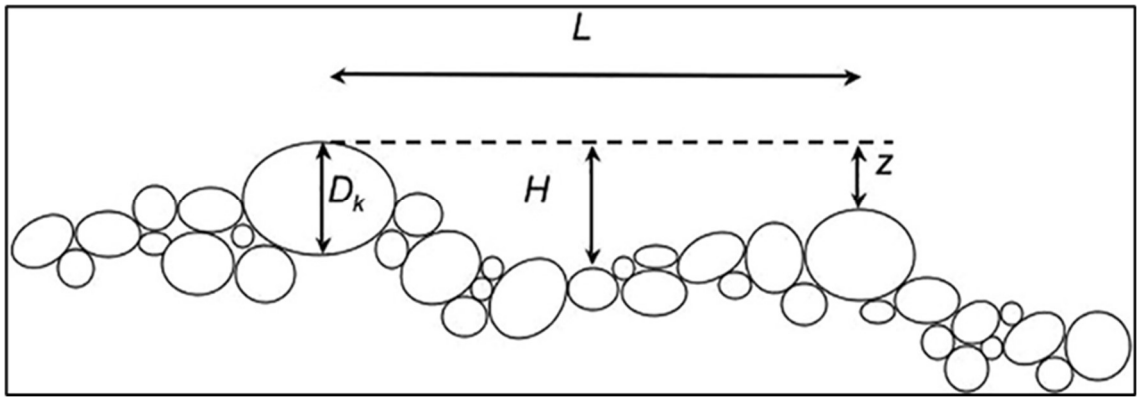

Figure 2: Diagram defining the geometry of the step pool. The stones at each end of the line labeled "L" are keystones (Richardson and Carling, 2021)

Although understanding step-pool geometry has important practical applications in ecological restoration, erosion control, and risk assessment in mountain streams there is, as of today, no complete explanation of the geometric relationships, and the published empirical geometric relationships are highly variable. So the published analysis is insufficient both to fully identify the controls on step-pool geometry and to allow inference of the origin and hydraulic conditions during step formation (Richardson and Carling, 2021).

Chin and Phills (2007) report that Judd (1963) was one of the first to study and document the dominant geometric characteristics of natural step-pool flows. Judd (1964) and Wertz (1966) identified an inverse relationship between step length and channel slope, whereby average step length increases as slope decreases. This trend has been demonstrated for step-pool flows in:

- New Zeland;
- Israel;
- Canada;
- Western United States,

Although the relationship is not always obvious, the initial observation that the frequency of steps-pools increases with increasing slope is to date firmly established and supported by numerous field data sets from around the world.

The spacing between step-pools along a given section is commonly reported to be regular because of the control exerted by channel parameters such as bed slope and grain size. Grant et al. (1990) determined that step-pool spacing was regular within each of 21 step-pool configurations in Oregon, where the average step-pool spacing was 2.56 m. D'Agostino and Lenzi (1997) found an inverse dependence between step-pool spacing and average section slope, using step-pool spacing measurements from nine step-pool configurations in the Rio Cordon, Italy, where the average step spacing was 7 m. From a study of 12 step-pool reaches in California, Chin (1999) identified a regular step with an average of 5.29 m by attributing the regularity of step spacing to the influence of slope and channel flow at the time of step formation (Curran and Wilcock,2005).

The study of step-pools is important because they are areas where, in addition to the dissipation of flow energy, outgassing occurs due to the mixing given by the jet stream, which contributes CO_2 emission to the atmosphere. Step-pool hydrodynamics can also influence the development of suitable habitats for salmonids and other fish (Chartrand et al. 2011).

As a result of increasing population numbers, the world's mountainous regions are coming under increasing pressure due to the need for land to be used for timber harvesting, agriculture, hydropower development and urbanization. These places, however, provide most of the sediment transported by rivers, as well as the water supply for adjacent lowland regions. Since mountain basins are likely to include a preponderance of stepped channels, it becomes of particular interest, under conditions of increasing land use, to apply knowledge of the processes acting along stepped channels in order to stabilize channel morphology and control sediment delivery, while at the same time ensuring downstream water for supplies and protection of aquatic habitat (Chin and Wohl, 2005).

2. Area of Interest

Valfredda [Valfrèda in Agordino dialect] is an alpine Village in Falcade (province of Belluno, Veneto Region) located near the San Pellegrino Pass, on the border with Trentino (between the municipality of Soraga and the hamlet of Fuciade).

The Rio Valfredda is found in this locality, a small uncontaminated tributary of the Biois river, with a maximum contributing area of approximately 7.5 km^2. The altitudes vary from 3'000 to 1'600 m.a.s.l..

Moving among the different areas of the basin, both lithology and vegetation are characterized by appreciable spatial heterogeneity; this, of course, greatly affects the observed hydrological dynamics.

The higher parts of the basin are formed by gravel, rocky debris and rocky outcrops; these areas are used for shallow and irregular grazing, that creates karst areas with high soil permeability and thus high rainfall infiltration rates.

Below 2'400 meters above sea level, vegetation consists of some conifers, which grow around the stream, drawing nutrients from the soil, which covers a rocky substrate of sedimentary origin. In the lower part of the basin, below 2'000 meters above sea level, forests cover an impervious pyroclastic substrate.

The climate of the area is alpine, with average annual precipitation of about 1'500 mm/year unevenly distributed in time, with heavy snowfalls in winter and subsequent melting in spring. All this leads to an average annual temperature in the basin of about 4°C (Durighetto et al.,2020).

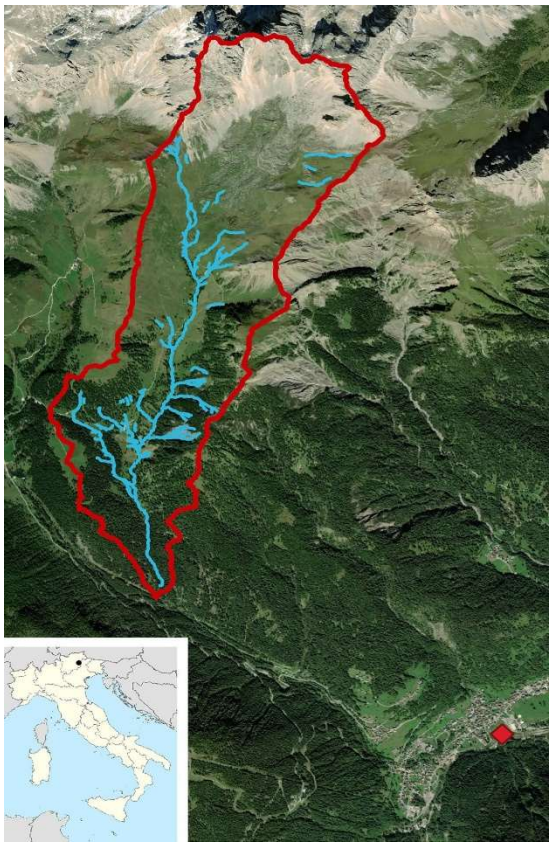

Figure 3: Orthophoto depicting the different land covers of the catchment together with its location in the Italian peninsula (Durighetto et al., 2020)

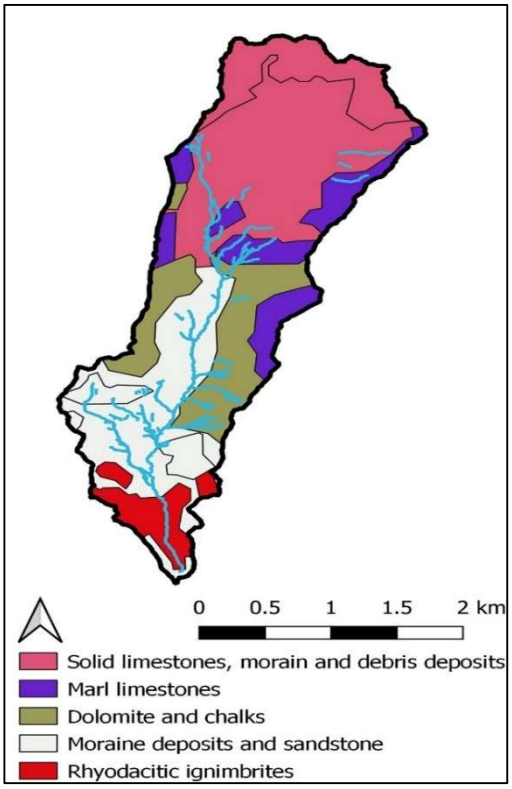

Figure 4: Geologic map of the catchment (Durighetto et al., 2020)

For the purpose of morphological study, the following areas will be examined within this Master's Thesis project:

- Main Stream, located between 1'750 and 1'780 m (visible in red in the Fig.10); downstream of the "Rifugio Flora Alpina". The area is characterized by numerous rocky debris separated from the grazing lands by tall conifers (this area is named "Meteo Valle" because a meteorological station of the "ERC DyNET" project is located there).

Figure 5: Segment of Main Stream at meteorological station site

- Main Stream, located between 1'920 and 1'980 m (visible in light blue in the Fig.10); upstream of the "Rifugio Flora Alpina". The area is characterized by medium to large sized conifers and particularly rocky soil surrounded by green grazing land. The upstream part is enclosed between two very incised mountainsides which limit the view to the sky (this area is named "Principale Ponte").

Figure 6: Segment of Main Stream at "Casoni" site

- "Affluente 1", located between 2'033 and 2'128 m (visible in purple in the Fig.10); The area is characterized by dense and lush herbaceous vegetation and lack of rocks, which are present in small quantities along the stream.

Figure 7: Segment of "Affluente 1"

- "Affluente 3" located between 2'072 and 2'115 m (visible in yellow in the Fig.10); "Affluente 3" has similar vegetation and geology to "Affluente 1", locating itself, however, in a position a little more incised in the terrain.

Figure 8: Segment of "Affluente 3"

- Main Stram, located between 2'119 and 2'028 m (visible in blue in the Fig.10); The area has very heterogeneous characteristics, starting from an incised between grazing lands, then extending below a rocky slope, until it reaches the first conifers downstream (this area is named "Principale Crocefisso").

Figure 9: Segment of Main Stream on Crucifix site

These elevations, as will be explained in the next chapters, are computed with respect to the WGS84 ellipsoid.

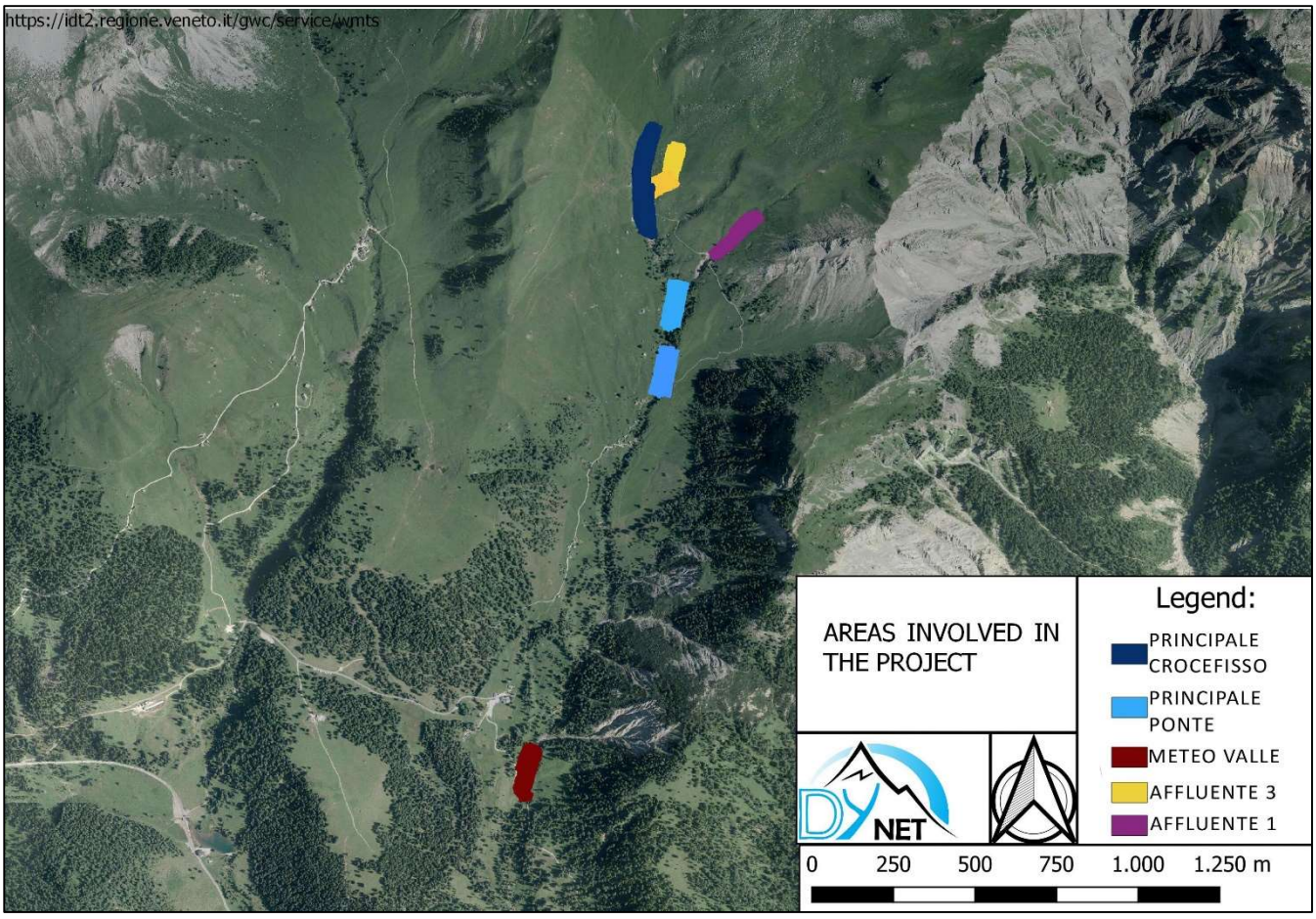

Figure 10: Areas involved in the Project

3. Survey Technologies and Methods

Through this work, morphological data are to be extracted, such as slopes and elevation differences, regarding the Valfredda Alpine Stream and its tributaries, keeping in mind that the morphology of these water bodies is not constant in time, as the mountainous area is in constant evolution. In fact, the sequence of dry periods and heavy rains profoundly marks this landscape, even changing the stream beds markedly over the seasons.

This will be a first attempt, within the project "ERC DyNET", of surveying the Valfredda basin using **R**emote **P**iloted **A**ircraft **S**ystem (SAPR) technology. A preliminary survey of the area was carried out in September 2018, produced a DTM with a maximum resolution of 20 cm, but since then the landscape has undergone deep changes due in part to Storm Vaia, an extreme weather event that affected the north-eastern part of Italy (particularly the mountainous area of the Dolomites and Venetian Prealps) from October 26-30, 2018, thus making this DTM unrepresentative in some areas.

Figure 11:Effects of the storm VAIA (vaiawood.eu)

The survey of some sections of the Main Stream and its affluents started on 13th May 2022 and lasted until 26th August 2022 for a total of 11 field outings, carried out on a weekly cadence under the supervision of Ph. Nicola Durighetto.

The SAPR surveying was complemented by a GPS-type survey based on the **G**lobal **N**avigation **S**atellite **S**ystem (GNSS), which allows for a more accurate, scalable and geolocalizable photogrammetric model.

The combination of these two methodologies allow to acquire data even in areas that are difficult to access, while also providing great versatility and agility of movement despite steep slopes. It also allows accuracies of less than 5 cm to be achieved under optimal flight conditions and satellite configuration.

3.1. Principles of Photogrammetry

Photogrammetry is a surveying technique that enables the determination of metric data, such as the shape and position of an object, through the acquisition and analysis of a pair of frames, taken from different points and representing the same object (stereoscopic pair). The "photogrammetric model" is created from the area in common between two photograms, which provides, through appropriate equipment, the stereoscopic view of the image. This surveying technique is distinguished into aerial photogrammetry, where the camera is located on an airplane/helicopter/drone, and terrestrial photogrammetry with the camera placed on a tripod.

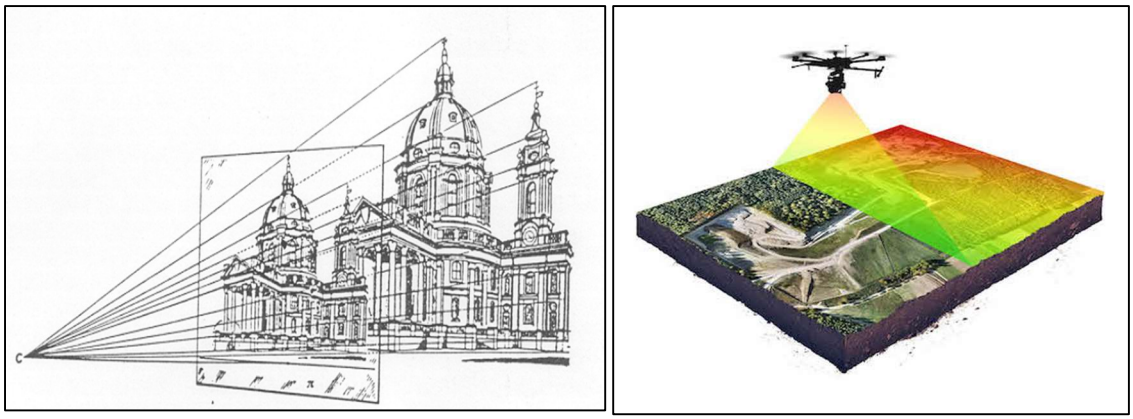

Figure 12: On left side a representation of Terrestrial Photogrammetry (Prof. C. R. Fichera, UNIRC) and on right side a representation of Aerial Photogrammetry (reprojectsrl.com)

Photogrammetry is adopted in cartography, topography, and architecture, and among the advantages in its employment are:

- High accuracy and detail in the representation of the object under analysis;
- Possibility of automating the survey;
- Low cost compared to classical topography surveys;
- Rapid and simultaneous survey of a large number of points, as it is performed a posteriori directly on the images;
- Avoiding direct contact with the object in order to determine its metric characteristics;
- Uniformity of accuracy within the various survey images; meaning that all measured points within the images have the same accuracy, independent of whether they are in the center or on the borders;
- Repeatability of measurements.

The photogrammetric survey is very useful in the analysis of changes and the state of the land as it is possible to derive:

- **Point cloud**: various existing software can determine the coordinates of millions of points on the object creating what is called a "point cloud". As a first output, a sparse point cloud is obtained, which allows assessments of the goodness of the survey, and from it a dense point cloud will be created, which forms the basis for subsequent processing.

Figure 13: On the left an example of sparse cloud, while on the right an example of dense cloud

- **Mesh**: starting from the dense point cloud, each point is connected with a neighbouring one to form a polygonal mesh. This creates a set of faces, edges and vertices that go to define the size and shape of the object. Volumes, areas and distances can be measured on this digital representation.

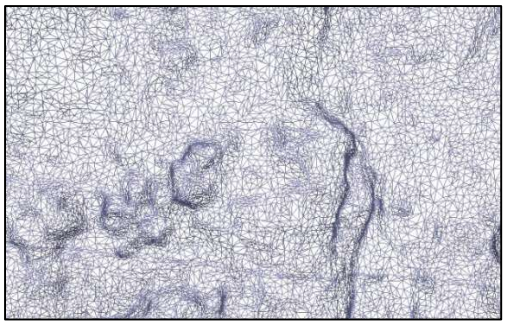

Figure 14: Mesh

- **DEM** (**D**igital **E**levation **M**odel): is a generic statistical surface in which a finite number of points are assigned an elevation coordinate. However, there is no strict and unequivocal definition of the concept of DEM in the literature, normally more specific definitions are used such as DSM (**D**igital **S**urface **M**odel) and DTM (**D**igital **T**errain **M**odel).
- **DTM**: reproduces the trend of the land surface alone ignoring anthropogenic elements and vegetation.
- **DSM**: reproduces the shape of the earth's surface, considering the objects on it (buildings, trees and other artifacts)

Figure 15: On the left side a DSM with anthropic construction and a tree, while on right side a DTM

- **Orthophotos**: the softwares allow the removal of perspective deformations within the photograms so to obtain 2D orthophotos with metric significance. Merging several orthophotos, an Orthomosaic can be generated that represents a larger area on which measurements can be done. In practice this involves moving from numerous central perspectives, as ideally the frames can be considered, to a projection of the terrain and overlying works on the map plane. A central perspective occurs when the object to be portrayed is parallel to the projection plane and the vanishing point, that is, the point toward which the parallel lines appear to converge, is located at the center.

Figure 16: Orthophoto

- **Sections**: from the three-dimensional models seen above, it is possible to extrapolate sections of points of interest.

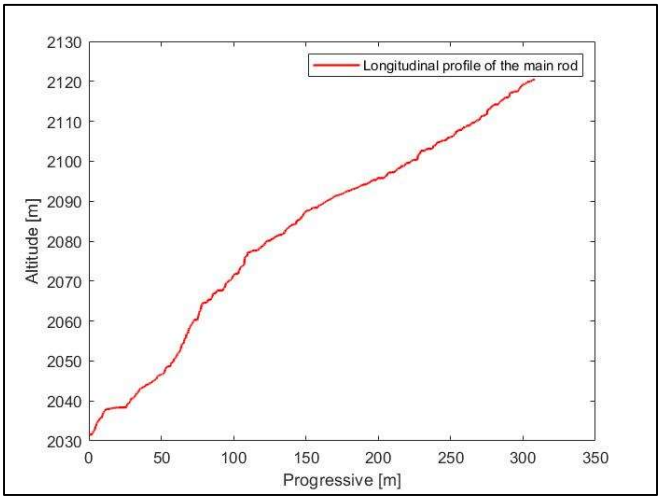

Figure 17: Sections

- **Contour lines:** which are based on the elevation data provided by the DEM.

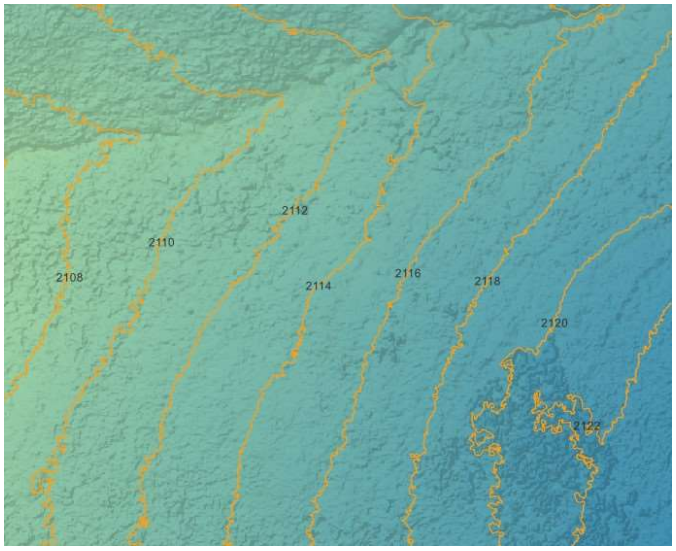

Figure 18: Contours line

Each of these elaborations makes it possible, as discussed in detail later, to extrapolate several information from the survey.

The acquired images are central perspectives of the object, in which the center of grip coincides with the center of the camera's objective. The projection of the grip center in the image plane is called the **P**rincipal **P**oint (PP).

Photogrammetry is based on the principle that each point on the object corresponds to a point in the image plane, which can be determined by means of a bundle of straight lines passing through the camera's grip center and then projected on the image plane.

It is therefore necessary to define the geometric relations that bind the object plane to the image plane. To this end, the image reference system solidal to the image itself is defined, consisting of the axes η and ξ that intersect at the **F**iducial **C**enter (FC), thus representing the center of the image. The Fiducial Center and the Principal Point differ by distances in the maximum order of 20µm (a not negligible value in high-precision surveys) therefore FC will have coordinates η_0 and ξ_0 in the image reference system.

The object reference system is solidal to the survey object, that refers to a generic X, Y, Z local system or cartographic system.

The grip center O of the image, located at the center of the photogrammetric camera lens, will have X_o, Y_o, Z_o coordinates relative to the object system. The distance between the grip center and the image plane is measured along the perpendicular to the image plane and is called the focal distance "c" of the camera.

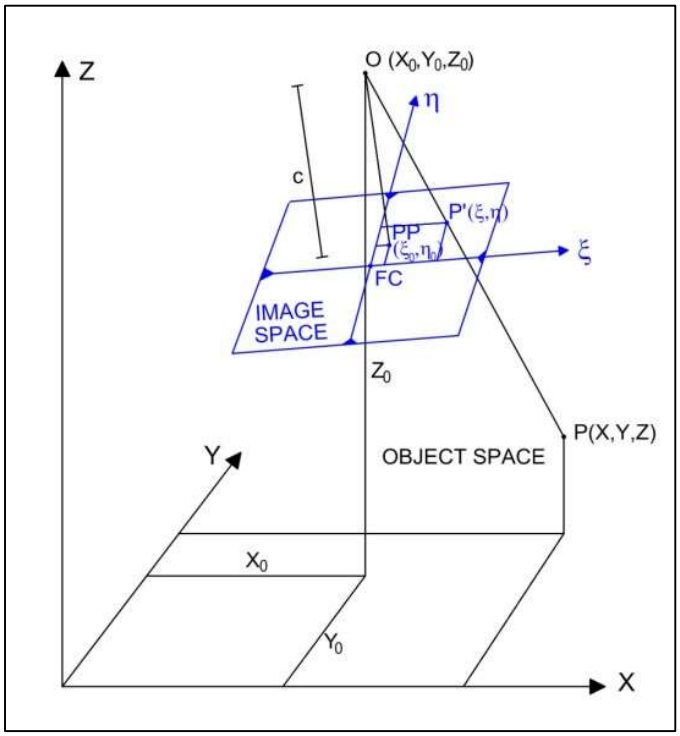

Figure 19: Photogrammetry scheme (Massimo Fabris, "GIS course slides", UNIPD)

In order to provide a stereoscopic view, and thus, to determine the elevations of the object under analysis, 2 images, the coordinates of the 2 centers of grip, the position of the homologous points B' and B" on the images, and the spatial orientation of the camera are necessary. Using this information in the Collinearity Equations, the coordinates of point B in the object system can be determined.

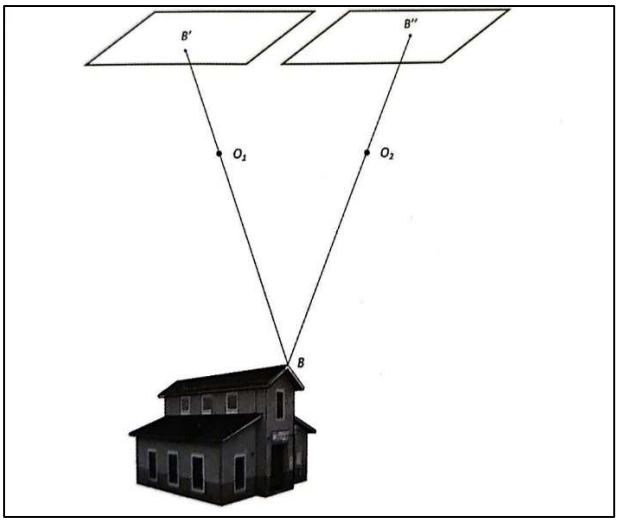

Figure 20: Photogrammetric acquisition (Massimo Micieli, "Aerofotogrammetria con i droni")

It must be specified that the 2 systems (image and object) are not parallel to each other, as, during the drone's capture phases, nor straight flight paths nor a flight attitude of the camera parallel to the ground coordinate

system are guaranteed. Therefore, it is necessary to consider the spatial trim of the frame at the time of acquisitionin order to relate the 2 systems; therefore, the parameters defining the attitude angles of the drone are exploited:

- **Roll**, ”ω”: manifests along the direction of flight; the x-axis is associated with it;
- **Pitch**,”φ”: manifests in the same plane as Roll, but in the direction of the y axis;
- **Yaw**, “k”: manifests along the z axis;

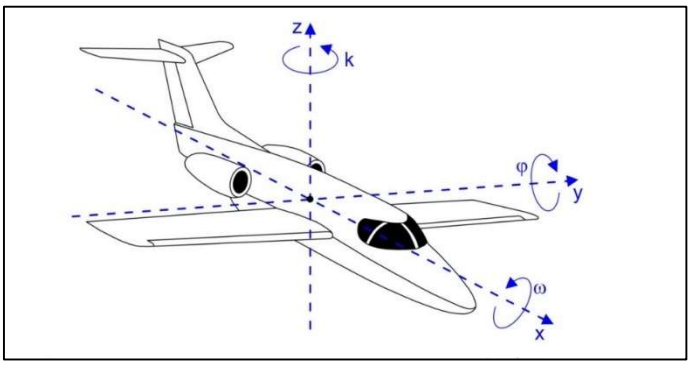

Figure 21: Trim angles of the aircraft (Massimo Fabris, "GIS course slides", UNIPD)

Attention must be paid to the fact that pitch rotation does not properly occur on the y-axis, but on y_ω i.e., the y-axis that underwent ω rotation; while yaw occurs along $z_{\omega\varphi}$, i.e., the z-axis that first underwent roll and then pitch.

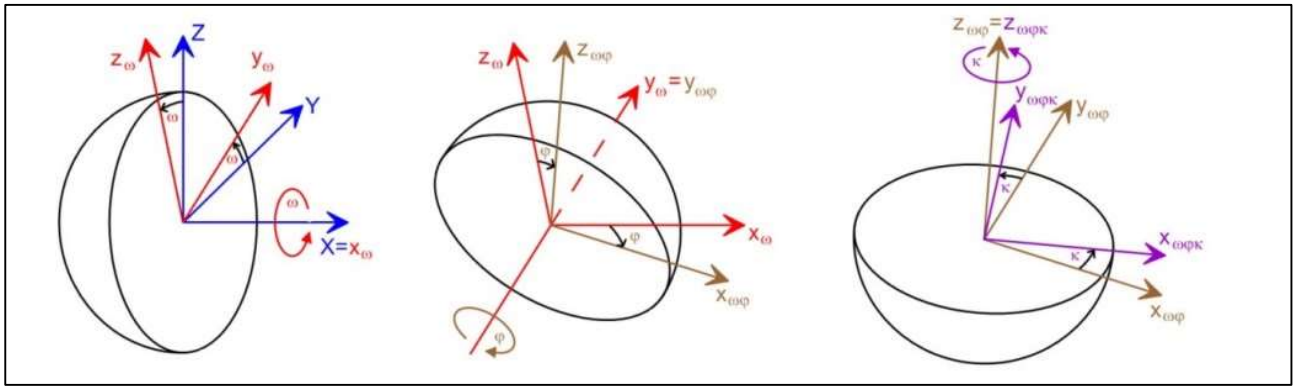

Figure 22: axes of rotation of the aircraft trim angles (Massimo Fabris, "GIS course slides", UNIPD)

The equations that allow to move from a generic point on the image plane to a point in the object plane are called Collinearity Equations:

$$\boldsymbol{X = X_0 + (Z - Z_O)\frac{r_{11}\cdot(\xi-\xi_o)+r_{12}\cdot(\eta-\eta_o)-r_{13}\cdot c}{r_{31}\cdot(\xi-\xi_o)+r_{32}\cdot(\eta-\eta_o)-r_{33}\cdot c}} \quad [1]$$

$$\boldsymbol{Y = Y_0 + (Z - Z_O)\frac{r_{21}\cdot(\xi-\xi_o)+r_{22}\cdot(\eta-\eta_o)-r_{23}\cdot c}{r_{31}\cdot(\xi-\xi_o)+r_{32}\cdot(\eta-\eta_o)-r_{33}\cdot c}} \quad [2]$$

Where r_{ij} are a function of the spatial trim angles (roll, pitch, yaw) of the picture frame.

There are 9 parameters that appear in these 2 equations and are defined as:

- **Internal Orientation Parameters:** provide the internal geometric characteristics of the camera (known in case of metric camera, as they are provided by the manufacturer, while for nonmetric cameras they are estimated by appropriate software).

- **External Orientation Parameters**: provide the geometric characteristics external to the camera, relative therefore to the object reference system, i.e., relative position and rotation of the camera at the time of image acquisition (X_o, Y_o, Z_o and roll, pitch, yaw).
  This orientation step is done through the use of ground anchor points commonly known by the acronym GPC (**G**round **C**ontrol **P**oints). They should be visible on the frames and surveyed by appropriate topographic techniques (GPS survey was used in the present case).

If all the parameters were known, a system of 2 equations and 3 unknowns (X; Y; Z) would be obtained, so with only 1 image it is not possible to solve the problem, but with two images of the same object (taken from 2 different positions) there would be a system of 4 equations and 3 unknowns, thus also giving mathematical explanation to the need for superposition.

These days, photogrammetry is completely digitized, thus obtaining a digital image which consists of a 2-dimensional matrix of numbers whose elements are pixels. Pixels are "g_{ij}" elements of the two-dimensional matrix G representing the digital image, where "i" and "j" refer to the row and column, respectively. In digital photogrammetry, the pixel is considered as the elementary unit; therefore, instead of points in the image, the pixel size defined by "Δx*Δy" is considered.

The image reference system (x,y), conventionally located in the upper left corner, has its origin shifted half a pixel upward and half a pixel to the left (i.e. Δx/2 and Δy/2). In this way it is possible to establish the relationship between the position of the pixel and the coordinate system. In fact, multiplying the indices "i" and "j" by "Δx" and "Δy", respectively, yields the coordinates of the generic point "g_{ij}"; it is also possible to calculate the (i,j) position of the pixel from the (x,y) coordinates.

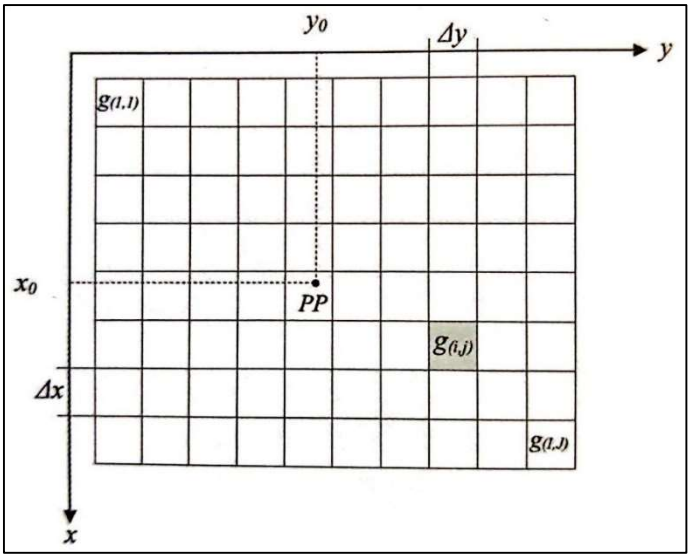

Figure 23: Two-dimensional matrix related to the image coordinate system (Massimo Micieli, "Aerofotogrammetria con i droni")

In order to determine the coordinates of a digital image, automatic pixel identification algorithms are implemented that are based on:

- **Radiometric resolution**: related to the number of bits used to represent the color of the image. Each pixel is then assigned a value between 0 and 255 that represents the color gradient (e.g., 8 bits provides a grayscale image with gradients ranging from 0, representing black, to 255, representing white; in contrast, RGB matrices use 24 bits);
- **Geometric Resolution**: related to the amount of pixels that are contained in one inch (area 2.54 cm x 2.54 cm) i.e., DPI (**D**ots **P**er **I**nch);
- **Spatial Resolution**: i.e., the GSD (**G**round **S**ample **D**istance) representing the area on the ground that each pixel covers. This parameter is a function of the grip distance (flight height "h"), the pixel side size "l" and the focal length "f" of the camera.

The relationship that provides the GSD is given by eq.[3]:

$$GSD = l \cdot h/f \quad [3]$$

The lower is the GSD the more detail will be visible on the ground. In cameras usually the "l/f" ratio is constant, therefore, the parameter to be considered for varying the GSD is the grip height. To increase the resolution, it will be necessary to decrease the flight height, however, doing so will also decrease the size of the photogrammetric cone and therefore more images will be needed to represent the same area.

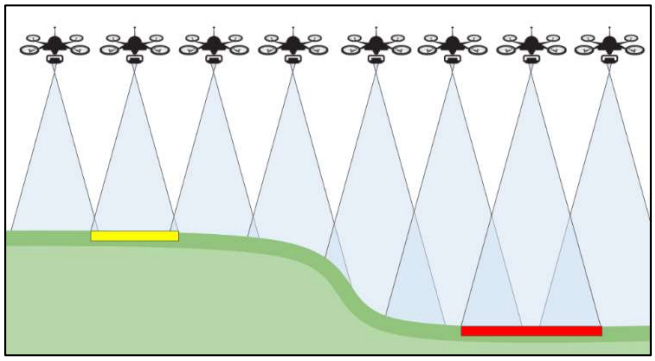

Figure 24: Variation of the photogrammetric cone based on the altitude (Propeller Aero)

In order to build a good photogrammetric model, some very important parameters of digital cameras must be defined, which are essential to ensure good input data; these include:

- **Exposure Time**: this is the time interval (seconds or fraction of seconds) that the shutter remains open so that a predetermined amount of light enters;
- **Aperture**: allows the amount of light passing through the lens to be adjusted;
- **Photographic Exposure**: regulated by exposure time and aperture. Specifically, exposure corresponds to the amount of light that hits the camera sensor in a given time interval, for a given aperture that regulates its intensity;
- **ISO**: adjusts the sensitivity of the sensor thus correlating with the other two parameters above;

The goal is to calibrate these parameters in order to obtain clear photos in motion.

Among the most important steps there is the planning of the photogrammetric flight, carried out in such a way as to satisfy the principle of image superposition, which is required for stereoscopic restitution and thus for three-dimensional modelling.

In the case of nadiral grip (aerophotographic survey of the earth's surface carried out with the optical axis of the camera vertical), rectilinear trajectories at constant speed at a fixed altitude "h" must be carried out, thus obtaining what in topographical jargon is called a "swipe", i.e. the set of frames taken along a single line of flight. The set of several swipes forms the photogrammetric block.

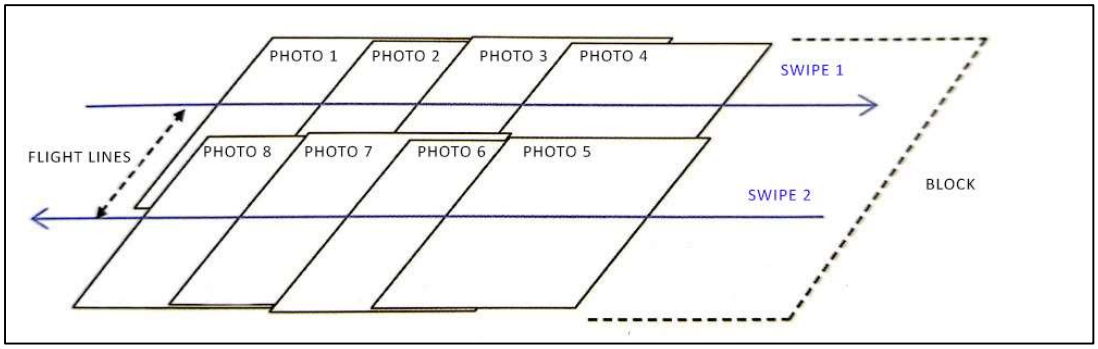

Figure 25: Swipe and Block (Massimo Micieli, "Aerofotogrammetria con i droni")

In order to effectively understand how to ensure that the principle of overlap is respected, it is necessary to define “overlap” and “sidelap”.

The “overlap” (longitudinal overlap) is defined as the fraction of overlapping frames along a swipe, while the “sidelap” (sidelap) is the overlap between 2 swipes; lastly, the distance between 2 grip centers is identified as the “base”.

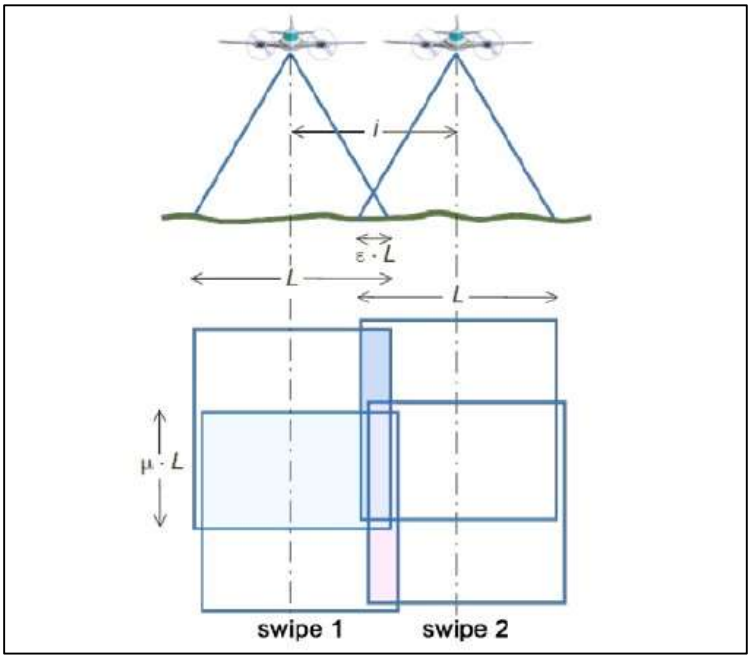

Figure 26: Overlap and sidelap between different frames and swipes (Zanichelli)

In order to have a proper stereoscopic model, the longitudinal overlap must be at least 60 percent for flat terrain and 80 percent for mountainous terrain, also allowing optimal chaining between different frames. The transverse overlap between two adjacent swipes, in flat terrain, must be between 10% and 20% and should be appropriately increased for mountainous terrain.

The flights performed within this project had an overlap of 80% and a sidelap of 70%, in order to cope with the morphological heterogeneity of the Valfredda basin.

Among the first planning steps is the choice of the flight polygon, containing the area to be surveyed, as it will be constructed according to a proper areal coverage for the purpose of 3d restitution.

Polygon construction takes place within software dedicated to drone flight control and planning, which allows tracking of the flight within digital maps made available by the software, requiring as input:

- Flight altitude;
- Percentage overlap and sidelap;
- Flight speed;
- Size and number of pixels of the photo sensor;
- Lens focal length;

Once the above information is inserted, the software will provide the flight plan to the drone, which will execute it in autonomous mode, calculating:

- Ground Grip (frame hugging);
- Total area covered;
- Grip base;
- GSD;

- Total flight distance;
- Flight time;
- Number of pictures;
- Number of swipes;
- Distance between swipes;
- Shooting interval;
- Number of way points (points including latitude, longitude and altitude, used as reference for the purpose of proper flight execution),
- Direction with respect to north of the flight lines.

Unfortunately, SAPR methodology is not exempt from problems, including the following:

- The calculated flight time is very often only indicative, as winds can vary the drone's cruising speed. This problem must be taken seriously considering the limited battery life of the drone;
- The shooting time between images allows to have the desired overlap of images (overlap) as a result; in the case of increasing drone speed the required overlap may not be achieved;
- Atmospheric disturbances may tilt the camera axis moving it from the vertical position. The remedy for this, however, comes with the Gimbal, which allows for angles of ω, φ, k to be almost zero;
- Photos being shot in motion may exhibit the drag effect, which is directly proportional to drone speed, focal length, and shooting time; while it is inversely proportional to flight height. However, this is a theoretical value also conditioned by the quality of the optics used;
- Rolling Shutter, an effect similar to dragging, causes distortion of the frames that could greatly decrease the quality of the model;
- The geomorphological conditions of the terrain and the presence of vegetation and/or objects of various kinds on which the drone might bump into.

Regarding the flight altitude, special attention should be paid in the case of sloping terrain; as, scheduling a flight mission on swipes that are all within a horizontal plane may not be the correct choice to return the model with an evenly distributed degree of accuracy.

In mountainous terrain, where the slope is laudable, one may incur the loss of overlap. In fact, if the distance between the drone and the terrain is reduced, but the camera shooting is left interval unchanged, it results in a reduction of the overlap between consecutive frames, leading to poor performances of the photogrammetric model.

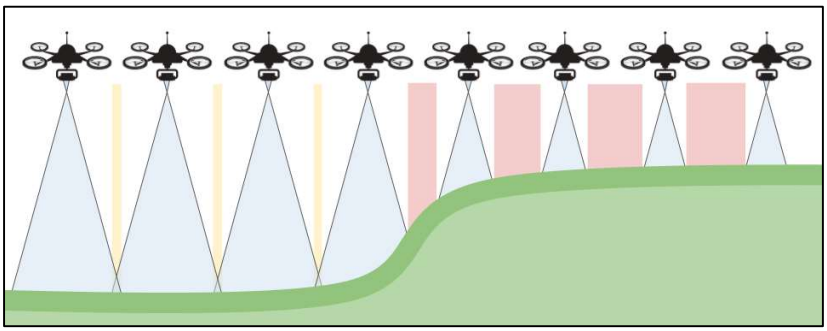

Figure 27: Loss of overlap due to height difference (Propeller Aero)

Vice versa, if the distance between the drone and the terrain increases, the overlap between the frames and the value of GSD (which depends linearly on the height) also increases. However, a high value of GSD results in less detailed images and thus a lower degree of detail in the model.

In order to obtain good photogrammetry even along steep terrain, two different solutions can be adopted:

1. Carry out flight missions at different altitudes in order to keep the GSD unchanged;

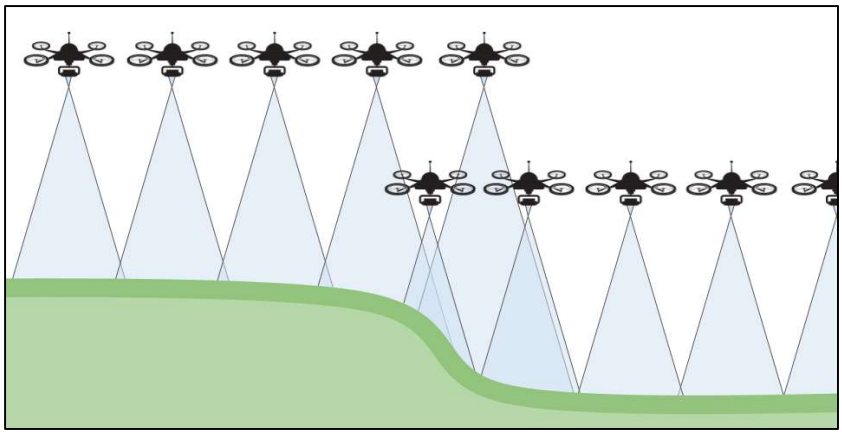

Figure 28: Fly at different altitudes (Propeller Aero)

2. Perform flight missions parallel to the terrain, so that the morphology of the underlying terrain is followed, thus varying the flight height accordingly.

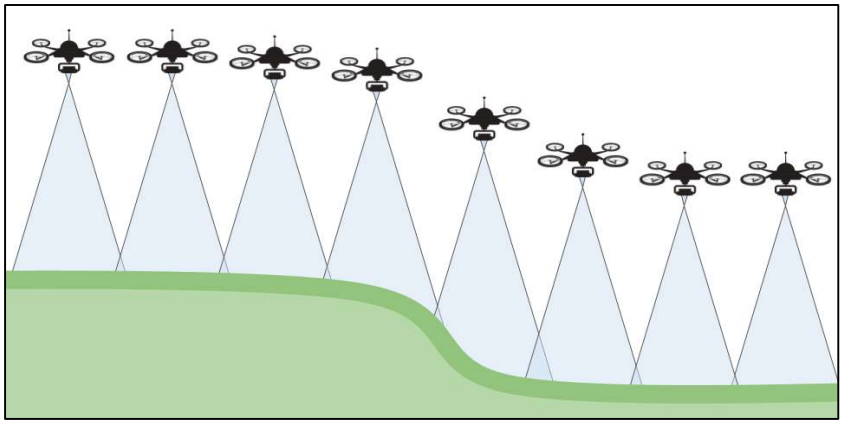

Figure 29: Fly parallel to the ground (Propeller Aero)

In this thesis project, the choice fell on the second solution since the flight software allowed to perform this flight mode.

At the flight is planned according to the procedure sketched above, the distance to be considered for GSD calculation is no longer the flight height, but the normal distance between drone and terrain. So it is important to plan for changes in altitude during the drone's flight mission to adapt to the altitude of the terrain (Paolo Corradeghini, 3d metrica, "Aerofotogrammetria di terreni inclinati").

Therefore, the success of a photogrammetric flight is affected by multiple aspects. When operating drones it is necessary always to evaluate wind conditions carefully and respect the safety requirements of ENAC (**E**nte **N**azionale per l'**A**viazione **C**ivile) regulations.

When talking about APRs, there are differences that make them more or less suitable for carrying out specific operations. The main classification of drones is based on the type of wing they have:

- **Fixed wing**: they are shaped like a miniature airplane and draw propulsion from a small propeller located on the tail of the APR;
- **Hybrid drones:** a hybrid of multirotor and fixed wing;
- **Multirotor:** consisting of arms disposed in a radial pattern on which rotors are installed;

Since the drone used in the survey is a multirotor, with 4 rotors (DJI MATRICE 200 V1 manufactured by DJI), the focus will be on this type of drone, which is also the most widely used given the diversity offered by the market in terms of cost, size and use possibilities.

Figure 30: DJI MATRICE 200 V1 (www.dji-store.it)

The main advantages of this type of drone are:

- The great handling;
- The ability to be stationed on a given point in altitude by being able to vary the camera angle or by making rotations on the same axis;
- High load capacity;
- Possibility of making vertical flights;
- Ability to have minimal space for lift off and landing.

Unfortunately, a low autonomy (10-30min) should be noted as major disadvantages, thus allowing limited areal coverage. In addition, having more engines implies the need for more maintenance.

In this type of drones the frame is generally made of carbon fiber and is designed for the purpose of ensuring perfect balance of the aircraft, providing optimal stability and handling.

The most important part of APRs is the "flight controller", which automatically manages through the IMU (Inertial Measurement Unit) all flight parameters whether they are manual or automatic. The IMU consists of a gyroscope, accelerometer, digital barometer, magnetometer and GPS.

The flight controller makes it possible to:

- Automatically execute programmed flights;
- Control the quality of the radio signal between drone and radio controller;
- Monitor battery status and GPS signal quality;
- Use telemetry, which enables real-time transfer of various info such as: altitude data, GPS position, HDOP (described in the next chapter), cruise and wind speed, flight height, etc. to the ground station (consisting of a tablet or notebook on the ground equipped with specific software for controlling the APR).

In addition to the functions presented above, the flight controller ensures a safe performance of the flight, and to this end the controllers are designed to ensure full respect of the regulations governing the use of SAPRs.

It's reported, for completeness, in Tab.1 the technical specifications of the DJI MATRICE 200 V1.

PARAMETERS	VALUES
Dimensions (unfolded)	883×886×398 mm
Diagonal Wheelbase	643 mm
Number of Batteries	2
Weight	4,69 kg (con due batterie TB55)
Maximum take-off weight	6.14 kg
Payload capacity	1.45 kg
Maximum ascent speed	5 m/s
Maximum descent speed	3 m/s
Maximum velocity	Mode S / Mode A: 81 km/h
	Mode P: 61.2 km/h
Maximum wind resistance	12 m/s
Maximum flight time (with two batteries TB55)	38 min (without load)
	24 min (take-off weight: 6.14 kg)

Table 1: DJI MATRICE 200 V1 parameters

Significantly, in addition to the take-off weight, the maximum flight time is largely influenced by the mode used during the flight: when the flight is pre-programmed, the battery life is longer than in a manual flight condition; this is due to the constant cruising speed guaranteed by the pre-programming.

In the field, it was found that adverse weather conditions, such as high winds, drastically reduced the flight duration to a range of 10 min.

Paired with the drone was the camera, non-metric, Zenmuse X5S also from DJI.

Figure 31: Zenmuse X5S (www.dji-store.it)

It's reported in Tab.2 the technical specifications of the camera.

PARAMETERS	VALUES
Dimensions	140×98×132 mm
Sensor	CMOS, 4/3"
	Effective Pixels: 20.8MP
FOV	72° (with DJI MFT 15mm/1.7 ASPH)
Photo Resolutions	4:3, 5280×3956
	16:9, 5280×2970
Photo Formats	DNG, JPEG, DNG+JPEG
Weight	461 g (Lens Kit)
Exposure Mode	Auto, Manual, Shutter, Aperture
Electronic Shutter Speed	8-1/8000s
ISO Range	100 – 25600 (Stills)

Table 2: ZENMUSE X5S parameters

3.2. GNSS

The **G**lobal **N**avigation **S**atellite **S**ystem (GNSS) makes it possible to determine the geographic coordinates (longitude, latitude and altitude) of any point on the Earth's surface or in the atmosphere as a function of a predetermined reference system.

The reference system used within this thesis is WGS84/UTM zone 32N (**W**orld **G**eodetic **S**ystem 19**84**/**U**niversal **T**ransverse **M**ercator spindle **32 N**orthern Hemisphere), a geographic coordinate system based on the reference ellipsoid developed in 1984, used to approximate the Earth's surface.

The ellipsoid surface is divided into 60 fuses of 6° longitude each numbered starting from Greenwich meridian and proceeding eastward.

Within each fuse, coordinates are determined from the equator and the central meridian of the fuse, which is given a conventional abscissa of 500 km in order to avoid negative abscissa values of points west of the central meridian.

In the UTM system, the ordinate axis is denoted by N (North) while the abscissa axis is denoted by E (East) thus having:

$$\begin{cases} N = X \\ E = Y + 500\ km \end{cases} \quad [4]$$

Italy lies between fuses 32 and 33, where the first is located between 6° and 12° east of Greenwich, and the second between 12° and 18° east of Greenwich.

The ellipsoid was further subdivided into 20 parallel phases of 8° amplitude in latitude from the parallel 80° south to 80° north, and each band corresponds to a capital letter of the conventional alphabet.

The common part between the band and the fuse is defined as the zone with amplitude of 6° in longitude and 8° in latitude and is denoted by the number of the fuse and the letter of the band (the study area is located in zone 32T).

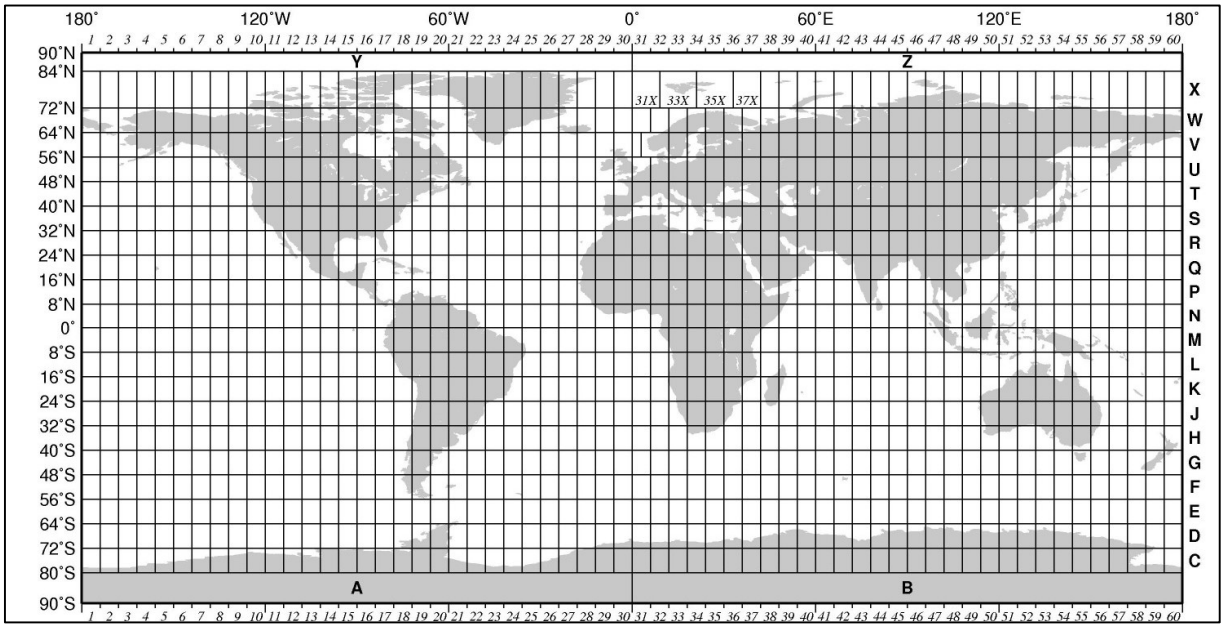

Figure 32: Universal Transverse Mercator projection (www.beamreach.org)

The GNSS consists of several constellations of satellites including:

- **NAVSTAR-GPS** (**Na**vigation **S**atellite **T**iming **a**nd **R**anging **G**lobal **P**ositioning **S**ystem) is a U.S. military satellite navigation and positioning system. It consists of 31 satellites, capable of providing coordinates with 10-20 m accuracy in real time and in all weather conditions, with continuous coverage in every part of the globe.
- **GLONASS** (**Glo**bal'naya **Na**vigatsionnaya **S**putnikovaya **S**ystem) launched in 2001 in Russia, similar to the "NAVSTAR-GPS" boasts 31 satellites, but with real-time accuracy of 2.8 m.
- **GALILEO**: is the European constellation that entered service in 2019 composed of 30 satellites; it can offer an accuracy of less than 10 centimeters in positioning, an accuracy never achieved before.
- **BEIDOU**: was built and managed independently by China and has 30 satellites with accuracy in the range of 5 meters.

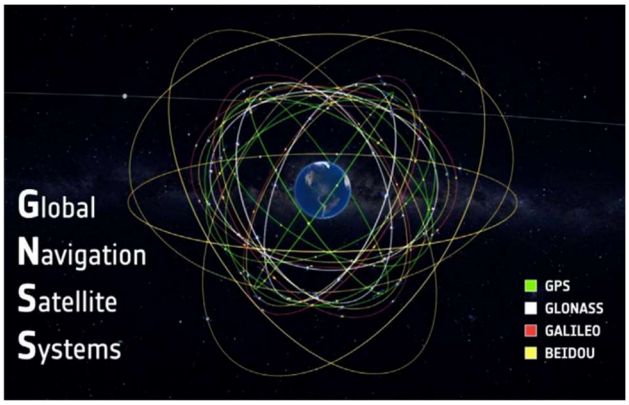

Figure 33: GNSS constellations (3eyegeomapping)

All these systems (together with others of lesser numerical extent, such as the Japanese QZSS system) constitute the GNSS**.**

The structure of GNSS is formed by the:

- **Space segment:** consisting of the satellites orbiting the Earth, which transmit, receive and store information through radio signals and perform orbital correction manoeuvres.
  Through the set of on-board clocks, it is also possible to maintain a time reference, and the fundamental frequency used to transmit satellite data is based on them. From the fundamental frequency are generated the:
  1. **Carrier component:** consisting of 2 sine waves (L1 and L2) generated by multiplying the fundamental frequency by appropriate α and β values (which vary according to the reference system).
  2. **Code component:** consisting of square waves having a value of ±1. The sequence of these values repeats after a certain time interval and is identical to the sequence self-generated by the receiver; the correlation between these 2 signals makes it possible to determine the satellite-receiver distance.
     This category consists of the C/A code (**C**oarse/**A**cquisition) and the P code (**P**recision), the former being modulated only on the L1 frequency, while the latter on both carriers.
  3. **Message component:** contains the satellite identifier, the almanac of the entire constellation, the updated orbit of that satellite, and other information that is loaded into memory as the satellite transits over the control center.

- **Control Segment:** consisting of a series of ground bases that constantly monitor the satellites, process the data that the satellites continuously provide, check and correct ephemerides (coordinates of the orbit that the satellite travels) and on-board clocks.

Each satellite system has a main reference station that collects a week's data, from several secondary receivers, and compensates them by the method of least squares, determining an initial estimate of the trajectory (reference ephemeris) with errors of the order of hundreds of meters. The data collected over the last 24 hours are compared with the corresponding reference ephemerides in order to obtain corrections to the orbital parameters and clocks thus providing from the reference ephemerides the predicted ephemerides (they have an accuracy of about 10 m) which are transmitted from the main base to the satellites, together with the data on the ionospheric model and time corrections. The predicted ephemerides are then sent by the satellites to the users and are called transmitted ephemerides and used to determine the satellite's position. A possible alternative to transmitted ephemerides are post-calculated ephemerides i.e., precise ephemerides, which are obtained by considering data collected over 8-15 days from numerous stations spread over the globe; the collected data are inserted into an orbit calculation program, resulting in an estimated, not extrapolated, orbit with an accuracy of a few meters.

- **User segment**: consisting of users equipped with Antennas capable of picking up signals sent by satellites. The antenna is formed by the:
    1. **receiver:** performs the function of analysing the signals, making calculations and measurements (of correlation and phase shift, for example), and finally stores the information;
    2. **controller**: usually connected via cable to the receiver or via Bluetooth (such as the one used in surveying), it has functions of controlling the operations to be performed and the settings to be imposed.

  Receivers are classified according to the frequencies they are able to pick up, thus dividing into four categories:

    - **Mass market receivers** also called “code measure” receivers (used for terrestrial navigation) acquire only the C/A code;
    - **“Phase/single frequency measurement” receivers** acquire the L1 carrier in addition to the C/A code;
    - **"Geodetic" Receivers** acquire C/A, P, L1, L2 from more than one constellation.

As mentioned above, Receivers correlate self-generated codes, through their clock and microprocessor, with codes from satellites, and once correlated it is necessary to ensure that both code frequencies remain aligned over time.

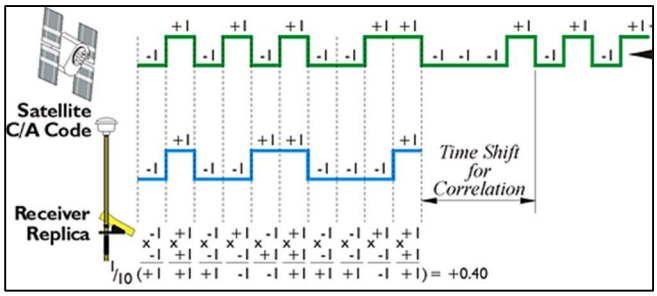

Figure 34: Correlation between the code of the satellite and the GPS antenna (Penn State)

GNSS adopts a spherical positioning method (trilateration), based on measuring the time it takes for a radio signal to travel the satellite-receiver distance.

The time delay between two code sequences (travel time) is related to the time (Δt) it takes for the satellite signal to arrive on earth. Since the incoming signal from the satellite is time-based (because it is not possible for the receiver to know in advance when the signal will be sent), multiplying the travel time by the speed of light in a vacuum ($c \simeq 300000$ km/s) yields the receiver-satellite distance.

However, the computed receiver-satellite distance is perturbed by the asynchronism (μ_{ij}) between space and ground clocks, and that is why the receiver-satellite distance is called the pseudo-distance (D_{ij}).

$$D_{ij} = c \cdot \Delta t \quad [5]$$

(Where "i" stands for the receiver and "j" stands for the satellite)

In order to establish ground position, the receiver must solve a system of 4 unknowns (latitude, longitude, altitude and clock offset) thus needing at least 4 equations and therefore 4 satellites.

$$\begin{cases} D_{ia} = \sqrt{(x_a - x_i)^2\,(y_a - y_i)^2\, + (z_a - z_i)^2} \pm c \cdot \mu_{ia} \\ D_{ib} = \sqrt{(x_b - x_i)^2\,(y_b - y_i)^2\, + (z_b - z_i)^2} \pm c \cdot \mu_{ib} \\ D_{ic} = \sqrt{(x_c - x_i)^2\,(y_c - y_i)^2\, + (z_c - z_i)^2} \pm c \cdot \mu_{ic} \\ D_{id} = \sqrt{(x_d - x_i)^2\,(y_d - y_i)^2\, + (z_d - z_i)^2} \pm c \cdot \mu_{id} \end{cases} \quad [6]$$

The necessity of having at least four satellites for the purpose of determining the coordinates of a point also has graphical demonstration in that:

- given the distance satellite receiver, it is possible to determine the sphere to which the point belongs;
- with two satellites one has that the point belongs to the circumference determined by the intersection of the spheres given by satellite 1-receiver and satellite 2-receiver;
- with three satellites, two points on the circumference are determined;
- with four the point becomes unique (see Fig.35);

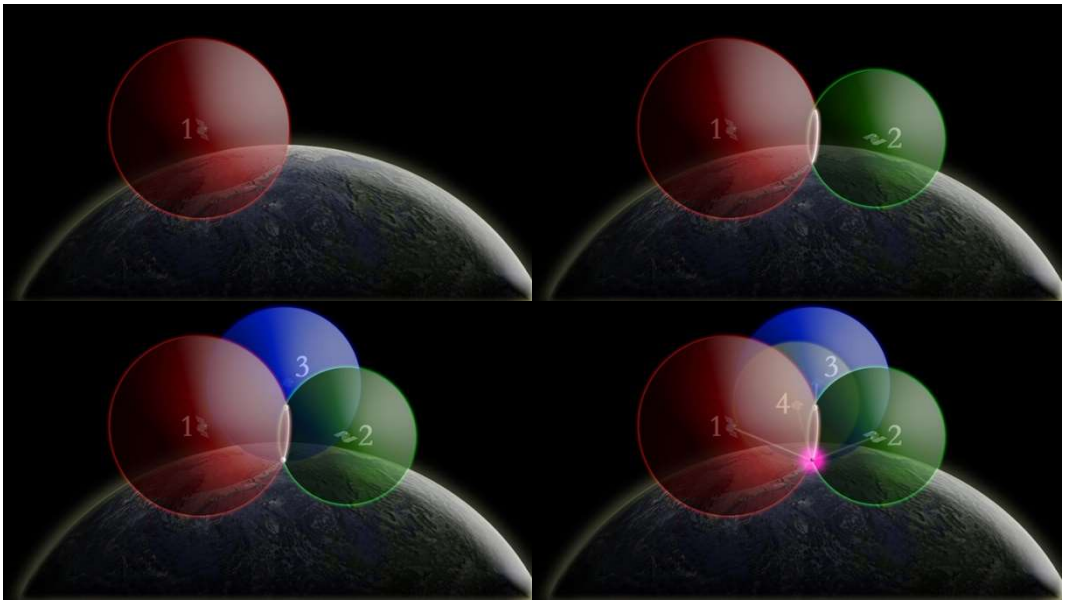

Figure 35: GPS Positioning (oceanservice.noaa.gov)

The receiver also provides another type of measurement, of millimeter precision, namely the "observable phase", given by the phase difference between the signal from the satellite and that generated by the receiver of the same frequency, it varies with time due to the relative motion from the 2 objects.

Techniques for data acquisition using GNSS methodology vary depending on how the receiver is placed on the ground, the number of receivers and for how long it remains in a given location. Among them are:

- **ABSOLUTE POSITIONING:** performed with a single receiver, it allows to obtain the geocentric coordinate of the point in real time using only the code component of the signal, thus having an accuracy on the order of 5-10 meters. It is typically used for navigation.
- **RELATIVE POSITIONING:** allows for the determination of coordinate differences (baselines) between points where receivers are placed at the same instant of time, which acquire both the code component and the phase. Basically, one point of known coordinates (Master) is used in order to determine another (Rover).

Processing is done in post-processing with accuracies ranging from centimeters to a few meters.

- **DIFFERENTIAL POSITIONING:** determines the coordinates of interest, in real time and without requiring post-processing, using a receiver that acquires both satellite signals and a correction from another fixed receiver or a network of permanent stations.
  If the signals acquired and the correction received involve only the code component, the technique is named DGPS (Differential GPS) and achieves accuracies on the order of 0.5 to 1 meter, employed for precision navigation, surveying for GIS, and medium-scale mapping; whereas if the signals received and the correction contain code and phase, the technique is named RTK (Real Time Kinematic) and achieves accuracies of the order of some centimeters. This technique is very fast and productive and is frequently applied in detail surveys, tracing, cadastral operations, and in all cases where rapid positioning with accuracy < 5 cm is required.

  There are 2 modes for RTK surveys:

  1. **RTK Base-Rover:** requires the use of a couple of receivers. It involves the use of one receiver (base) at a point of known coordinates in combination with another (rover) that moves to the various points of interest. The base sends the RTCM (Radio Transmission Format) correction via GSM card (Global System for Mobile Communications, i.e., via SIM) or radio link.

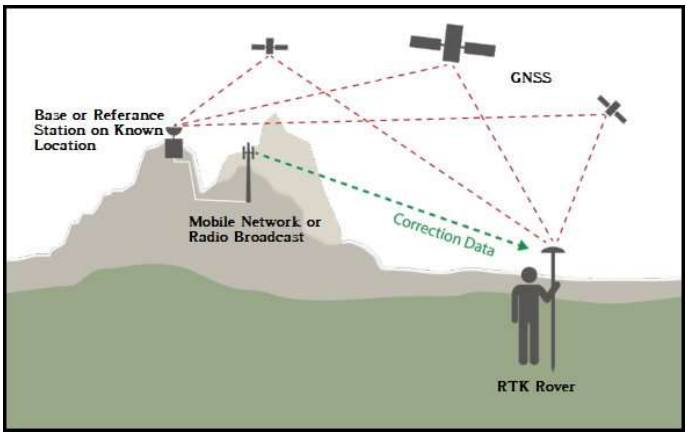

Figure 36: RTK Base-Rover Positioning (datagnss)

  2. **NRTK (Network RTK):** requires the use of a single receiver (rover) that gets the RTCM correction from a network of GNSS permanent stations via modem and GSM card that connects to the network website and acquires the correction in real time.

In accordance with the stationing time, coordinate acquisition techniques are divided into:

METHOD	MEASUREMENT TIME	POSITIONING	PRECISION
STATIC	20-60 min	RELATIVE	1 cm
RAPID STATIC	5-20 min	RELATIVE	3-30 cm
		DIFFERENTIAL	
KINEMATIC STOP AND GO	<60 sec	RELATIVE	3-60 cm
		DIFFERENTIAL	
KINEMATIC	/	ABSOLUTE	10 cm-20 m
		RELATIVE	
		DIFFERENTIAL	

Table 3: Survey methods based on positioning time

During the survey phase, the GPS antenna "Leica GS16" was used to detect the coordinates of GCPs by differential NRTK positioning in stop-and-go kinematic mode.

It's reported in Tab. 4 the technical specifications of the GPS Antenna.

Figure 37: Leica GS16 (Leica Geosystems)

Tracked Signals	Multifrequency
Constellation	GPS / GLONASS / Galileo / BeiDou / QZSS / SBAS
Network RTK	Hz 8 mm + 0.5 ppm / V 15 mm + 0.5 ppm
Static (phase) with long observations	Hz 3 mm + 0.1 ppm / V 3.5 mm + 0.4 ppm
Static and rapid static (phase)	Hz 3 mm + 0.5 ppm / V 5 mm + 0.5 ppm
Reliability	99.99%
Positioning	5 Hz / 20 Hz
Data	Raw data / RINEX data recording / NMEA output
Memory	Micro SD card
Telephone modem	3g
Weight (without battery)	0.93 kg
Battery duration with internal telephone modem	6h
Software and connectivity	Captivate

Table 4: GPS Antenna Parameters

The GPS provides the elevation measurement with respect to the ellipsoid but, as can be seen from Fig. 38, the ellipsoid and geodesic elevation lines are not coincident, but display a very small vertical deviation angle. Luckily the approximation to 2 coincident lines is conceded and the elevation difference between geoid and ellipsoid is provided through the geodesic undulation.

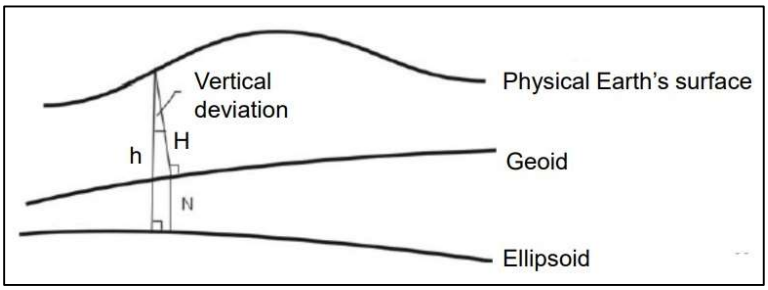

Figure 38: Difference between geodetic and ellipsoidic elevation (Massimo Fabris, "GIS course slides", UNIPD)

In Italy, the "Italgeo model" is used for geodetic ripple estimation, which provides accuracy of 4 cm.

In this Thesis work, conversion from ellipsoidal to geodetic elevations was not performed, not being of particular interest; therefore, elevations will be a function of the WGS84 reference surface.

Although the use of GPS methodology can provide very accurate results for the purpose of positioning it is not free from random and systematic errors that can compromise the results. Among them are:

1. **Satellite and receiver clock error:** composed of asynchronism (temporal shift of the origin of time between satellite and receiver clocks) and drift in time (the temporal variation of an indication, due to changes in the metrological properties of a measuring instrument) of one or more clocks due to their malfunction.
2. **Orbit error:** consisting of the uncertainty of the orbit of satellites, caused by various physical phenomena (e.g., Earth's gravitational field, attraction of celestial bodies, solar pressure, etc.). DOP (**D**iluition **O**f **P**recision) indices give an indication of the contribution of this uncertainty. Among the various indices is GDOP, which was visible directly from the controller in the field and defines the relationship between receiver position errors, time errors, and receiver-satellite distance errors through the function:

$$GDOP^2=PDOP^2+TDOP^2 \quad [7]$$

Where TDOP (**T**ime **D**ilution **O**f **P**recision) measures the magnitude of the DOP positioning error caused by the offset of clocks; while PDOP (**P**ositioning **D**ilution **O**f **P**recision) expresses the relationship between the receiver position error and the satellite position error according to the function:

$$PDOP^2=HDOP^2+VDOP^2 \quad [8]$$

Where HDOP (**H**orizontal **D**ilution **O**f **P**recision) measures the magnitude of DOP errors in latitude and longitude and VDOP (**V**ertical **D**ilution **O**f **P**recision) in altitude.
In the field, it was possible to operate with GDOP less than 5, a good value considering that the range of this indicator is from 1 to 20, where proximity to 1 is an indication of optimal satellite distribution.

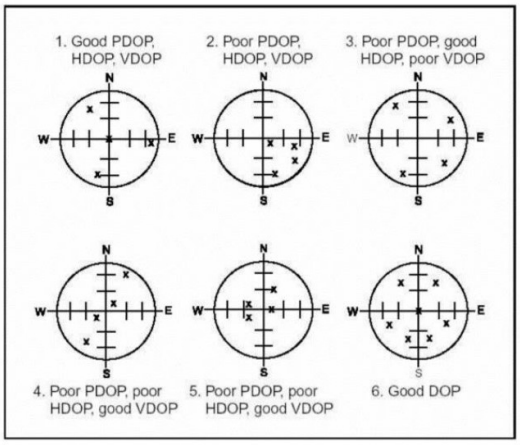

Figure 39: Trend of the DOP indices based on the satellite configuration (CIRGEO UNIPD)

3. **Ionospheric Refraction:** in the ionosphere the GPS signal is scattered differentially affecting codes (delaying them) and carriers (advancing the phase). Observations could be carried out at night to reduce this phenomenon, as ionospheric activity is minimal at this stage of the daily cycle, or correction ionospheric patterns can be applied. Dual-frequency receivers make it possible to estimate the delay, taking advantage of the different influence of the ionosphere on the frequencies of the two L1 and L2 carriers (this capability also turns out to be in the GPS used in the field).

4. **Tropospheric refraction:** it delays the propagation of the GPS signal. The delay does not depend on frequency, but on atmospheric parameters and the satellite's elevation above the horizon. Tropospheric delay has been found to increase significantly with elevations less than 15° from a plane passing through the instrument center and parallel to the horizon. Tropospheric models or a cut-off angle that excludes satellites at elevations less than 10/15° can also be used for correction here.

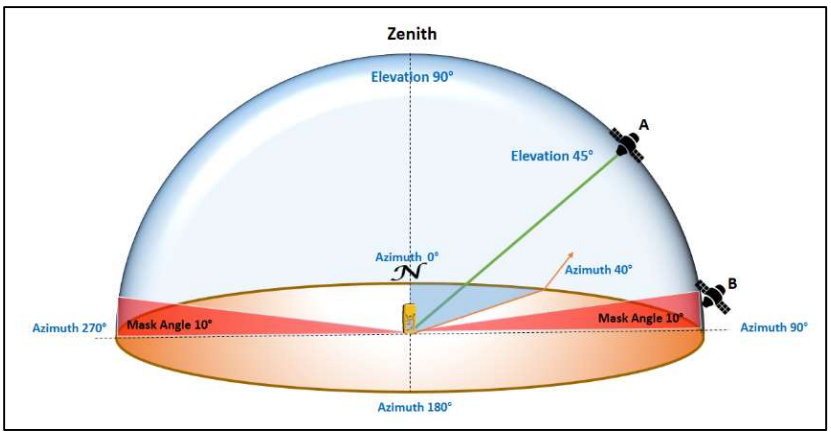

Figure 40: Cut-off Angle (Chinmaya S Rathore, CoG,IIFM)

5. **Multiphath:** occurs when the received GPS signal is composed of two parts: one direct and one reflected. The reflected part arrives at the receiver later, with respect to the direct part, creating an ambiguity about the time of arrival of the signal and thus distorting the measurement of the distance

to the satellite. To limit this error, the position of the antenna must be carefully chosen so that it is free from obstructions to the sky, which can cause reflected signals.

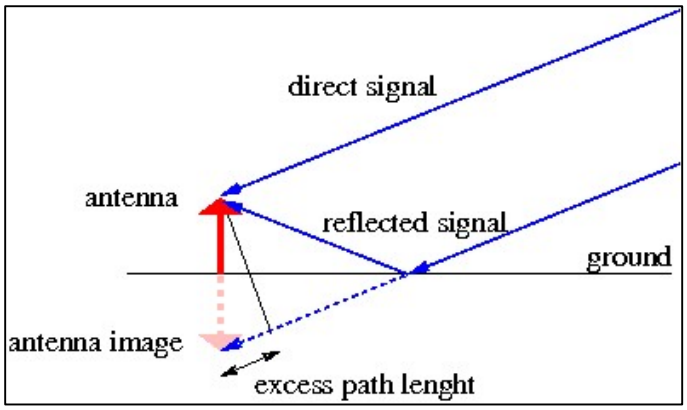

Figure 41: Multiphat (gssc.esa.int)

6. **Electromagnetic interference:** The presence of any other electromagnetic signals may interfere with the GPS signal by increasing noise.
7. **User error:** Human error is the one that numerically makes the largest contribution to the overall error present in GPS measurements; it is due to inaccuracies such as failure to measure antenna height, incorrect transcription of measurements, etc.

3.3. Softwares

3.3.1. Agisoft Metashape

In order to be able to process the photogrammetric model, which will allow the morphological study of the basin, Agisoft Metashape was adopted.

Agisoft Metashape is a stand-alone software that makes it possible to photogrammetrically process digital images from RGB or multispectral cameras (including multicamera systems) and generates 3D spatial data based on the **S**tructure **F**rom **M**otion (SFM) algorithm. This algorithm is a range imaging technique of computer vision and visual perception, in which the process of estimating three-dimensional structures is done from sequences of two-dimensional images coupled with local motion signals. Simply put, from photographs taken in motion, it is possible to reconstruct a point cloud with 3D coordinates.

The use of this Software allows, depending on the hardware specifications of the computer in which it is employed, fast data processing and thanks to its intuitive and linear workflow can be easily mastered even by a non-specialist, allowing complete control over the accuracy of the results thanks to the automatically generated report at the end of the computation.

Agisoft Metashape's output products include:

- 3D Models;
- DEMs;
- Orthophotos;

which can be used in GIS applications, documentation of cultural patrimony and production of visual effects, as well as for indirect measurements of objects of various scales.

The software offers absolute accuracies of up to 2-5 cm (depending on the GSD), which can vary depending on the method of image acquisition, the accuracy of the drone's GPS data and from the GCPs, but most importantly on the degree of accuracy required by the survey.

3.3.2. QGIS

QGIS (**Q**uantum **G**eographic **I**nformation **S**ystem) software was used to support Agisoft Metashape and to extract additional information from the photogrammetric models.

QGIS is the world's most widely used Open-Source Geographic Information System that enables the visualization, organization, analysis and representation of spatial data; it allows data from different sources to be merged into a single spatial analysis project.

GIS technology integrates into itself:

- the computerized drawing system or CAD;
- the relational database DBMS (**D**ata **B**ase **M**anagement **S**ystem);

Thus, enabling both the analysis and search operations typical of Databases, with the geographical analysis and representation typical of CAD.

The data are divided into Layers and from them a map is created with the graphics customizable by the user, who can enrich it with icons and labels dependent on the attributes of the cartographic elements.

3.3.3. UGCS

UGCS (**U**niversal **G**round **C**ontrol **S**oftware) allows planning photogrammetric surveys with the help of advanced Tools.

Among the strengths of this software are:

- the function-rich graphical interface that allows control and planning of flights;
- the ability to program flight paths that the drone will execute automatically using Waypoints (points above which the drone is bound to pass);
- the resuming of missions from the point of interruption (e.g., after battery change);
- the return of the elevation profile to the screen;
- the direct control of the drone;
- the control of the remote control;
- the simulation program that allows to test a route before flying it with a real drone;

Fundamental to obtaining an excellent survey is the planning phase consisting of:

- Verification of the legislative and physical constraints present in the area of interest;
- Definition of the final quality of the required outputs (GSD, spatial accuracy, etc.);
- Flight planning with the appropriate tools provided by UGCS. Very important are the overlap and sidelap parameters, the GSD, flight speed and take-off and landing points.

In addition to flight parameters, it is also possible to set camera parameters such as ISO, zoom, focus, etc.

After each flight plan is calculated, it is uploaded to the drone thus allowing the automatic flight mode which makes available on screen the elevation profile and altitude, both above ground and sea level, of each location where the drone will visit.

In addition to automatic mode, the software also allows to use the drone in manual mode, a very useful option in emergency situations such as wind gusts or various unpredicted events that may occur on the field.

3.3.4. Matlab

In order to extract further information from the previous computations, it has been used Matlab (**Ma**trix **Lab**oratory), a programming software that integrates:

- computational functions;
- graphical visualization;
- programming.

It is implemented in a GUI work environment having a modular structure, which provides a functionality with considerable expandability.

It is possible to speak of both “Matlab language” and “Matlab work environment” since they have considerable integration.

Matlab's main interface consists of several windows that you can place side by side, move, minimize, resize, and so on. The main used windows are four:

- Command window;
- Workspace;
- Current directory;
- Command history;

It is also its remarkable customization that makes Matlab one of the most widely used programming and computing platforms in science and engineering.

4. Data Acquisition

The survey phase was carried out on a weekly basis from 13th May 2022 until 26th August 2022.

The methodology explained in the previous chapter was used for data acquisition; therefore, during the various weeks of the measurement campaign, images were acquired by SAPR and the coordinates of the Markers were acquired by GPS in stop-and-go kinematic mode, with stationing on GCPs of about 30 seconds and NRTK differential positioning based on the permanent GPS stations of the Veneto Region.

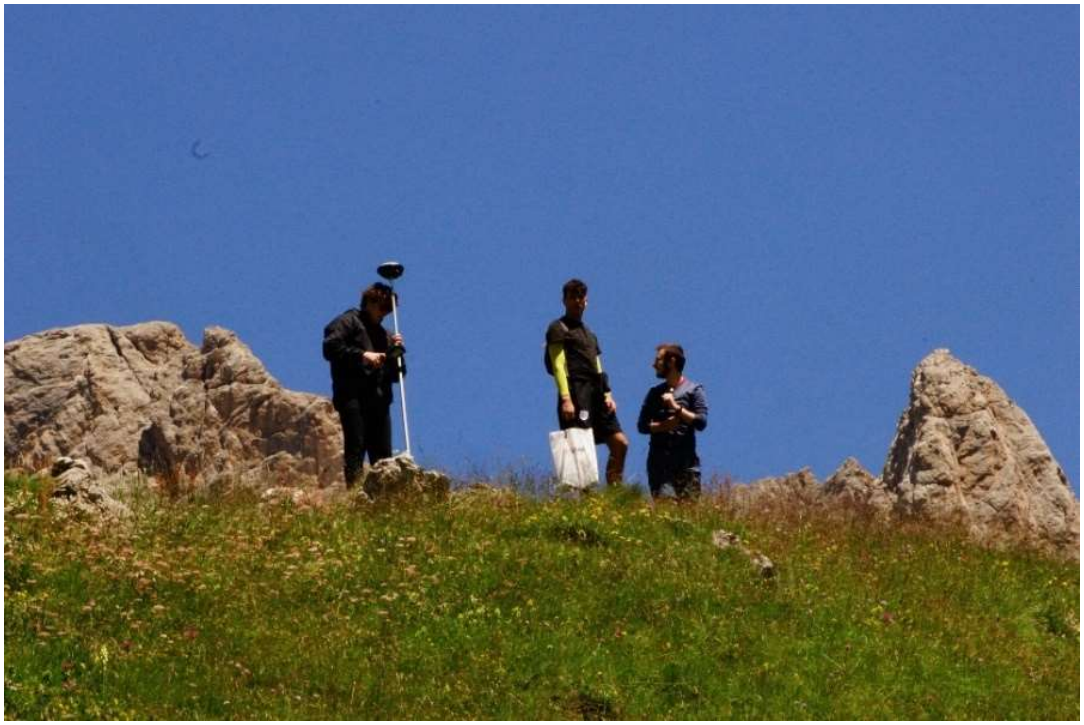

Figure 42: Point Acquisition with methodology kinematic stop and go

The number of GCPs was chosen according to the morphological complexity of the area subjected to survey; that is, in the presence of numerous slopes and complex geometries the number of GCPs was appropriately increased in order to make the output model more robust and reliable.

Out of all the points on the ground surveyed in the measurement phase, a part as already mentioned has been used as GCPs, while a second part will fill the role of QCPs (**Q**uality **C**ontrol **P**oints, identified by the software as Check points) i.e., points of the survey whose topographic position is known, useful for comparing their position with the position of the corresponding point of the model, already scaled, oriented and rototranslated with the GCPs, thus giving a measure of the goodness of the survey.

Depending on the area of survey, there are:

- ***Meteo Valle***: 9 GCP and 4 QCP:

Figure 43: GCP and QCP of "Meteo Valle"

- ***Affluente 1***: 20 GCP and 5 QCP:

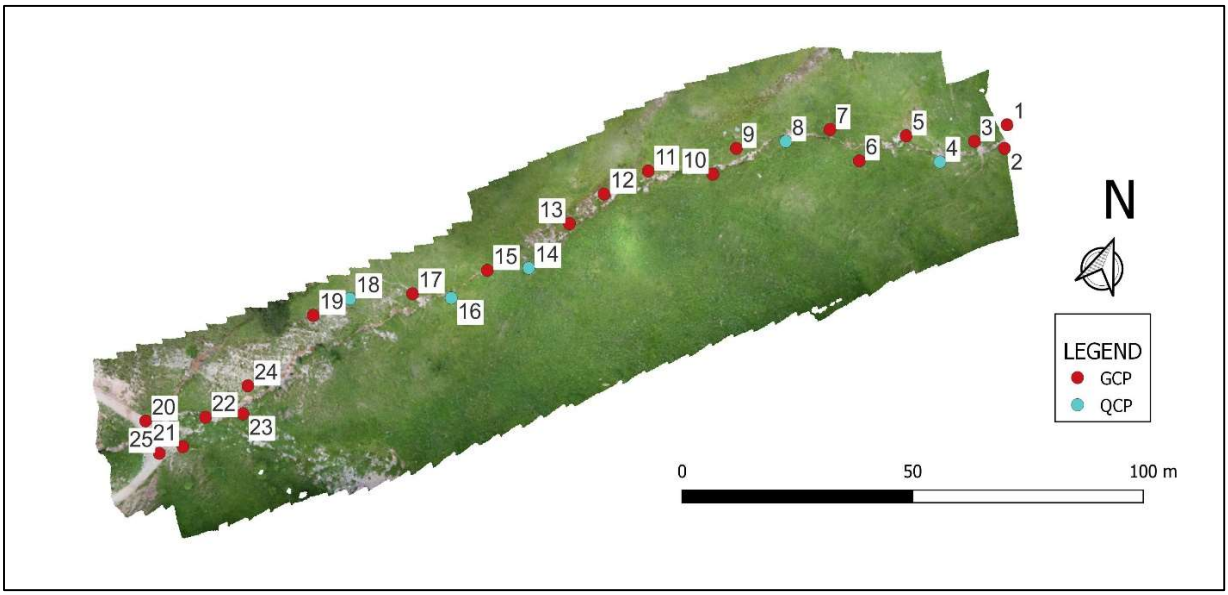

Figure 44: GCP and QCP of "Affluente 1"

- ***Principale Ponte downstream***: 15 GCP and 5 QCP

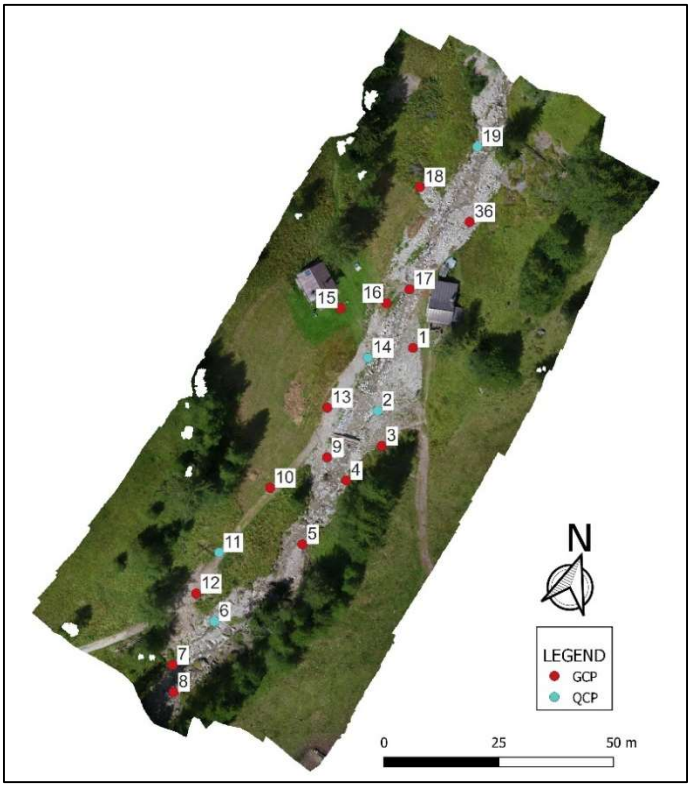

Figure 45: GCP and QCP of "Principale Ponte Downstream"

- ***Principale ponte upstream***: 9 GCP and 5 QCP

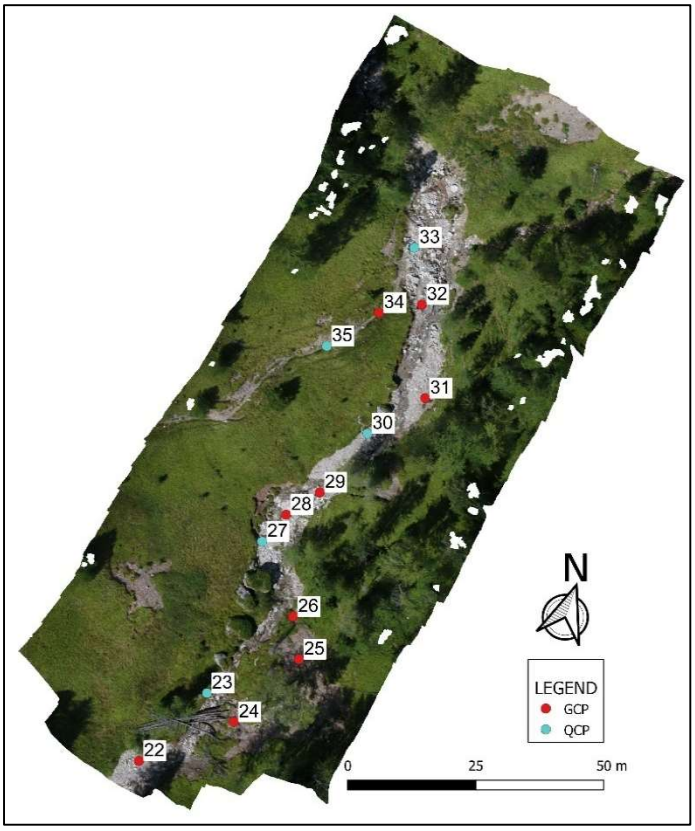

Figure 46: GCP and QCP of "Principale Ponte Upstream"

- ***Affluente 3 upstream***: 8 GCP e 4 QCP:

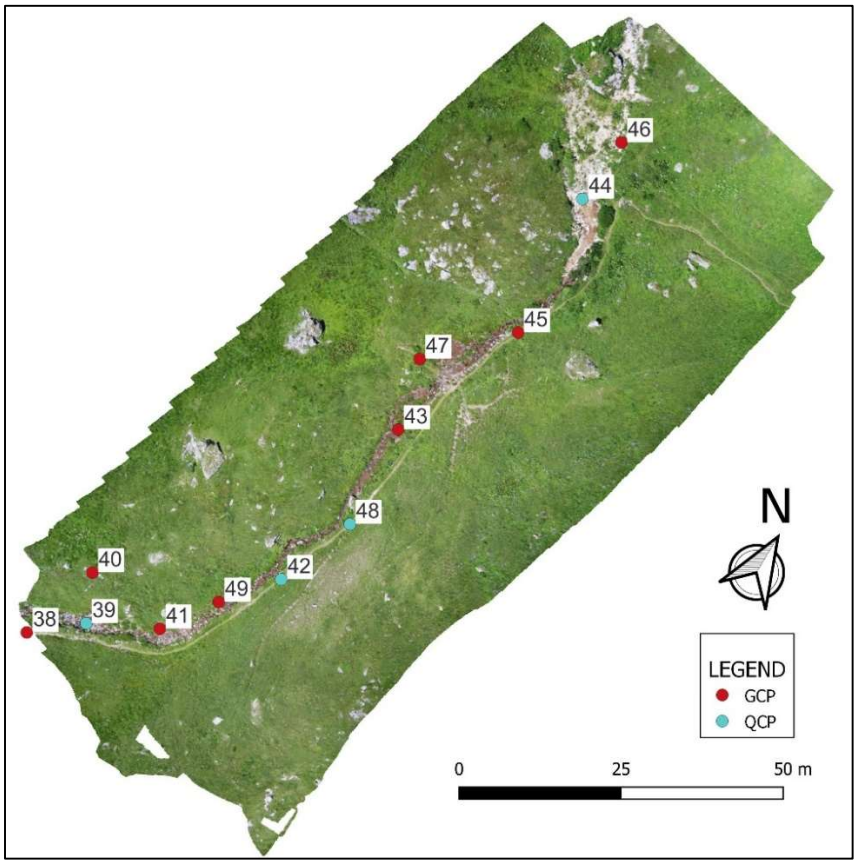

Figure 47: GCP and QCP of "Affluente 3 upstream"

- ***Affluente 3 downstream***: 7 GCP e 4 QCP:

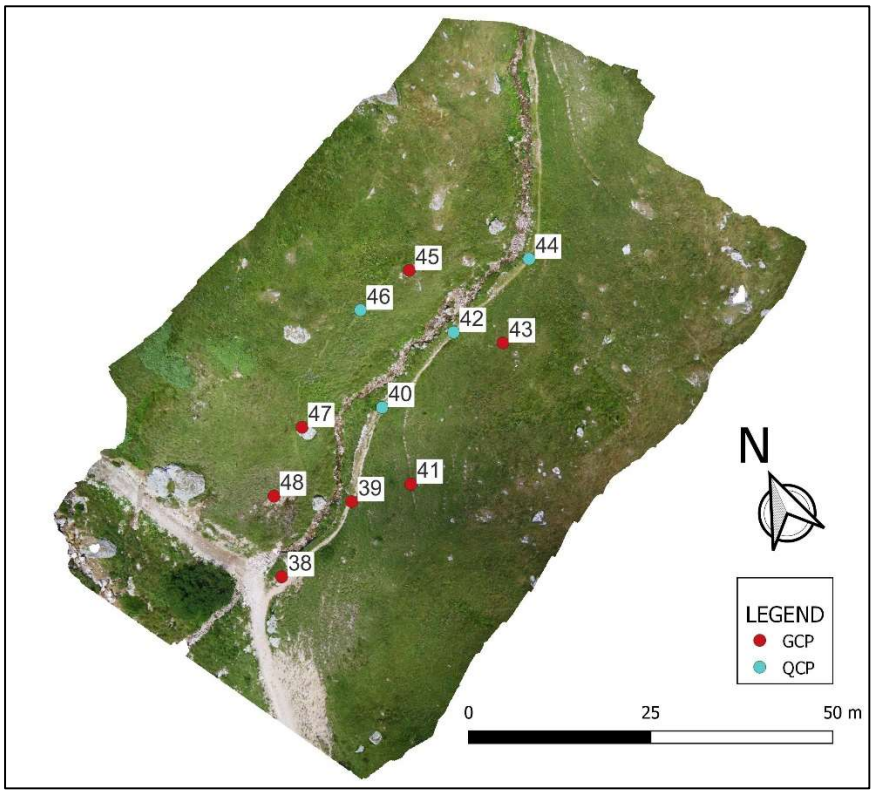

Figure 48: GCP and QCP of "Affluente 3 downstream"

- ***Principale Crocefisso upstream***:14 GCP e 6 QCP:

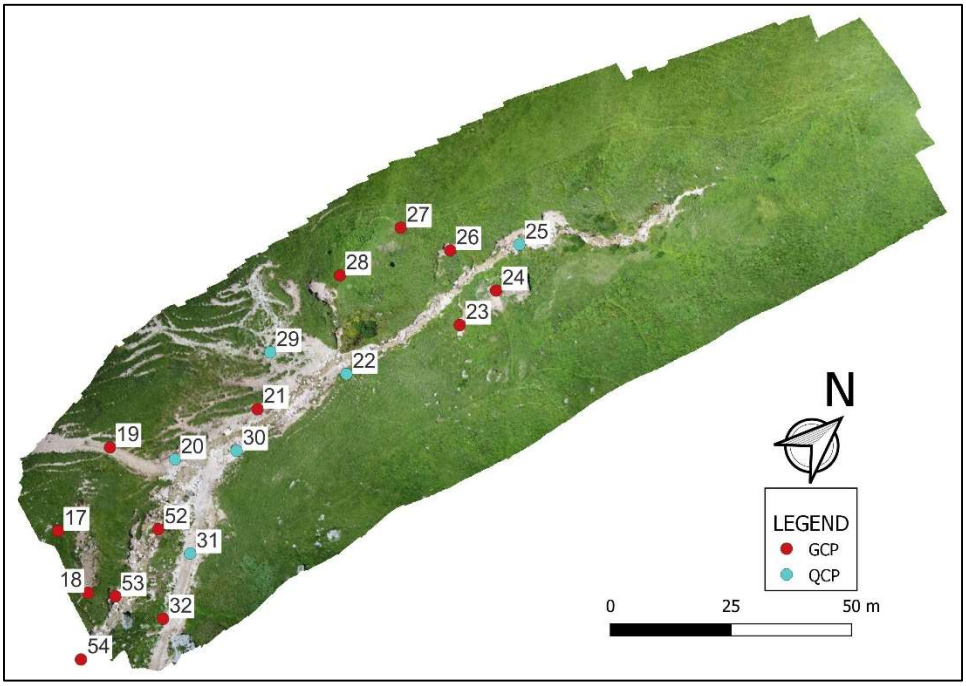

Figure 49: GCP and QCP of "Principale Crocefisso upstream"

- ***Principale Crocefisso downstream***: 27 GCP e 11 QCP:

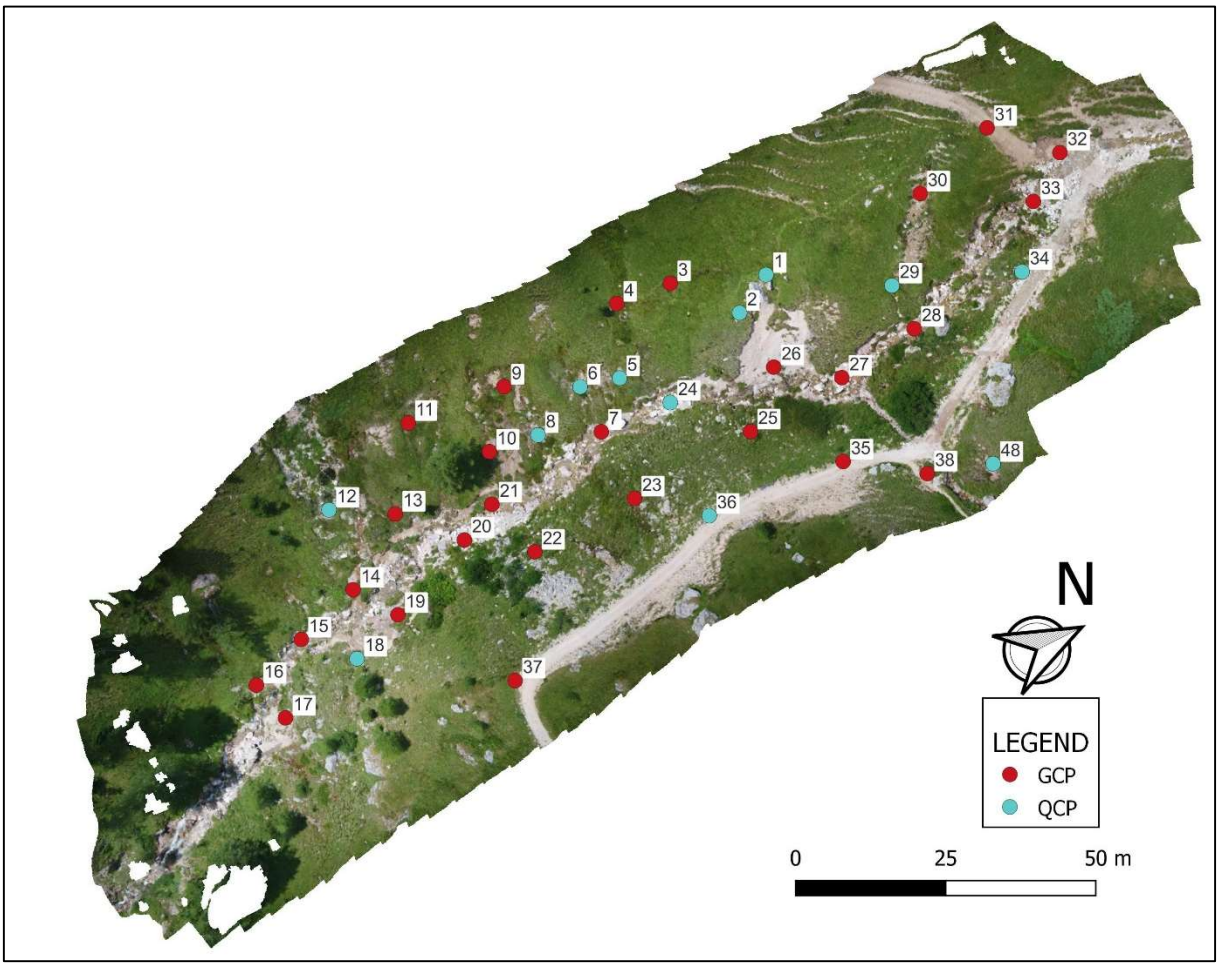

Figure 50: GCP and QCP of "Principale Crocefisso downstream"

Self-generated Agisoft Metashape targets were used, printed on recycled paper to reduce overexposure caused by sun reflection and in A3 format to ensure visibility.

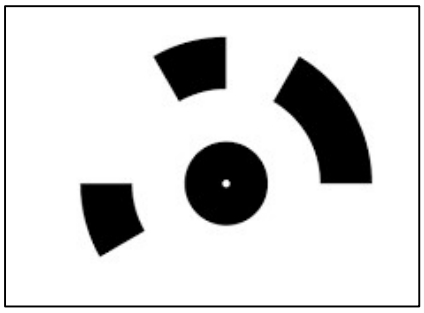

Figure 51: Default Metashape marker

Good practice to be followed in the arrangement of GCP-QCPs includes the following rules:

1. Uniform disposal over the entire survey area (this was not possible in the survey of "Affluente 1" due to very tall and strong grass and "Meteo Valle" for problems which will be discussed in the following chapters);
2. Placement in elevation changes;
3. Guaranteed visibility in photographs;
4. Ground fixation so as to ensure the same position between SARP and GPS survey.

The 5 areas of interest differ greatly in morphological characteristics and climatic conditions during the survey, so in addition to a different number of GCP/QCPs, the flight and photographic parameters, entered into UGCS, also require adjustments.

In particular:

- AFFLUENTE 1:

Flight speed [m/s]	2.50
GSD [cm]	0.75
Overlap [%]	82
Sidelap [%]	73
Direction angle [°]	50
ISO	200
Distanza focale [mm]	14

Figure 52: Mission "Affluente 1" on UGCS

- PRINCIPALE PONTE:

Flight speed [m/s]	1.8
GSD [cm]	0.75
Overlap [%]	82
Sidelap [%]	73
Direction angle [°]	13.31
ISO	200
Focal length [mm]	20

Figure 53: Mission "Principale Ponte" on UGCS

- AFFLUENTE 3 AND PRINCIPALE CROCEFISSO UPSTREAM:

Flight speed [m/s]	2.50
GSD [cm]	0.75
Overlap [%]	82
Sidelap [%]	73
Direction angle [°]	15
ISO	200
Focal length [mm]	15

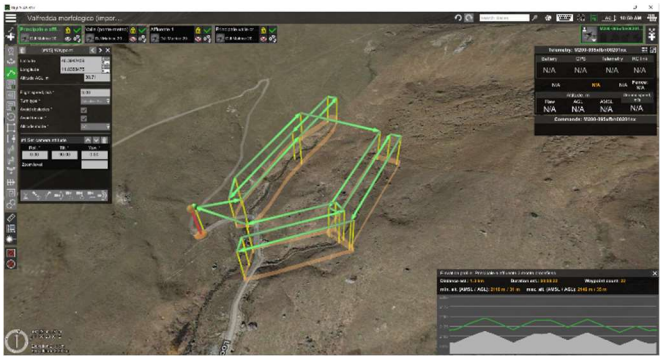

Figure 54:Missions "Affluente 3" and "Principale di Monte" on UGCS

The downstream part due to poor accuracy was remeasured below.

- PRINCIPALE CROCEFISSO DOWNSTREAM AND AFFLUENTE 3 DOWNSTREAM:

Flight speed [m/s]	1.80
GSD [cm]	0.75
Overlap [%]	82
Sidelap [%]	73
Direction angle [°]	65
ISO	200
Focal length [mm]	15

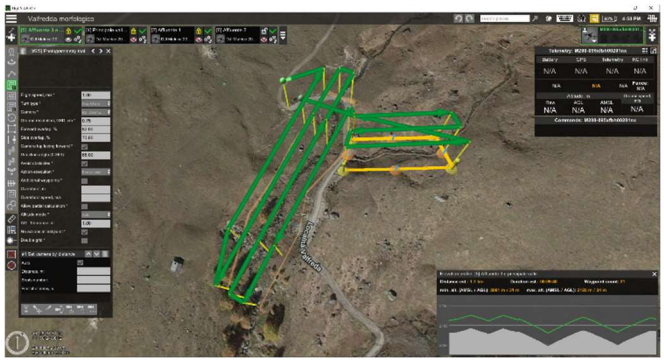

Figure 55: Missions "Affluente 3 di valle" and "Principale di valle" on UGCS

- METEO VALLE:

Flight speed [m/s]	2.00
GSD [cm]	0.75
Overlap [%]	85
Sidelap [%]	75
Direction angle [°]	200
ISO	200
Focal length [mm]	25

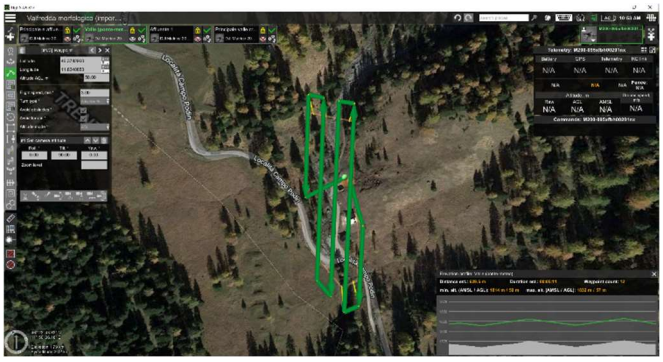

Figure 56: Mission "Meteo Valle" on UGCS

5. Data Processing

Once the field phase of image and coordinate acquisition is completed, the creation of the photogrammetric model in Agisoft Metashape is carried out.

Processing is facilitated by the software's simple and intuitive workflow, which consists of 7 steps:

1. Uploading photos;
2. Photo alignment;
3. Construction of the dense point cloud;
4. Construction of the mesh;
5. Creation of the textures;
6. Creation of the DEM;
7. Creation of the Orthomosaic;

Once the photos are loaded inside the workspace it is possible to perform a preliminary phase of quality control of the photos; in fact, through the "Images Quality" command it is possible to have an estimation of the goodness of the acquisition by means of the range of this indicator that goes from 0 to 1, to be interpreted as closer get to unity the better the image (the range commonly used is between 0. 75 and 0. 9, photos with lower quality are discarded). The images used in this work all have a rating above 0.8.

Photos

Label	Size	Aligned	Quality	Date & time	Make	Model	Focal length	F-stop	ISO	Shutter	35mm focal
DJI_0588	5280x3956	✓	0.865713	2022:07:01 15:39...	DJI	FC6520	25	F/7.1	200	1/1000	50
DJI_0589	5280x3956	✓	0.870668	2022:07:01 15:39...	DJI	FC6520	25	F/7.1	200	1/1000	50
DJI_0590	5280x3956	✓	0.870517	2022:07:01 15:39...	DJI	FC6520	25	F/7.1	200	1/1000	50
DJI_0591	5280x3956	✓	0.863083	2022:07:01 15:39...	DJI	FC6520	25	F/7.1	200	1/1000	50
DJI_0592	5280x3956	✓	0.860349	2022:07:01 15:40...	DJI	FC6520	25	F/7.1	200	1/1000	50
DJI_0593	5280x3956	✓	0.864719	2022:07:01 15:40...	DJI	FC6520	25	F/7.1	200	1/1000	50
DJI_0594	5280x3956	✓	0.855982	2022:07:01 15:40...	DJI	FC6520	25	F/7.1	200	1/1000	50
DJI_0595	5280x3956	✓	0.845831	2022:07:01 15:40...	DJI	FC6520	25	F/6.3	200	1/1000	50
DJI_0596	5280x3956	✓	0.845198	2022:07:01 15:40...	DJI	FC6520	25	F/7.1	200	1/1000	50
DJI_0597	5280x3956	✓	0.844709	2022:07:01 15:40...	DJI	FC6520	25	F/6.3	200	1/1000	50
DJI_0598	5280x3956	✓	0.845687	2022:07:01 15:40...	DJI	FC6520	25	F/6.3	200	1/1000	50

Figure 57: An example of Photo parameters used in Agisoft Metashape

Metashape also gives, at this preliminary stage, the possibility of using masks to remove unwanted objects that would otherwise show up in the final model (for example, moving people).

Once the preliminary editing phase is over, a first alignment of the photos is done. It will be possible to choose the degree of accuracy of the alignment and modify some advanced parameters such as the maximum number of points analysed per image (key point limit) and the number of points used to tie the images (tie point limit). By checking adaptive camera model fitting, the software will perform additional automatic corrections to the alignment.

Once the alignment phase is finished, the software will automatically create the sparse point cloud consisting of the tie points used in the alignment phase.

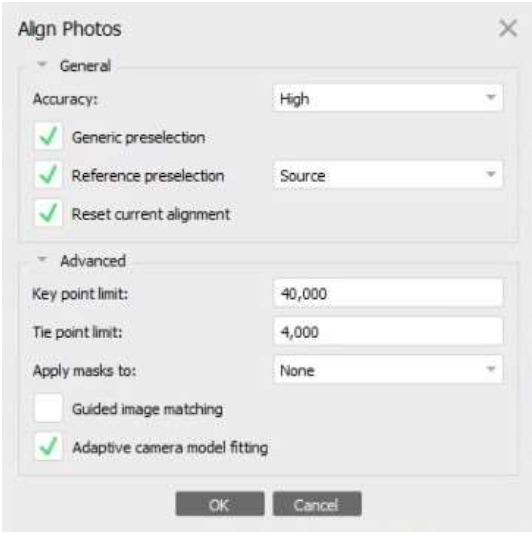

Figure 58: Align Photos Window with project settings

In order to have a scalable, georeferenced and properly oriented product, the optimization of the alignment, accessible through the "Reference" panel, is carried out. During this phase it will be necessary to make explicit the reference system of the project, drone and GPS detected points and then proceed with the loading of GCPs and QCPs.

Agisoft Metashape provides an automatic marker recognition system, to which the GPS coordinates are then associated using a ".csv file"; unfortunately, this option never provided optimal accuracies during the various photogrammetries, so manual input was adopted. Important graphical support was provided by QGIS; in fact, thanks to its Data Base Management System function, it made the Markers inside the photos easily distinguishable, thus allowing their correct identification and assignment of coordinates (as visible from Fig. 43 to 50).

Having inserted all the GCPs and QCPs within the various images and making their coordinates explicit, the alignment optimization is carried out, which will return the sparse cloud of points in the chosen reference system (WGS 84 UTM 32N).

From the workflow menu it will now be possible to construct the dense point cloud. This step is one of the most computationally onerous and the higher the quality selected, the longer it will take to return the output.

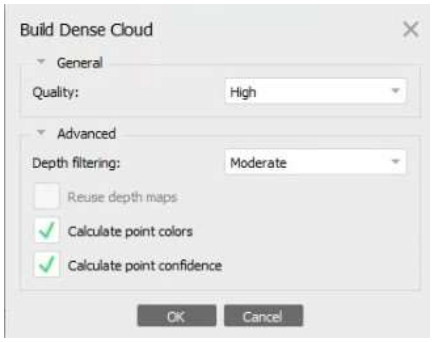

Figure 59: Build Dense Cloud Window with project settings

The Ultra high option is the only one that processes the images in the original format, all other choices involve scaling down the quality.

In the "Advance" section of dense cloud construction, a filtering operation can be performed that removes outliers that might occur. High quality and moderate depth filtering were used in all five models, this choice was a good compromise between computation time and result since the ultra-high option with aggressive filtering did not result in appreciable improvements.

Regarding the modelling of "Affluente 3" and some sections of the Main, given the considerable amount of photos, it was necessary to subdivide the model, through the possibility of Metashape to work in chunks (groups of photos). In this way, it was possible to work with groups of photos that underwent Workflow separately until the dense cloud stage, and then proceed to the alignment of the chunks and finally to the union. Merging of the chunks is done by dense cloud points or tie points or by the coordinates of GCPs.

In parallel with the dense cloud, "depth maps" are generated as visualizations of the depth parameter processed through stereoscopy by the software.

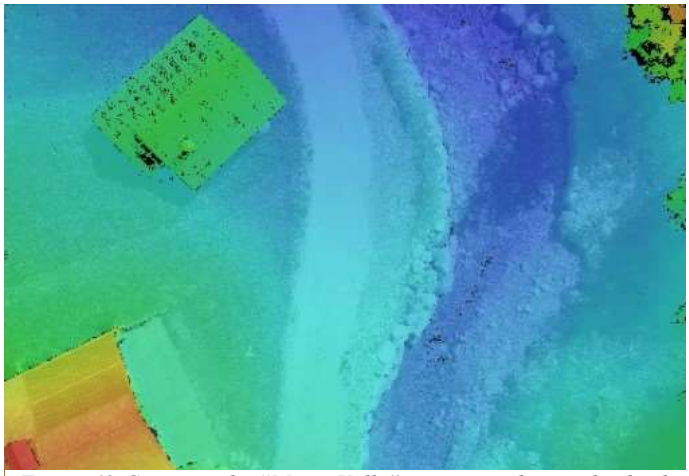

Figure 60:Casoni in the "Meteo Valle" area according to the depth parameter (it goes from red "higher altitude areas" to blue "lower altitude areas")

Therefore, it will be possible to visualize the images no longer only in RGB mode, but also according to this parameter.

Once the dense cloud construction procedure is concluded, construction of the mesh is carried out. The main difference between dense cloud and mesh is that the last one is a surface composed of adjacent triangles, while the dense cloud is a set of distinct points. The algorithm, based on the points of the dense cloud, creates the triangles of the mesh. Through the "Face Count" option it is possible to decide on the quality of the triangulation, which in this case is always set to high, i.e., the closest possible points will be used for the creation of the polygons. The software will also interpolate the holes within the mesh to avoid discontinuities.

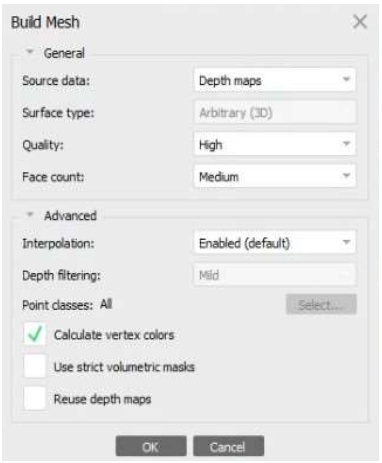

Figure 61: Build Mesh Window with project settings

In this work, the mesh was created from depth maps instead of the dense cloud because the mesh creation algorithm based on depth maps is much more performant. It is appreciable, moreover, the difference in the 2 methods in the regions with presence of cavities or jagged areas in which the choice of the dense cloud leads to an increase in noise, while through depth maps a filtering procedure intervenes that makes future processing on the mesh easier (such as exclusion of points from the wrong position).

At the end of mesh processing, a model consisting of triangles (Model Wireframe) and a color model (Model Shaded) will be created, which at first a glance might be a very good representation of reality, but zooming in reveals a scarcity of detail.

Figure 62: Model Shaded quality example

To have a model visibly more defined and representative of reality, the creation of the texture of the model is carried out.

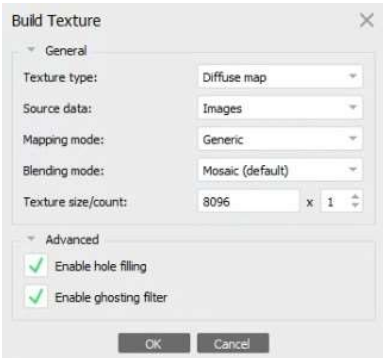

Figure 63: Build Texture Window with project settings

The texture is a kind of dress that is sewn from the images that have been loaded into Metashape and allows to see the details of the model. This dress is dropped onto the mesh which gives the texture, shape and geometry.

The texture is strictly dependent on the mesh, changing quality or other settings of the mesh results in a need to recompute the texture, also without mesh the texture creation cannot take place.

The process of mesh creation and texturing provides a 3D model, which can be useful for detailed visualization of the area of interest, since it is possible to move through it via the Metashape GUI, but appreciable numerical data of the survey area will be provided by the DEM and orthophotos, instead.

The creation of the DEM results in a 2.5D image where in addition to the dimensions of length and width, which are visible graphically in the image, a numerical value of height is attached to each pixel. Metashape

does not distinguish between DSM, DTM and DEM, the distinction can be made in post processing by classifying the point cloud. Since the area of interest in this thesis is the stream area, thus purely considering this portion within the various models, the DEM provided by Metashape can be considered as a DTM minus the water height, which is small anyway due to drought.

The DEM is based on the dense cloud and is provided according to the desired reference system (WGS84 fused 32N). The most important parameter regarding this product is the resolution, i.e. the portion of the terrain represented by the single pixel, a parameter that will change between the models due to different flight settings.

The last step available within the Metashape workflow is the construction of the Orthomosaic from orthophotos.

Figure 64: Build DEM Window with project settings of "Meteo Valle"

Orthophotos are photographs that have the property of being orthographic projections, i.e., all vertical elements of the image disappear; it is as if each is viewed from its very top.

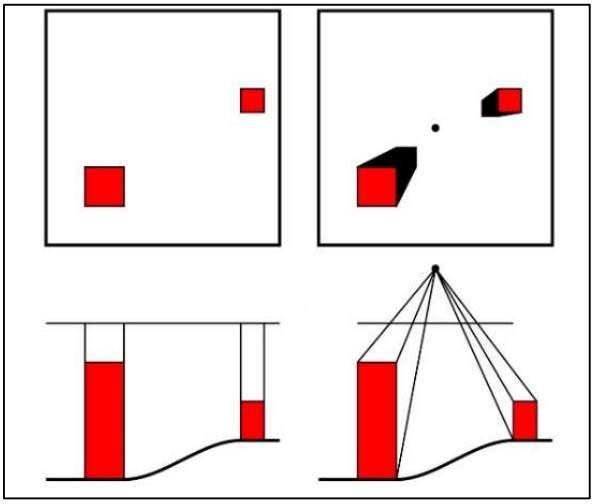

Figure 65: On the left the orthographic view while on the right the perspective view (3dmetrica)

Figure 66: Collages of orthophotos that form an Orthomosaic

The Orthomosaic is a purely 2D product; it is an image, at high resolution, that is reconstructed by taking all the images in the dataset that make up the photogrammetric project; they will be corrected in distortion, merged together and projected onto the DEM or mesh generating a georeferenced and scaled output where each point is seen from its vertical (a valid statement in the case of nadiral orthophotos such as those performed in this project). Therefore surfaces that scale in the nadiral direction will be represented only from the top (this is perfectly visible at "Meteo Valle", at "Affluente 3", at "Principale Crocefisso Upstream" and at "Principale Ponte" due to the presence of buildings).

The DEM was chosen as the support surface for orthophotos because it is a solid support with optimal resolution for generating an Orthomosaic. In case of fast processing, moreover, the choice of DEM saves time as it requires less computation time compared to mesh.

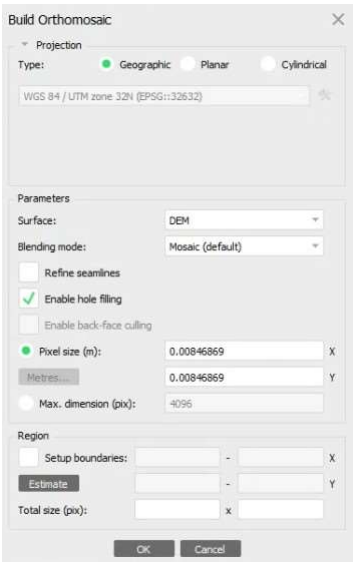

Figure 67: Build Orthomosaic Window with project settings of Meteo Valle

Prominent among the parameters shown in Fig.67 is "pixel size" [m] or GSD, a parameter that changes from model to model as a function of the grip distance, optics and sensor size. The selected value was the maximum obtained from the dataset; therefore, it does not make sense to decrease this value in order to have a better GSD as the data do not allow it. Instead, the increase of the pixel size is permissible as it can reduce the weight of the model. The GSD was kept the same as that set in the field during the processing of the various considered models.

Since the Orthomosaic is a georeferenced and scaled product, once exported to Metashape or CAD/GIS programs it allows for planimetric measurements.

The DEM files, in order to a better visualization, will be exported through "file.tiff" and then processed within QGIS, so to increase the accessibility exploiting the combination of color grading and hill shading function, which are available in the software raster settings, thus giving a more three-dimensional view to the DEM. In addition, thanks to computerized drawing system present in QGIS, it was possible to perform scaling and rotation procedure while maintaining both metric and georeferencing properties of the project, both for DEMs and Orthomosaics.

On the basis of the three-dimensional data stored in the DEM maps were created with the additional and integrative information of contour lines with a pitch of 2 m, which give an immediate representation of the morphology of the territory.

In addition to what has been done so far, information extraction will continue within the GIS environment, taking advantage of the processing tools:

1. ***r.watershed***: takes the elevation information input from the DEM and through the Multiple Flow Direction (MFD) algorithm provides the "Drainage Direction", the "Stream segments", and the "Number of Cells that Drain through each Direction" in the form of a raster file. The MFD algorithm implemented by QGIS exploits the slope between cells forming a given area to distribute a hypothetical water flow, this process occurs in proportion to the degree of slope present between cells.

   The output "Number of Cells that Drain through each Direction" reports for each cell the average value of the areas that contribute to the runoff along the hydrographic network.

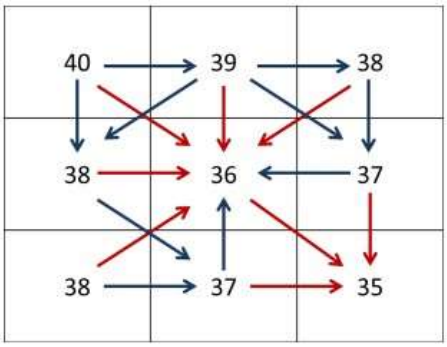

Figure 68: MFD algorithm illustration

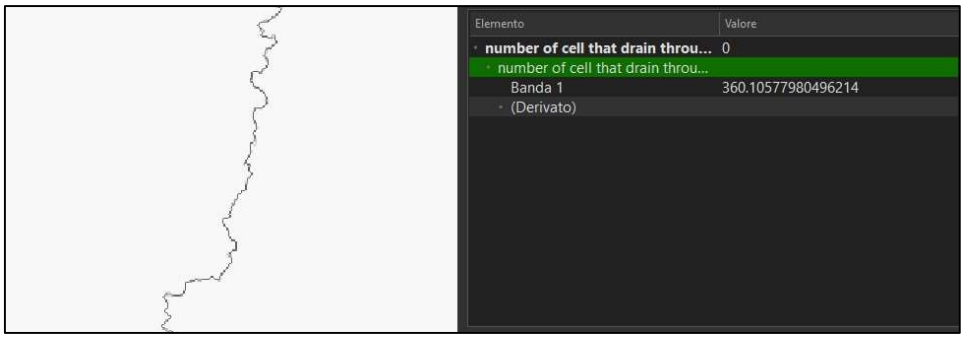

Figure 69: Number of Cells that Drain through each Direction

"Stream segments" reports the value "no data" outside the drainage directions, but reports within the grid, for each segment, the subbasin code. Fig. 70 shows how the segments are of different colors; in fact, QGIS categorizes according to the subbasin ID the segments and assigns them a color, thus also giving immediate information about the segments membership.

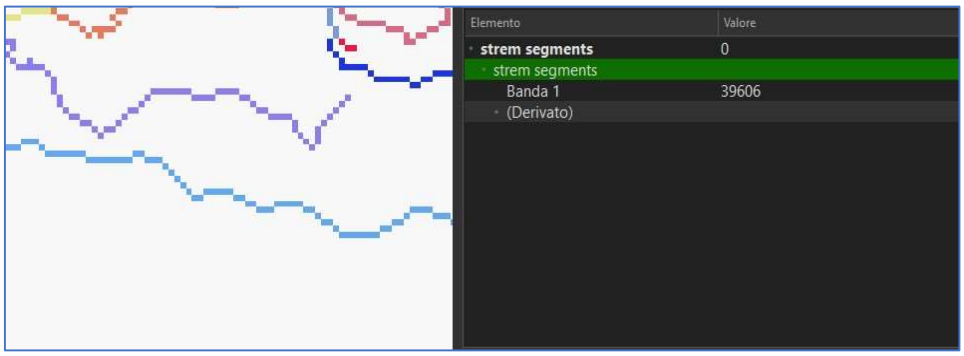

Figure 70: Stream segments

"Drainage Direction" contains the flow directions calculated by the MFD algorithm.

Figure 71: Drainage Direction

2. ***r.water outlet***: Takes as input the "Drainage direction" file and the coordinates of the closure section so as to determine the catchment area.

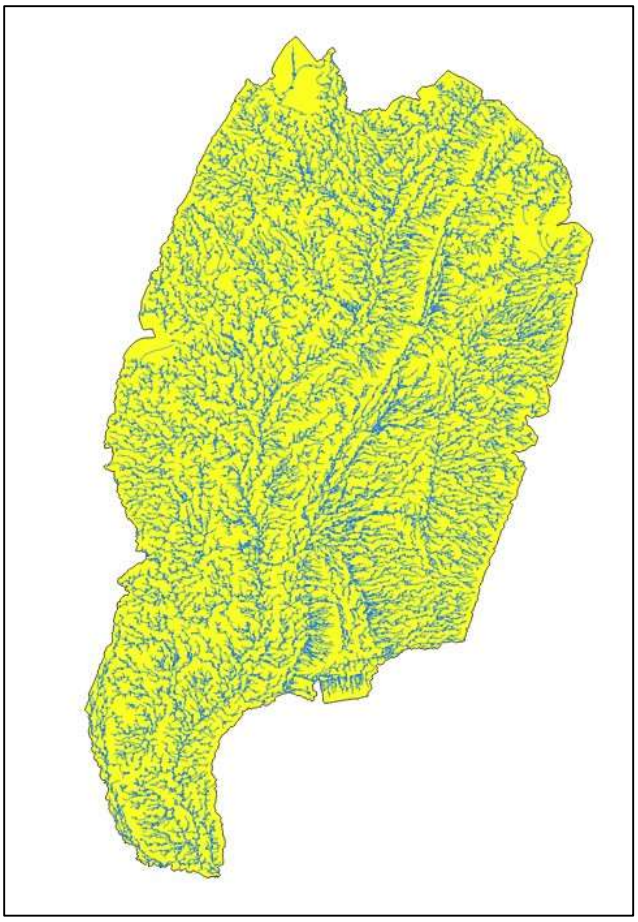

Figure 72: Basin extraction of "Meteo Valle" site

The outputs provided by these tools make it possible to determine:

- the area and perimeter of the basin;
- the statistics of the basin;

Area and perimeter are easily calculated by the Calculator found in the attributes table. As for the statistics, namely:

- Minimum Elevation;
- Maximum Elevation;
- Average Elevation;
- Variance of the Elevation;
- Standard deviation of the Elevation;

The function "Raster statistics for polygons" was used, which will take the DEM of the area as input.

The last operation carried out within QGIS will be the determination of the basin's main rod and its elevation and length information. By taking advantage of the combination of orthophotos, hydrographic grid and "short path (from point to point)" function, it will be possible to extract the main basin rod. By definition of main basin rod (https://www.youtube.com/watch?v=thGPcIWlSik&ab_channel=SoluzioniIngegneristiche):

"longest path in the hydrographic network connecting the water divide with the closure section"

It was necessary, at the end of the execution of the "short path (from point to point)" algorithm, to apply manual graphical corrections in order to be able to ensure that the longest path is taken.

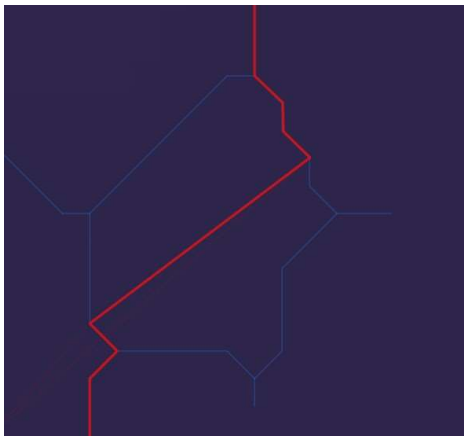

Figure 73: Path Correction

The union of these operations provides the Hydrographic maps found in the following chapters, and the ".csv file" containing the various elevations of the main rod along the longitudinal section. The elevations will be processed by a code in MATLAB (found in the appendix) that will provide:

- The Longitudinal Profile of the various water bodies along the main drainage direction;
- The number of drops that the streams make for a predetermined Δz and Δx;
- Mean slope along the longitudinal profile;
- Mean step spacing.

With regard to Δx and Δy it was decided to maintain, for each site analyzed, a Δz of 15 cm which is about the height of the tie-rod present in these streams; while for Δx it was decided to use 10 cm in the tributaries (Where the steps should be closer) and Δx of 20 cm in the main (where the steps should have a larger mean step spacing). These considerations find support in Judd (1964), where jump spacing is inversely proportional to the slope of the tract.

6. Results and Discussion

This chapter discusses the results of photogrammetric processing for each area of interest, identifies the critical issues and problems encountered, and highlights the accuracies achieved through the combination of GPS survey and aerophotogrammetry.

In the description of the rigorous procedure used in this thesis work, no marked distinction is made in the data processing between the different areas; this is because the proposed methodology is applicable in a broad range of contexts.

6.1. Meteo Valle

"Meteo Valle" was the first area surveyed. This first experience allowed me to identify the optimal flight parameters and the appropriate camera setting, depending on the geometry of the area to be surveyed and the weather conditions.

The final flight took place with partially cloudy sky, which, despite not being one of the best conditions, provided excellent shots.

The main drawback of the application to this area was the presence of the tall coniferous trees that required a flight height of the drone of 56 m in order to avoid the drone crashing.

Figure 74: Climatic conditions in the morning of 07/01/22

Figure 75: Conifers in "Meteo Valle" area

Tests at "Meteo Valle" resulted in finding the right size of ground markers and the optimal material for their printing. The size of the markers used in the project is A3 size made of recycled paper, so that they are visible in Metashape under all light conditions. During the 07/01/22 surveys, using GPS antenna, problems with the RTK correction occurred which made the marker coordinates very inaccurate, this made the External Orientation of the model affected by large errors. As a solution to this issue, replacement GPS surveys were adopted, based on visible and fixed points present within the survey area and visible in the photos, this solution resulted in a final accuracy of the model of approximately 5 cm.

Photogrammetry of the area is based on 123 photos taken on 07/01/22, late morning, which covered an area of 10'500 m^2.

Starting from these images, the software provided the sparse cloud shown in Fig. 76, which was gathered using the parameters in Tab. 5.

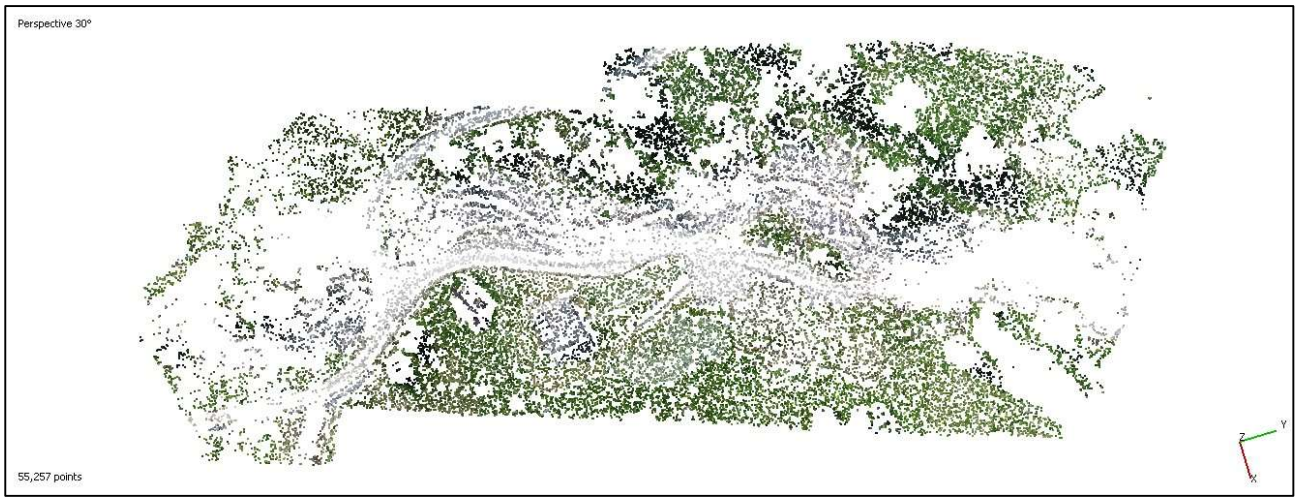

Figure 76: Sparse Cloud of "Meteo Valle"

Resolution [pixel]	5280x3956	Tie points	55’257
Flight height [m]	56.4	Projections	298’077
Pixel size [um]	3.28x3.28	Reprojection error [pixel]	0.616

Table 5: Sparse Cloud of "Meteo Valle" parameters

The optimization of the alignment will later provide an estimate of the error on the model, based on the coordinates of the markers, in Fig. 77 it is possible to have both numerical and graphical feedback of this magnitude.

Figure 77: GCP locations and error estimates of “Meteo Valle”.
Z error is represented by ellipse color. X, Y errors are represented by ellipse shape.
Estimated GCP locations are marked with a dot or crossing.

Count	X error [cm]	Y error [cm]	Z error [cm]	XY error [cm]	Total [cm]
8	2.4534	1.93338	0.800489	3.12364	3.22458

Table 6: Control points RMSE of "Meteo Valle".
X - Easting, Y - Northing, Z - Altitude.

Count	X error [cm]	Y error [cm]	Z error [cm]	XY error [cm]	Total [cm]
4	2.50049	3.07246	4.18305	3.96137	5.76111

Table 7: Check points RMSE of "Meteo Valle".
X - Easting, Y - Northing, Z - Altitude

Fig. 77 shows the distribution of points; it is evident they do not cover the whole area. This is due to the impossibility of using the coordinates of the markers surveyed during aerophotography and the use of fixed points visible from the photos for the GPS survey, which unfortunately were mainly located only in the lower right.

Figure 78: Substitute survey

Starting from the sparse cloud, the dense cloud in Fig. 79 consisting of 106'851'264 points will then be created.

Figure 79: Dense Cloud of "Meteo Valle"

At the next step, the mesh shown in Fig. 80 consisting of 960'964 vertices and 1'920'022 faces was produced, on which the texture in Fig. 81 was laid.

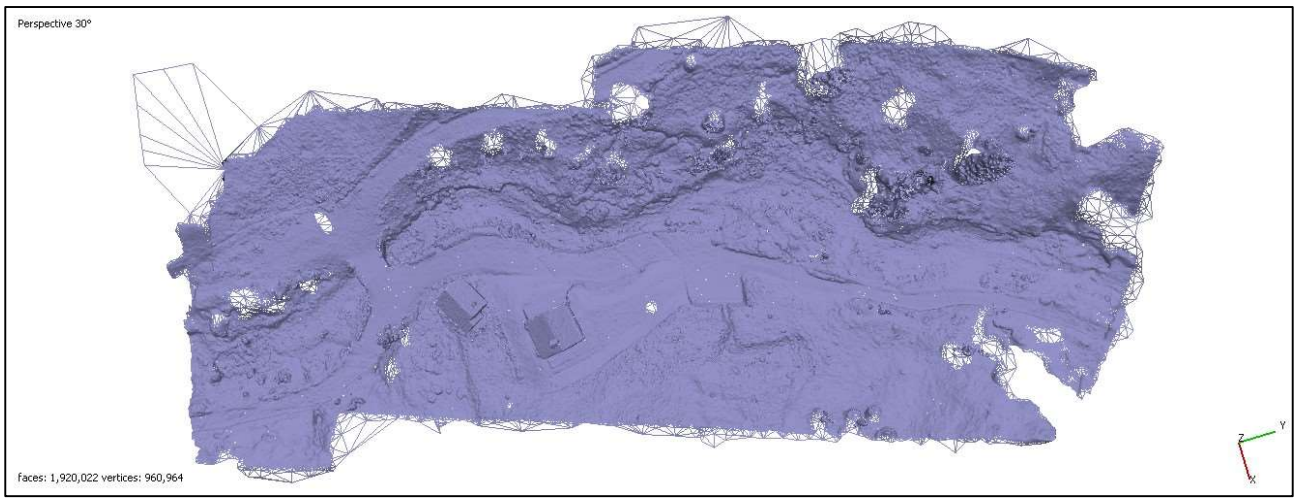

Figure 80: Mesh of "Meteo Valle"

Figure 81: Texture of "Meteo Valle"

Fig. 82 shows the Orthomosaic representing “Meteo Valle” with ground resolution of 7.21 mm/pixel, which provides information on the status of the stream on 07/01/22. The Orthomosaic revealed the presence of water, the riverbed, and the pattern followed by the stream; also clearly visible are the areas around the stream.

In Fig. 84, the DEM made with a resolution of 1.44 cm/pixel is presented, from which a visual feedback of the distribution of elevations within the survey area can be obtained. It is possible to see how the reach “Meteo Valle” goes from elevation 1’776 meters on the ellipsoid to 1’754 in a quite gradual way, i.e., without abrupt jumps along the elevation profile.

On the basis of the cartographic data within the “.tiff file” of the DEM, it was also possible to reconstruct the contour lines of the area shown in Fig. 83 with 2 m pitch and the hydrographic map in Fig. 85.

Figure 82: Orthomosaic of "Meteo Valle" with ground resolution di 7.21 mm/pixel

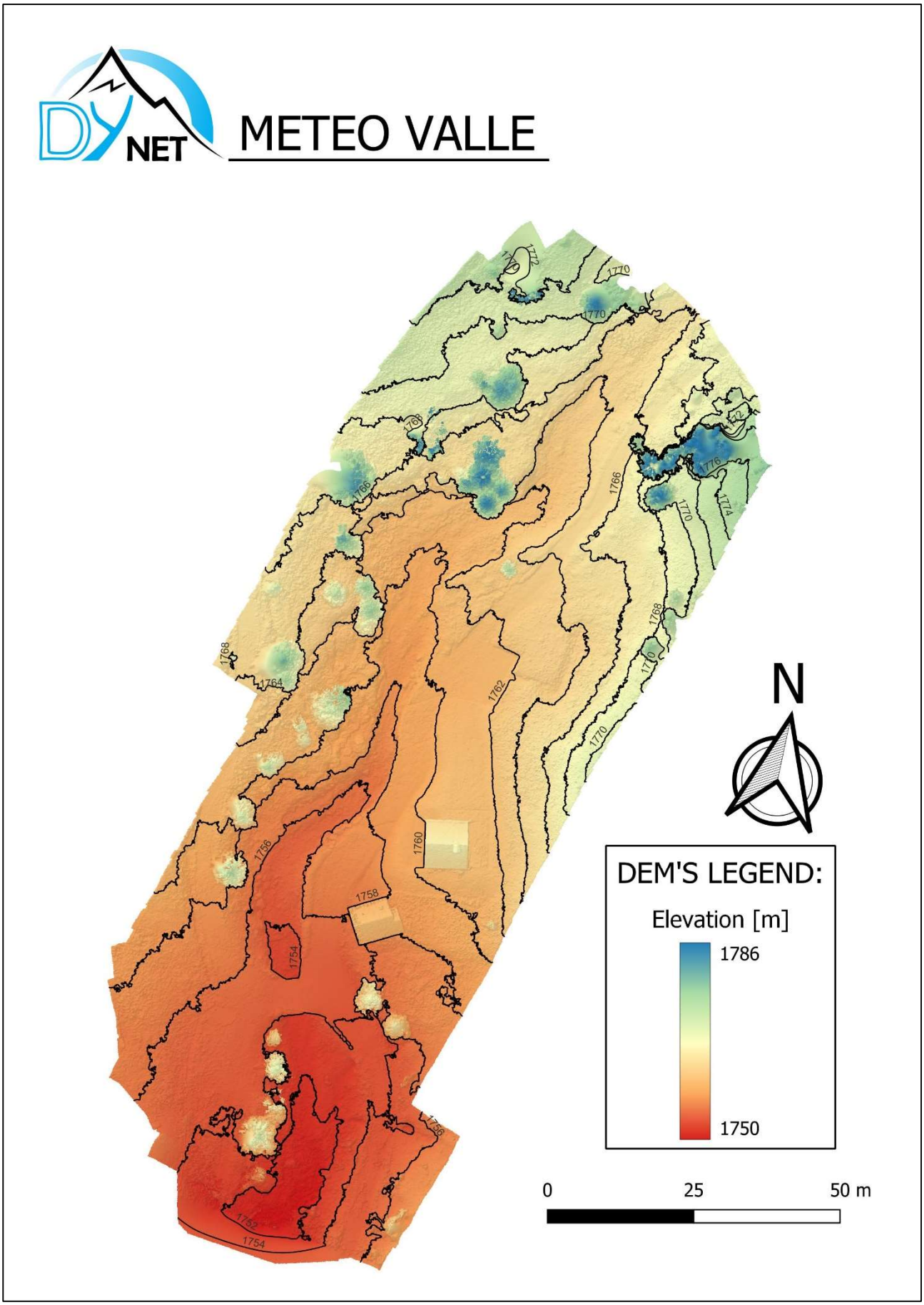

Figure 83: Contour lines of "Meteo Valle" with step of 2m

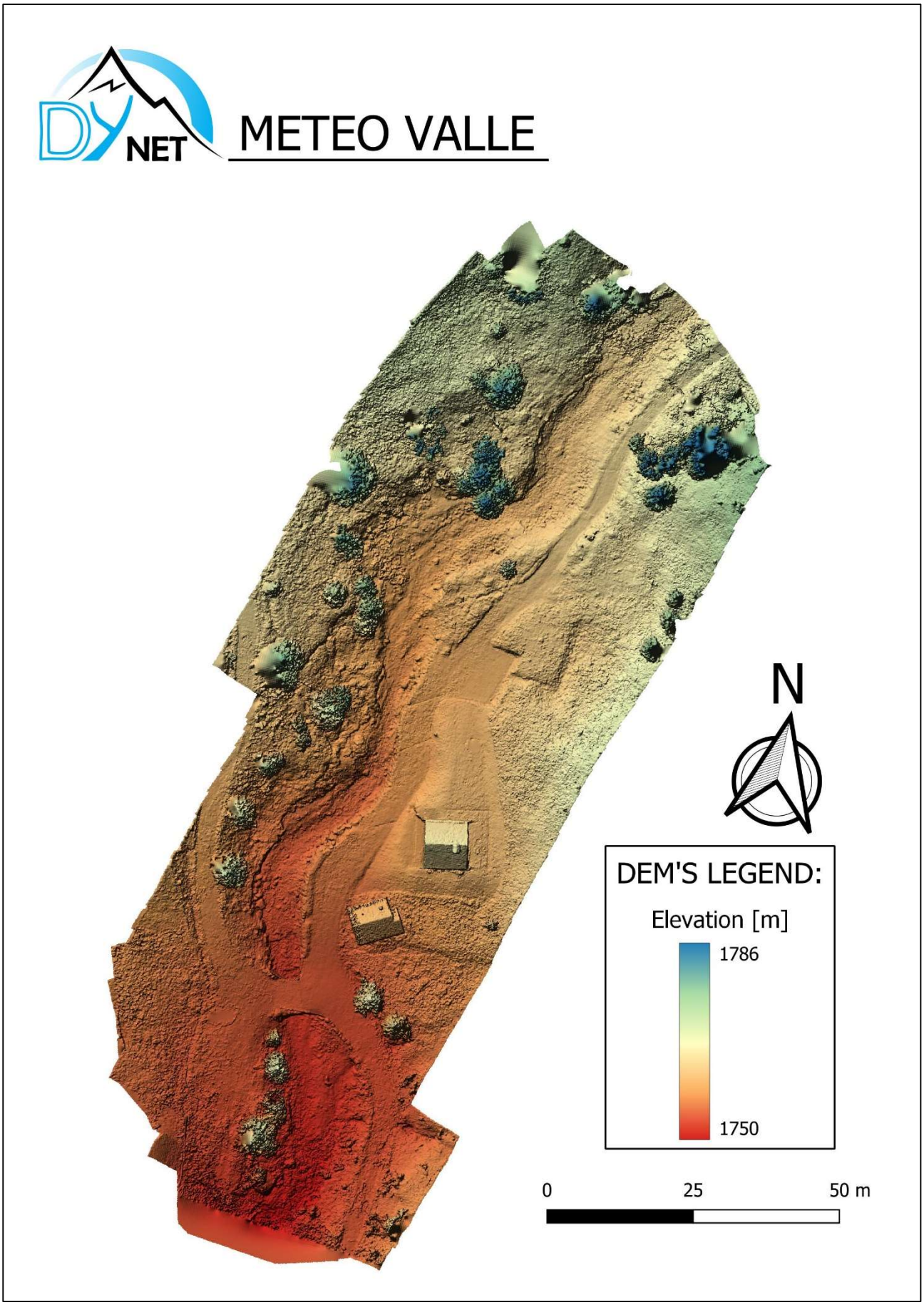

Figure 84: DEM of "Meteo Valle" with ground resolution di 1.44 cm/pixel

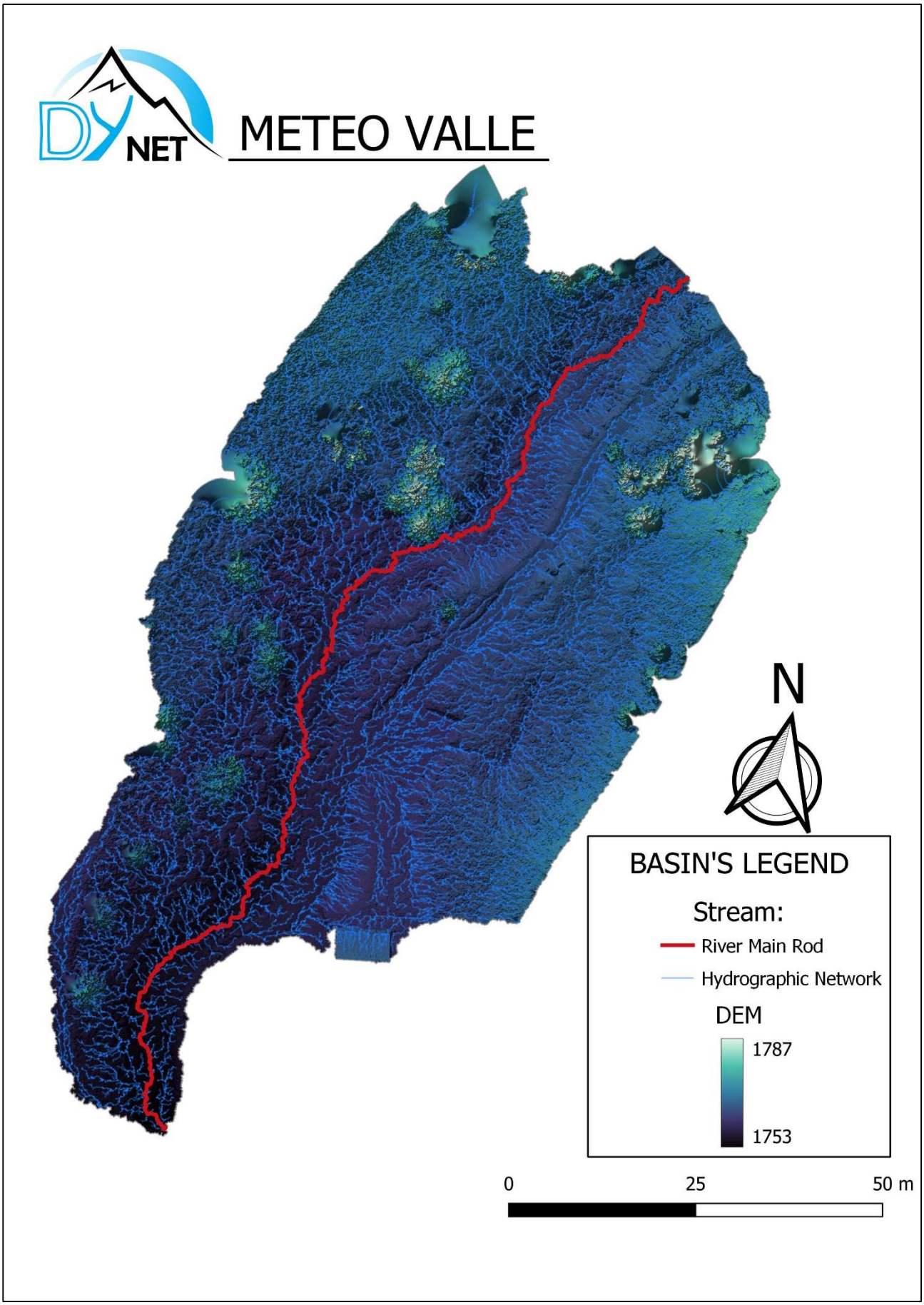

Figure 85: Hydrographic map of "Meteo Valle"

Fig. 85 is only a simplification of the basin and drainage network of "Meteo Valle", as these data are limited to drone aerophotogrammetric acquisitions. In any case, Fig. 85 provides useful information regarding the location of the main rod, i.e., where the main runoff direction is located, and the areas around it that contribute to the runoff.

Tab. 8 shows the statistics of the surveyed portion of the basin.

Area [m^2]	Perimeter [m]	Min. Altitude [m]	Max. Altitude [m]	Mean Altitude [m]	Altitude's Variance [m^2]	Altitude's Standard Deviation [m]
6'630	710	1'753	1'786	1'765	32	6

Table 8: Meteo Valle" Basin Statistics

Finally, thanks to the elevation data of the main rod, the elevation profile was obtained and then modified with a "pit filling" algorithm. Assuming the step can be identified by elevation of drop of 15 cm (or more) within a long distance Δx of 20 cm, the number of jumps was obtained (Fig. 86). I report in Tab. 9 the characteristics of the longitudinal profile of "Meteo Valle".

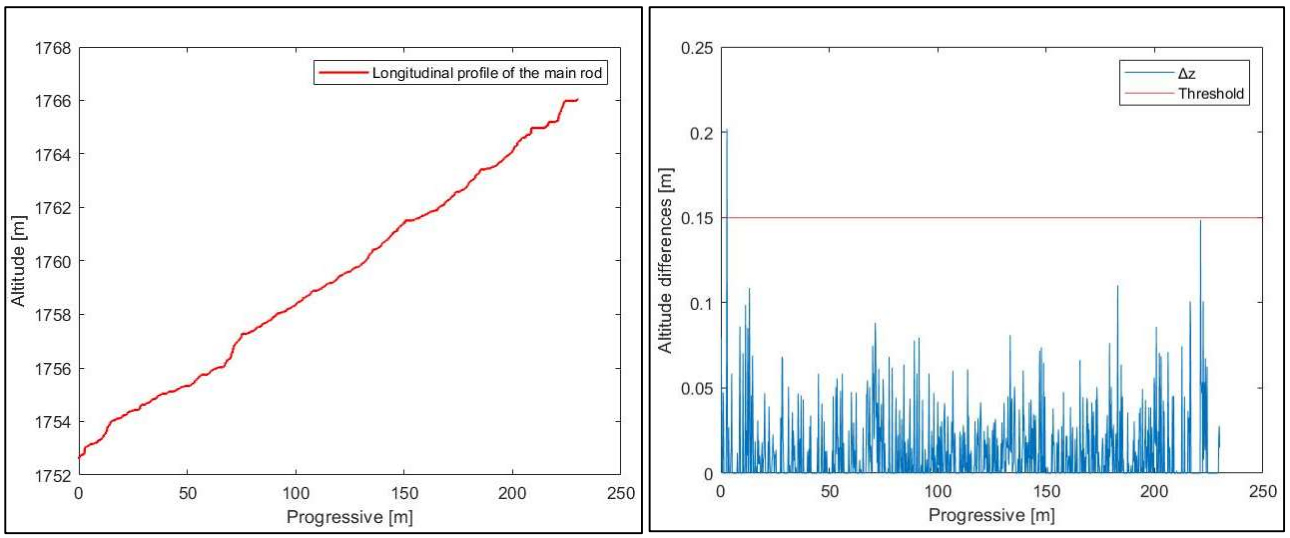

Figure 86: On the left side the longitudinal profile of the section of "Meteo Valle" on the right side the steps along the longitudinal profile

Slope	Mean Step Spacing (MSS) [m]	Δx [cm]	Δz [cm]	N°Step
0.06	230	20	15	1

Table 9: N° of step at "Meteo valle" for a prescribed Threshold value

"Meteo Valle" is too wide to have a step-and-pool configuration, in fact by reducing Δx the number of steps that the algorithm finds drops to zero while by increasing Δx those that are detected are no longer steps and pools, but high-turbulence riffles or partial steps that do not experience the full flow rate.

Figure 87: On the left the only Step-pool found at "Meto Valle" for Δx= 20cm, while on the right a riffe found for Δx= 40cm

6.2. Affluente 1

In the early afternoon of 07/01/22, survey operations were held for "Affluente 1". This second model is based on of 87 photos and covers an area of 9'480 m^2. From these data Agisoft Metashape provided a sparse cloud, shown in Fig. 88, which was gathered using parameters in Tab. 10.

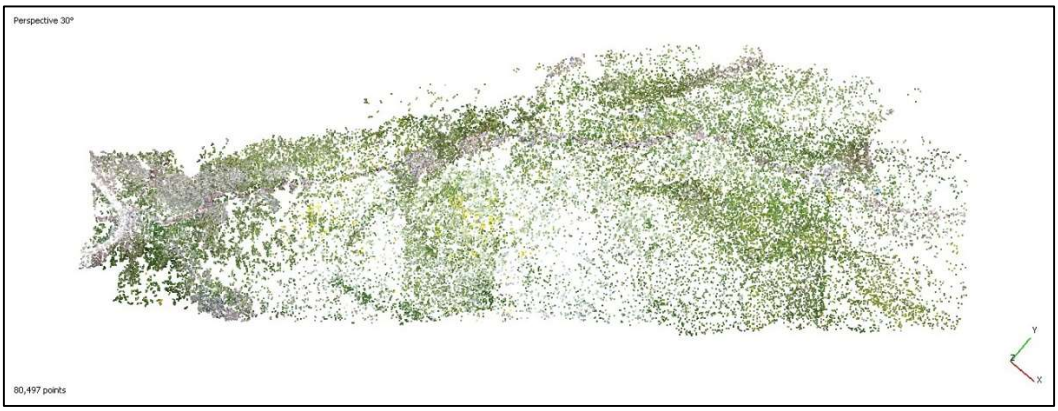

Figure 88: Sparse Cloud of "Affluente 1"

Resolution [pixel]	5280x3956	Tie points	80'497
Altezza di volo [m]	33.3	Projections	198'210
Pixel size [um]	3.28x3.28	Reprojection error [pixel]	1.16

Table 10: Sparse Cloud of "Affluente 1" parameters

From the optimization of the alignment, the accuracy of the survey is obtained:

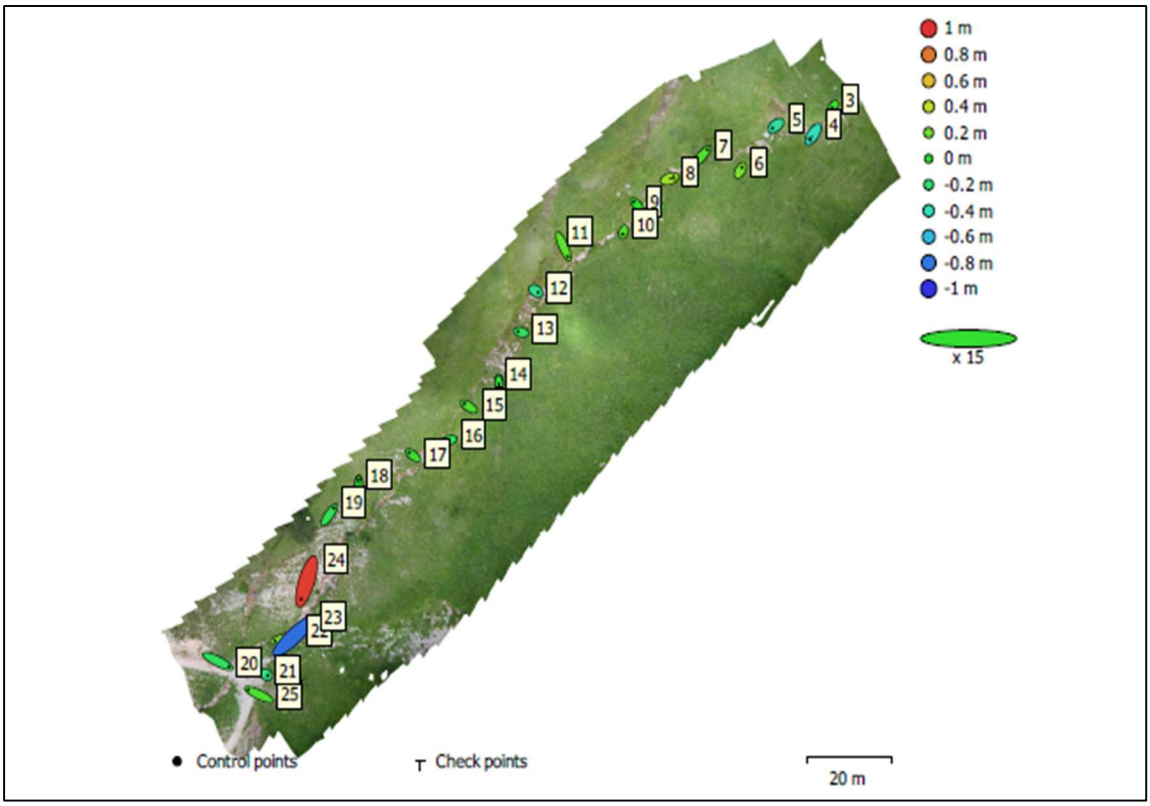

Figure 89: GCP locations and error estimates of "Affluente 1".
Z error is represented by ellipse color. X, Y errors are represented by ellipse shape.
Estimated GCP locations are marked with a dot or crossing.

Count	X error [cm]	Y error [cm]	Z error [cm]	XY error [cm]	Total [cm]
18	21.0716	19.8025	33.4897	28.9163	44.2461

Table 11: Control points RMSE of "Affluente 1".
X - Easting, Y - Northing, Z - Altitude.

Count	X error [cm]	Y error [cm]	Z error [cm]	XY error [cm]	Total [cm]
5	10.4129	13.3292	22.8407	16.9144	28.4217

Table 12: Check points RMSE of "Affluente 1".
X - Easting, Y - Northing, Z – Altitude

This is the model with the largest error, mainly due to the adverse weather conditions, manifested in the afternoon, characterized by intense wind that caused the drone batteries to exhaust quickly. An additional problem was due to the dense and high vegetation that did not allow a homogeneous distribution of the ground Markers as can be seen from Fig.89. Fig. 89 shows how points 23 and 24 are affected by an error of an order of magnitude greater than the others points. This is due to the presence of a large elevation difference between the beginning and the end of the waterfall, that made both GPS acquisition of these points and RTK reception difficult, as the vertical rock face limited signal acquisition.

Figure 90: Climatic conditions in the afternoon of 07/01/22

Starting from the sparse cloud, the dense cloud in Fig. 91 consisting of 145'982'058 points was then created.

Figure 91: Dense Cloud of "Affluente 1"

This is followed by the restitution of the mesh consisting of 1'425'592 vertices and 2'851'192 faces, on which the texture in Fig. 93 was laid.

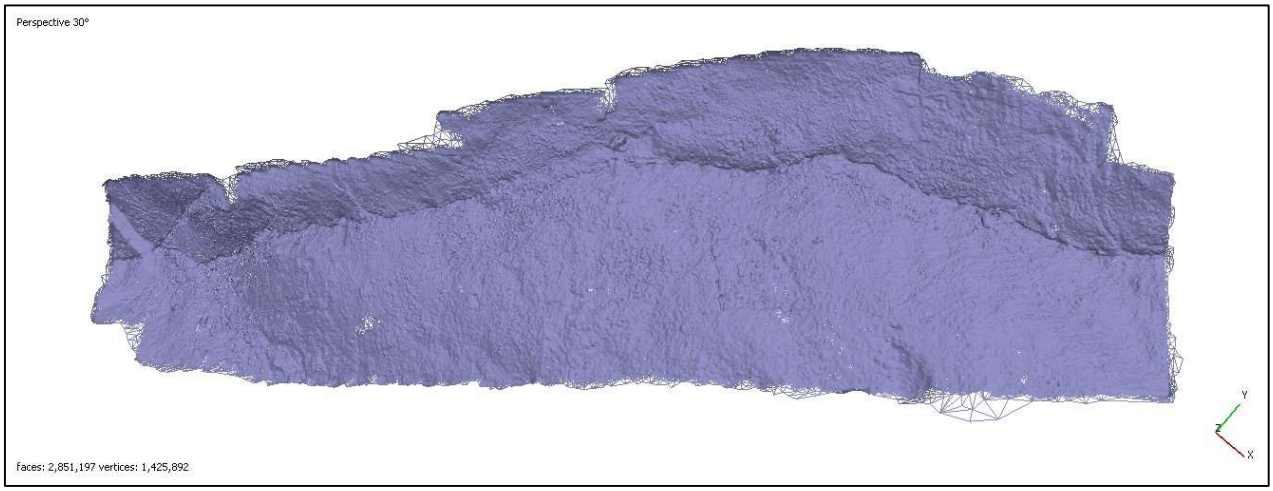

Figure 92: Mesh of "Affluente 1"

Figure 93: Texture of "Affluente 1"

Fig. 94 shows the Orthomosaic representing “Affluente 1” with ground resolution of 6.22 mm/pixel, which provides information on the state of the stream that was almost completly dry and the pattern that the stream follow; the areas around the stream are also clearly visible.

Fig. 96, shows the DEM with a resolution of 1.24 cm/pixel, from which a visual feedback of the distribution of elevations within the survey area can be obtained. It can be seen that “Affluente 1” goes from elevation 2’128 m on the ellipsoid to 2033 in a gradual manner from elevation 2’128 m to 2’088, i.e. without sharp jumps along the elevation profile, while from 2’088 to 2’033 the slope becomes much steeper, as appreciable also from Fig. 95.

On the basis of the cartographic data within the “.tiff file” of the DEM, it was also possible to reconstruct the contour lines of the area shown in Fig. 95 with 2 m step and the hydrographic map in Fig. 97.

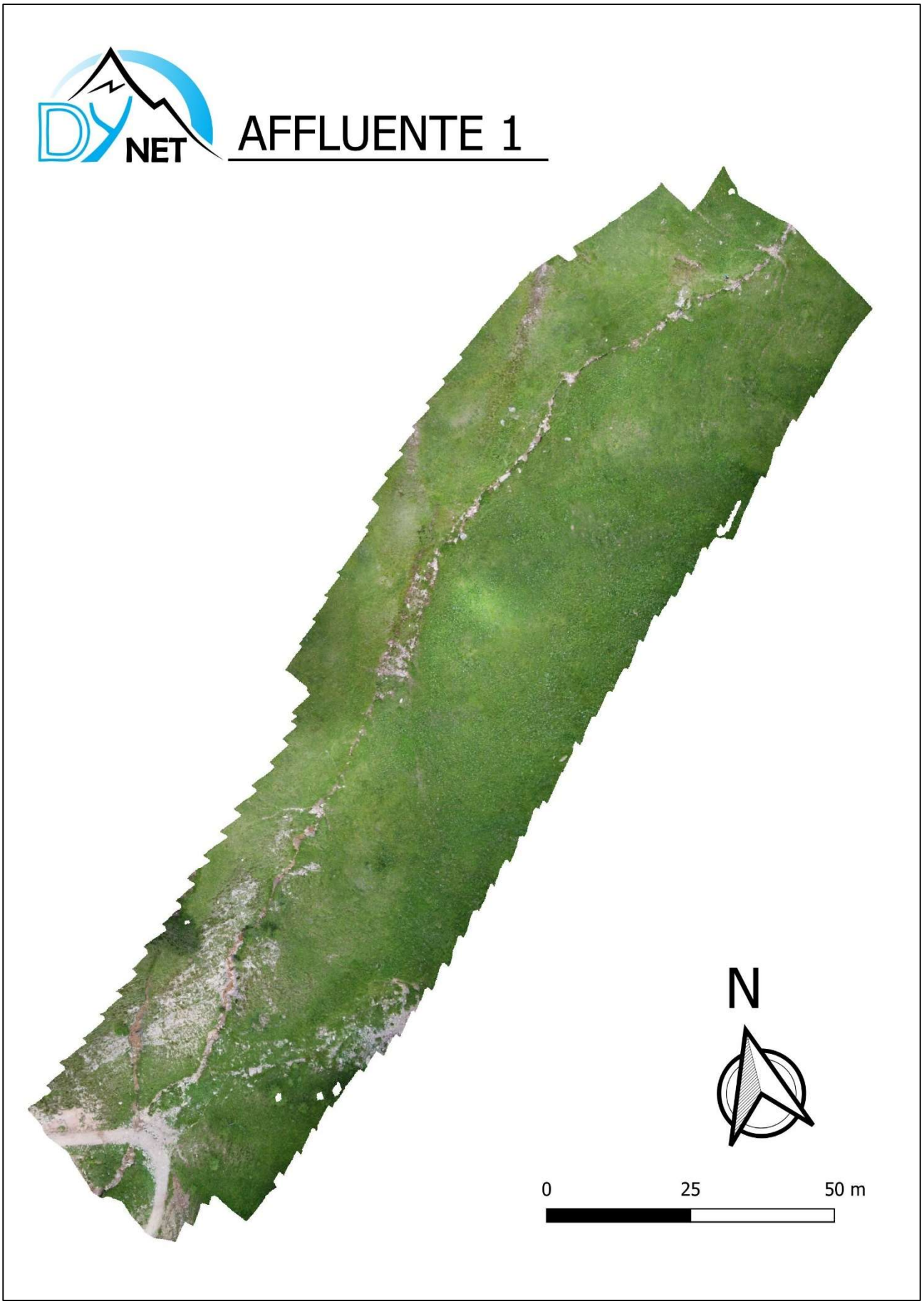

Figure 94: Orthomosaic of "Affluente 1" with ground resolution di 6.22 mm/pixel

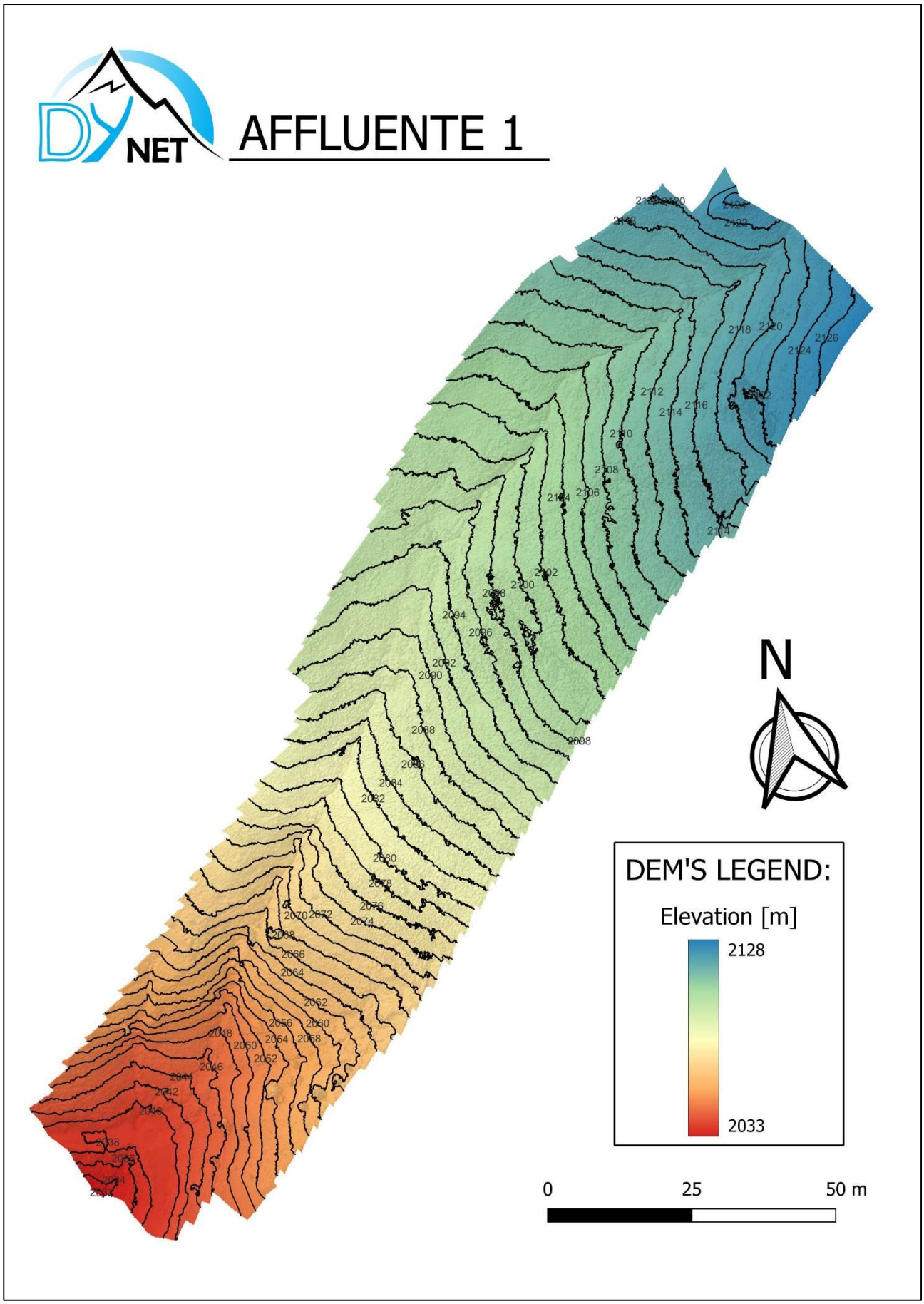

Figure 95: Contour lines of "Affluente 1" with step of 2m

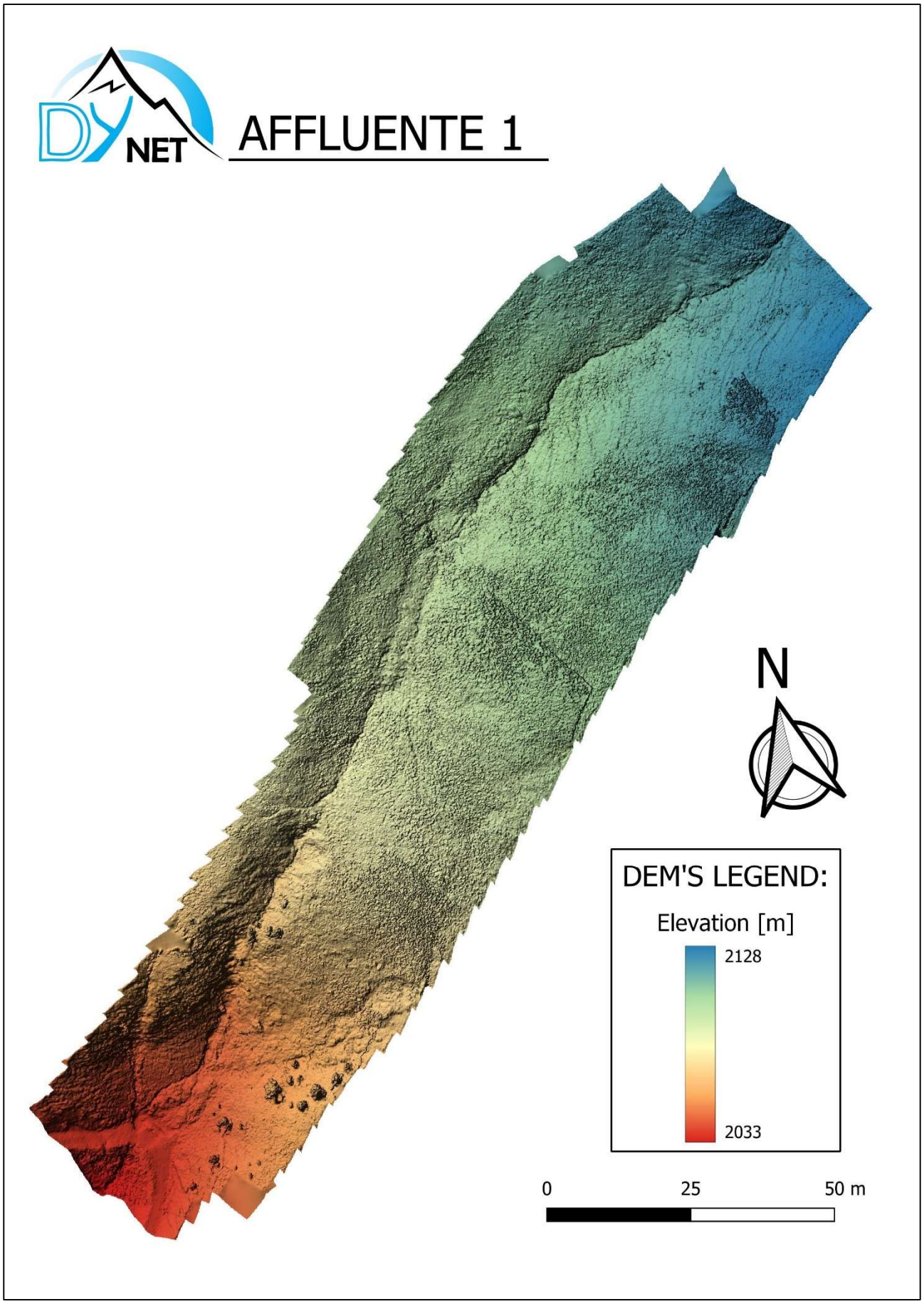

Figure 96: DEM of "Affluente 1" with resolution of 1.24 cm/pixel

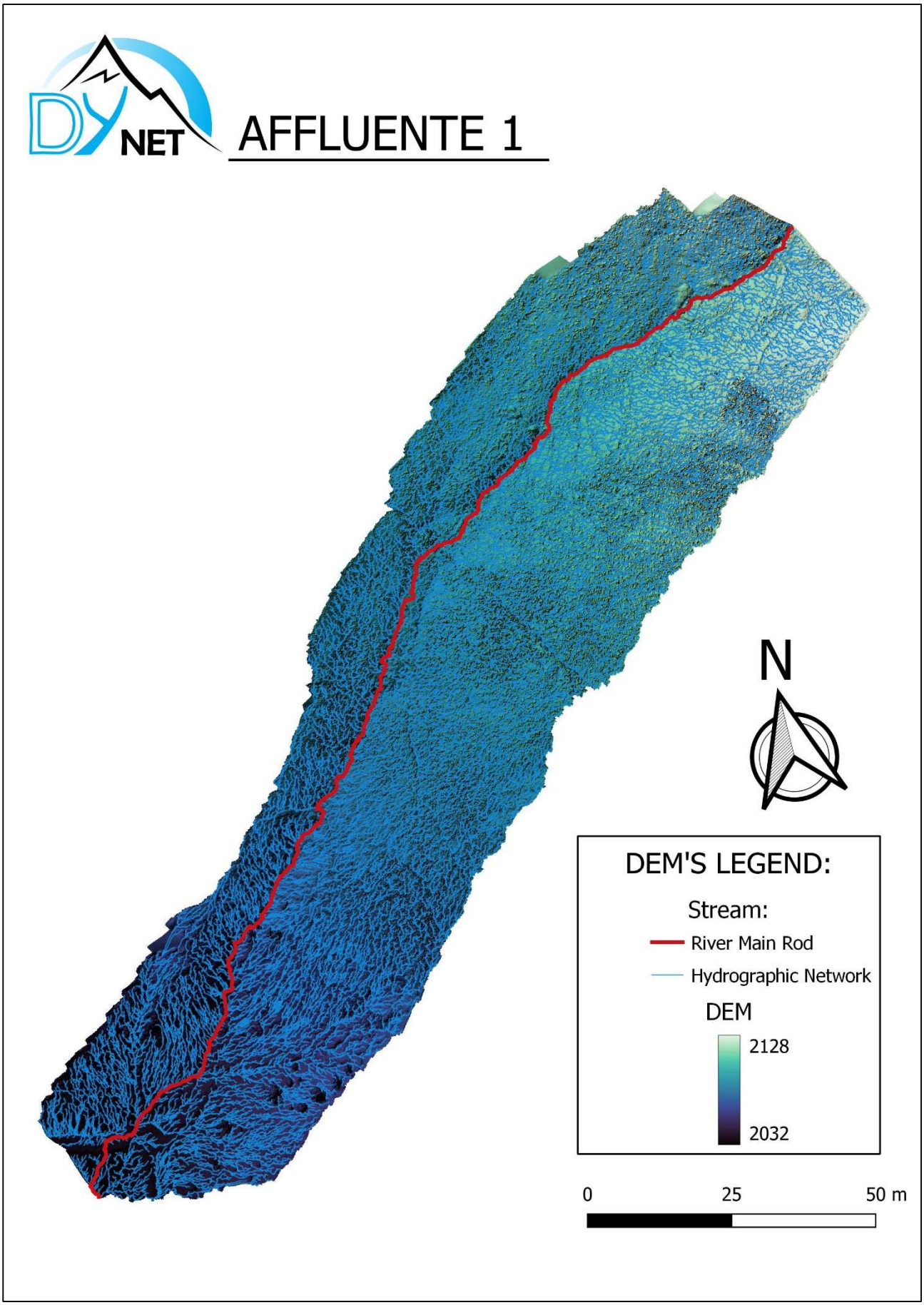

Figure 97: Hydrographic map of "Affluente 1"

Fig. 97 is only a simplification of the basin and drainage network of "Affluente 1", as these data are limited to drone aero-photogrammetric acquisitions and the dense vegetation due to the summer season distorts the ground drainage network. In any case, Fig. 97 provides useful information regarding the location of the main rod, i.e., where the main runoff direction is located, and the areas around it that contribute to the runoff.

Tab. 13 shows the statistics of the surveyed portion of the basin.

Area [m^2]	Perimeter [m]	Min. Altitude [m]	Max. Altitude [m]	Mean Altitude [m]	Altitude's Variance [m^2]	Altitude's Standard Deviation [m]
8'913	860	2'032	2'128	2'088	590	24

Table 13: "Affluente 1" Basin Statistics

Finally, thanks to the elevation data of the main rod, the elevation profile was obtained and then modified with a "pit filling" algorithm. Assuming the step can be identified by elevation of drop of 15 cm (or more) within a long distance Δx of 10 cm, the number of jumps was obtained (Fig. 98). I report in Tab. 14 the characteristics of the longitudinal profile of "Affluente 1".

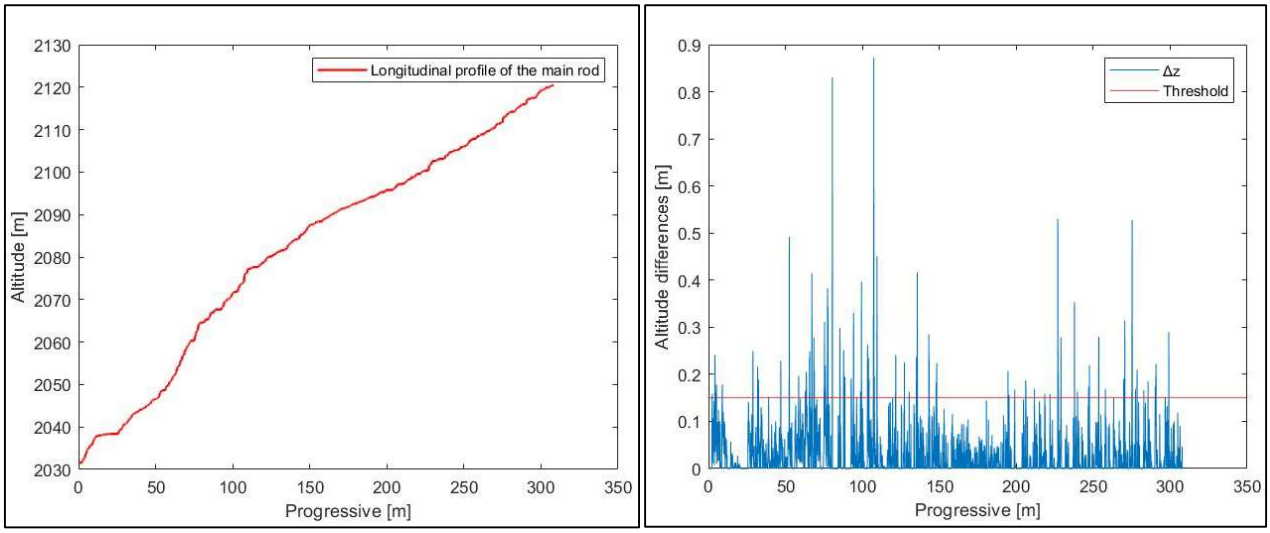

Figure 98: On the left side the longitudinal profile of the section of "Affluente 1" on the right side the steps along the longitudinal profile

Slope	Mean Step Spacing (MSS) [m]	Δx [cm]	Δz [cm]	N°Step
0.29	2.93	10	15	105

Table 14:N° of step at " Affluente 1" for a prescribed Threshold value

The grass at "Affluente 1" not only caused errors in the determination of the drainage network, but also caused problems in the determination of some of the steps. Fig.99 shows that extra steps are detected due to the grass wires (A total of 12 jumps).

Another form of disturbance is the waterfall which causes extra steps because of the steep drop in longitude that is decomposed by the algorithm into multiple steps (12 total).

Figure 99: On left an example of extra point caused by grass and on right side the problem due to the waterfall at "Affluente 1"

6.3. Affluente 3

This area is located in an incision between two grasslands, which did not allow for optimal network and satellite signal reception during surveying. The morphology of the area caused problems especially downstream of the tributary, where the slope located to the south limited the acquisition of the RTK correction signal, giving accuracies on marker coordinates in the order of one meter. Therefore, 2 measurement campaigns (07/08/22 and 07/25/22) were needed in order to collect the necessary data for modelling the area, then the tributary was divided in an upstream chunk ("Affluente 3 upstream") and a downstream chunk ("Affluente 3 downstream"). Unfortunately, since the two acquisitions were performed with different flight parameters, merging them into a single piece quadrupled the error from less than 5 cm to 20 cm. Therefore, it was decided to process the two parts separately with very high levels of accuracy given the small extent of the areas.

Fortunately, both survey campaigns took place under clear sky conditions, thus providing very good quality images.

Figure 100: On the left the weather conditions during the survey of the upstream part of "Affluente 3" while on the left the conditions for the valley part

For surveying the area, 66 photos were taken in the upstream area and 45 in the downstream area and covers a total area of 13430 m^2.

Sparse clouds (Fig. 101) and their survey parameters (Tab.15-16) are given below.

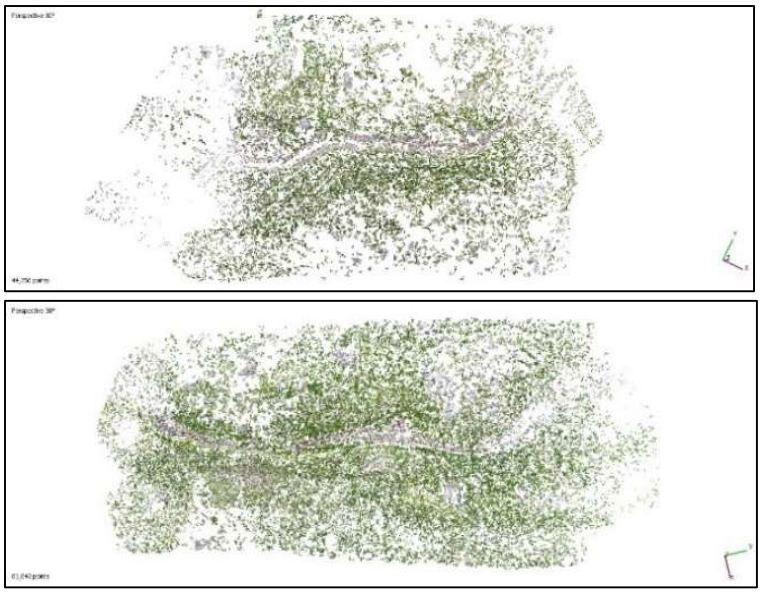

Figure 101: On the upper part the sparse cloud of downstream part of "Affluente 3" while on bottom part the upstream part

Resolution	5280x3956	Tie points	44’756
Flight height [m]	38.6	Projections	127’705
Pixel size [um]	3.28x3.28	Reprojection error	0.701 pixel

Table 15: Sparse Cloud of “Affluente 3 downstream" parameters

Resolution	5280x3956	Tie points	81’843
Flight height [m]	36	Projections	215’975
Pixel size [um]	3.28x3.28	Reprojection error	0.572 pixel

Table 16: Sparse Cloud of “Affluente 3 upstream" parameters

From the optimization of the alignment, the accuracy of the survey is achieved:

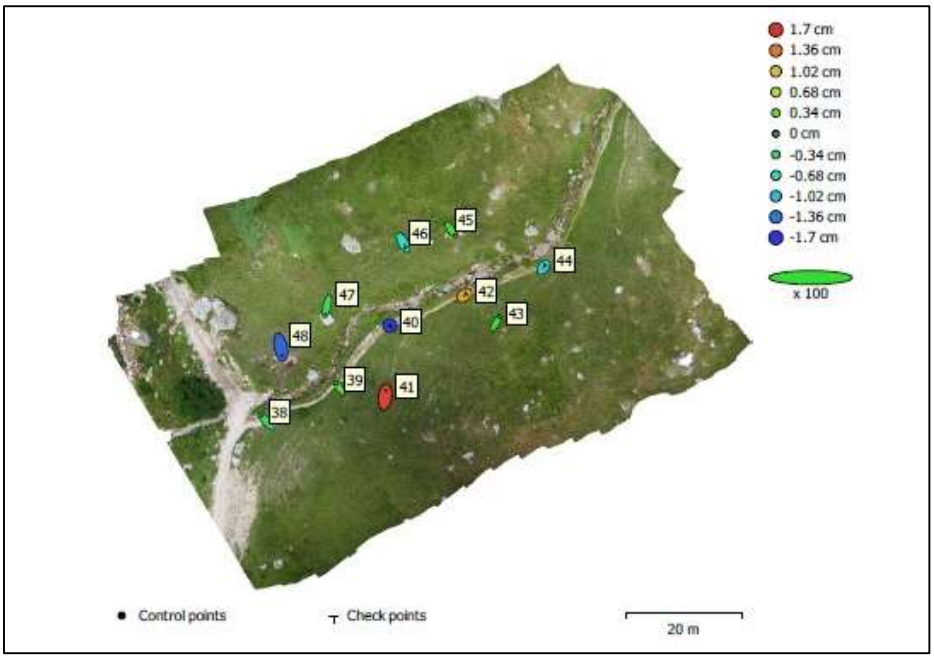

Figure 102: GCP locations and error estimates of “Affluente 3 downstream”.
Z error is represented by ellipse color. X, Y errors are represented by ellipse shape.
Estimated GCP locations are marked with a dot or crossing

Count	X error [cm]	Y error [cm]	Z error [cm]	XY error [cm]	Total [cm]
7	0.942859	2.1291	0.829497	2.32853	2.47187

Table 17: Control points RMSE of "Affluente downstream".
X - Easting, Y - Northing, Z - Altitude.

Count	X error [cm]	Y error [cm]	Z error [cm]	XY error [cm]	Total [cm]
4	0.653971	1.00478	1.15824	1.19886	1.6697

Table 18: Check points RMSE of "Affluente downstream".
X - Easting, Y - Northing, Z - Altitude.

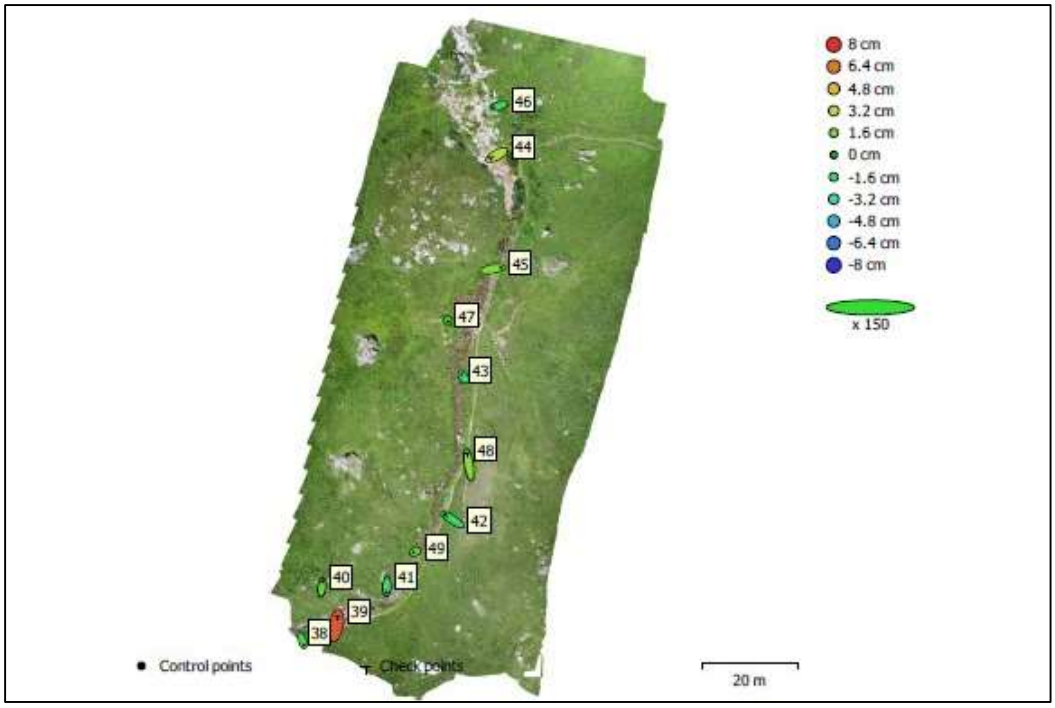

Figure 103: GCP locations and error estimates of "Affluente 3 upstream".
Z error is represented by ellipse color. X,Y errors are represented by ellipse shape.
Estimated GCP locations are marked with a dot or crossing

Count	X error [cm]	Y error [cm]	Z error [cm]	XY error [cm]	Total [cm]
8	0.995999	0.964088	1.05476	1.38617	1.74184

Table 19: Control points RMSE of "Affluente upstream".
X - Easting, Y - Northing, Z - Altitude.

Count	X error [cm]	Y error [cm]	Z error [cm]	XY error [cm]	Total [cm]
4	1.46916	2.24558	4.02679	2.68348	4.83902

Table 20: Check points RMSE of "Affluente upstream".
X - Easting, Y - Northing, Z - Altitude.

Restitution of the dense cloud follows, composed of 42'010'226 points for the downstream side and 60'218'753 points upstream, followed by the mesh composed of 599'723 vertices and 1'197'517 faces downstream and 1'254'460 vertices and 2'507'971 faces upstream, on which the texture in Fig. 106 was laid.

Figure 104: On the upper part the dense cloud of downstream part of "Affluente 3" while on bottom part the upstream part

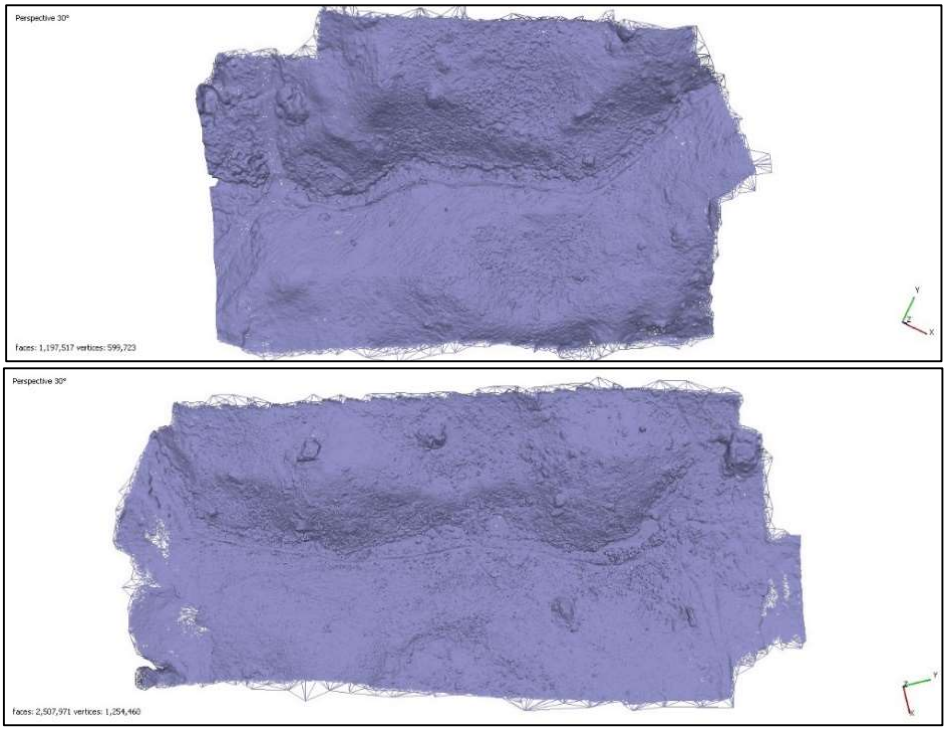

Figure 105: On the upper part the mesh of downstream part of "Affluente 3" while on bottom part the upstream part

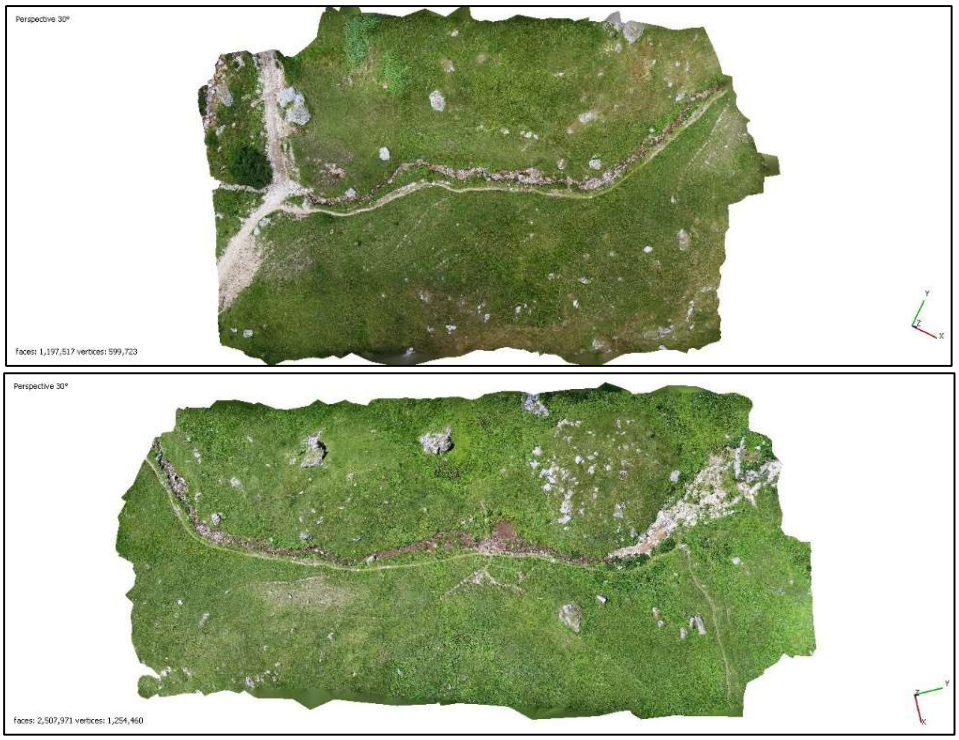

Figure 106: On the upper part the texture of downstream part of "Affluente 3" while on bottom part the upstream part

Fig. 107 shows the Orthomosaics representing “Affluente 3” with ground resolution of 7.18 mm/pixel for the upstream part and 7.73 mm/pixel for the downstream part, which provides visual information about the status of the stream. Appreciable is the fact that on 07/08/22 the tributary had water available, information that can be deduced from the color of the stream bed, while on 07/25/22 it was almost completely dry. Also clearly visible are the areas around the watercourse and the path taken by the tributary.

In Fig. 109, the DEM made with a resolution of 1.44 cm/pixel in the upstream area and 1.55 cm/pixel in downstream area is presented, from which visual feedback of the distribution of elevations within the survey area can be obtained. “Affluente 3” is located within a highly incised area since the area affected by the stream is colored with the lower end of the color scale present in the DEM legend while the surrounding areas are colored with the upper end. Moreover, the different slope of the two parts can be appreciated thanks to Fig. 108 where it is evident that the creek bed in the downstream part is more sloping.

Based on the cartographic data within the “.tiff file” of the DEM, it was also possible to reconstruct the contour lines of the area shown in Fig 108 with 2 m step and the hydrographic map in Fig. 110.

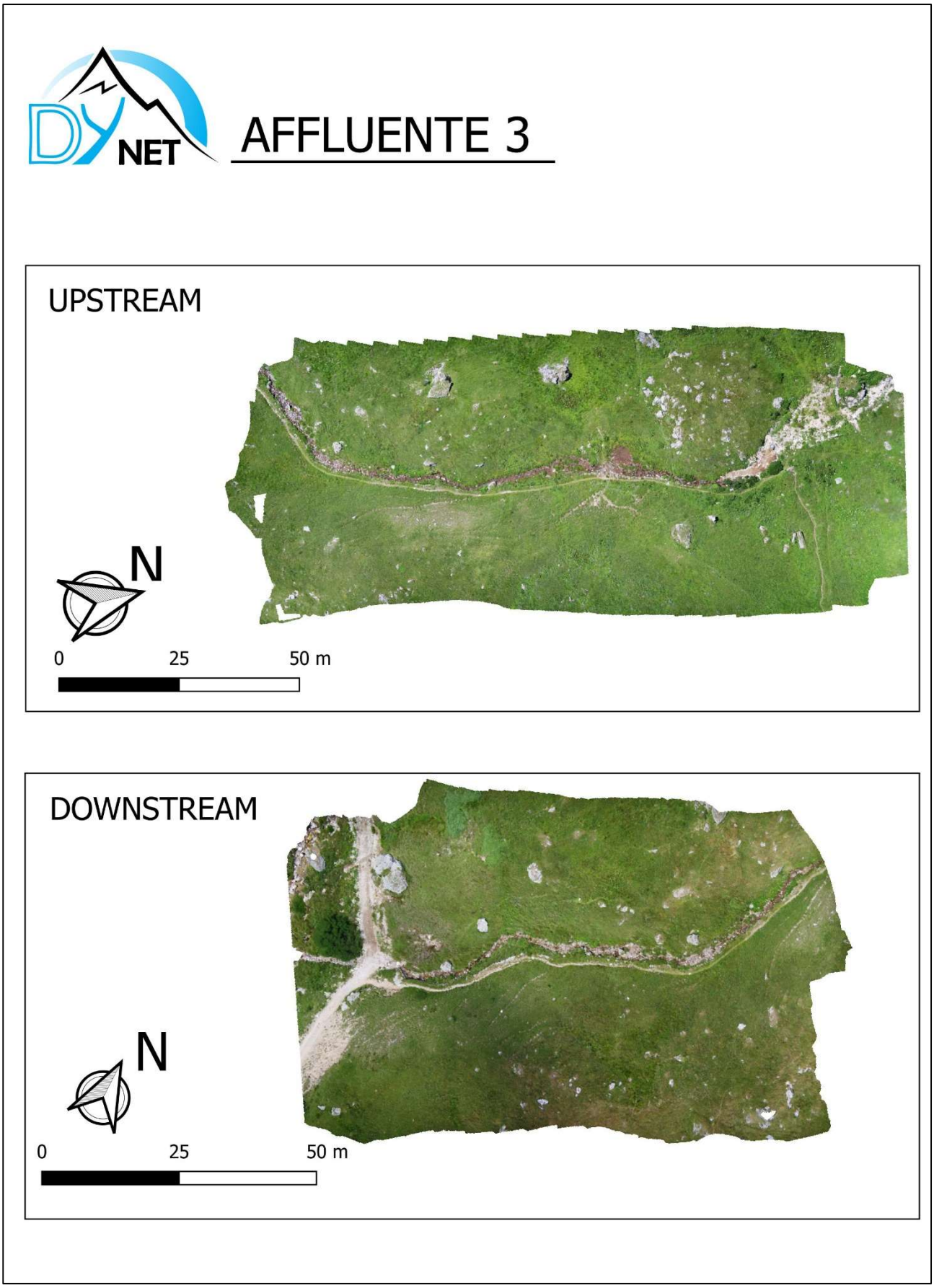

Figure 107: At the top the Orthomosaic of the upstream area of "Affluente 3" with ground resolution 7.18 mm/pixel while at the bottom the Orthomosaic of the valley area with ground resolution 7.73 mm/pixel

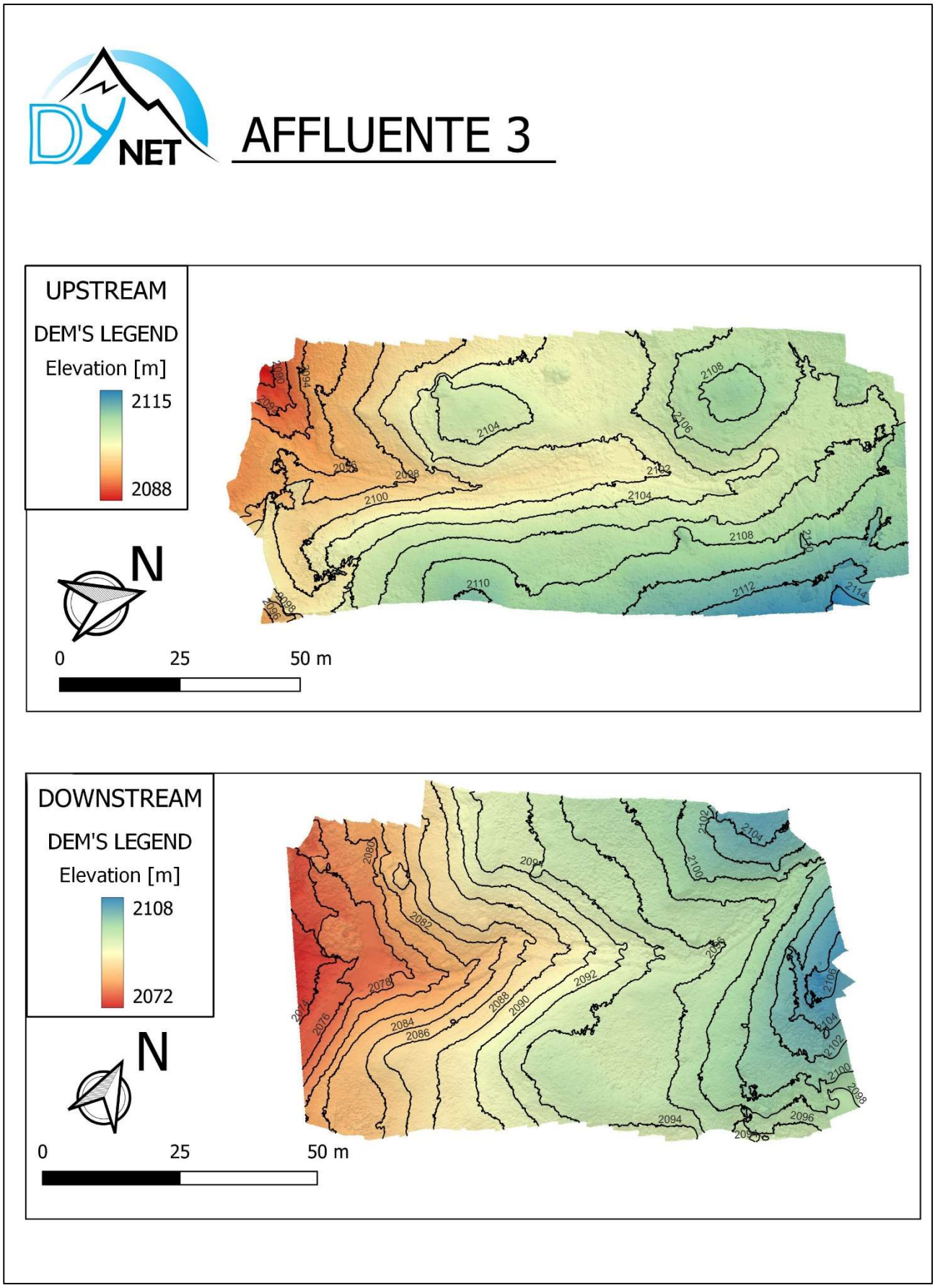

Figure 108: At the top the Contour lines of the upstream area of "Affluente 3", while at the bottom the Contour lines of the valley area both with 2m of step

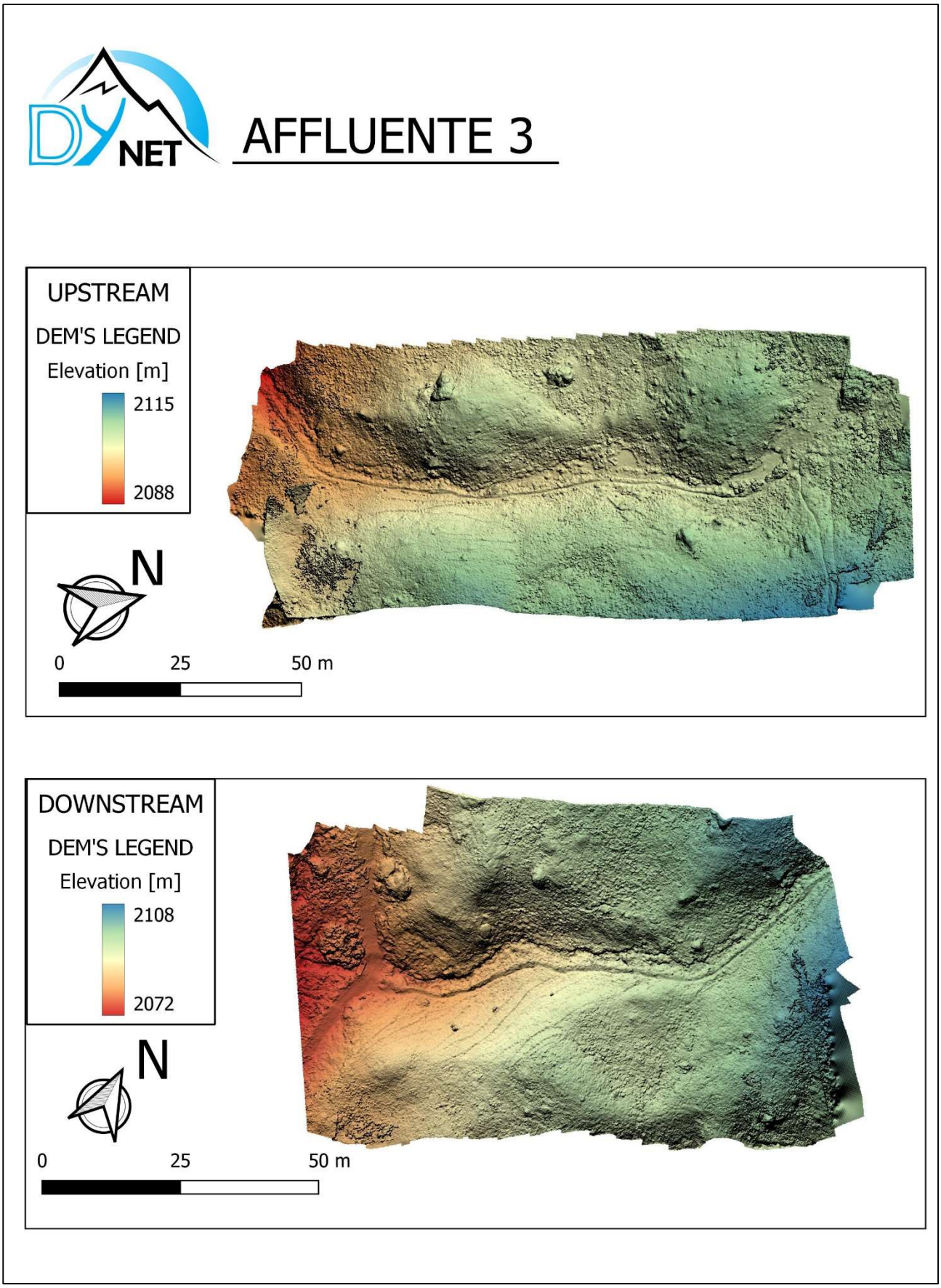

Figure 109: At the top the DEM of the upstream area of "Affluente 3" with resolution 1.44 cm/pixel while at the bottom the DEM of the valley area with resolution 1.55cm/pixel

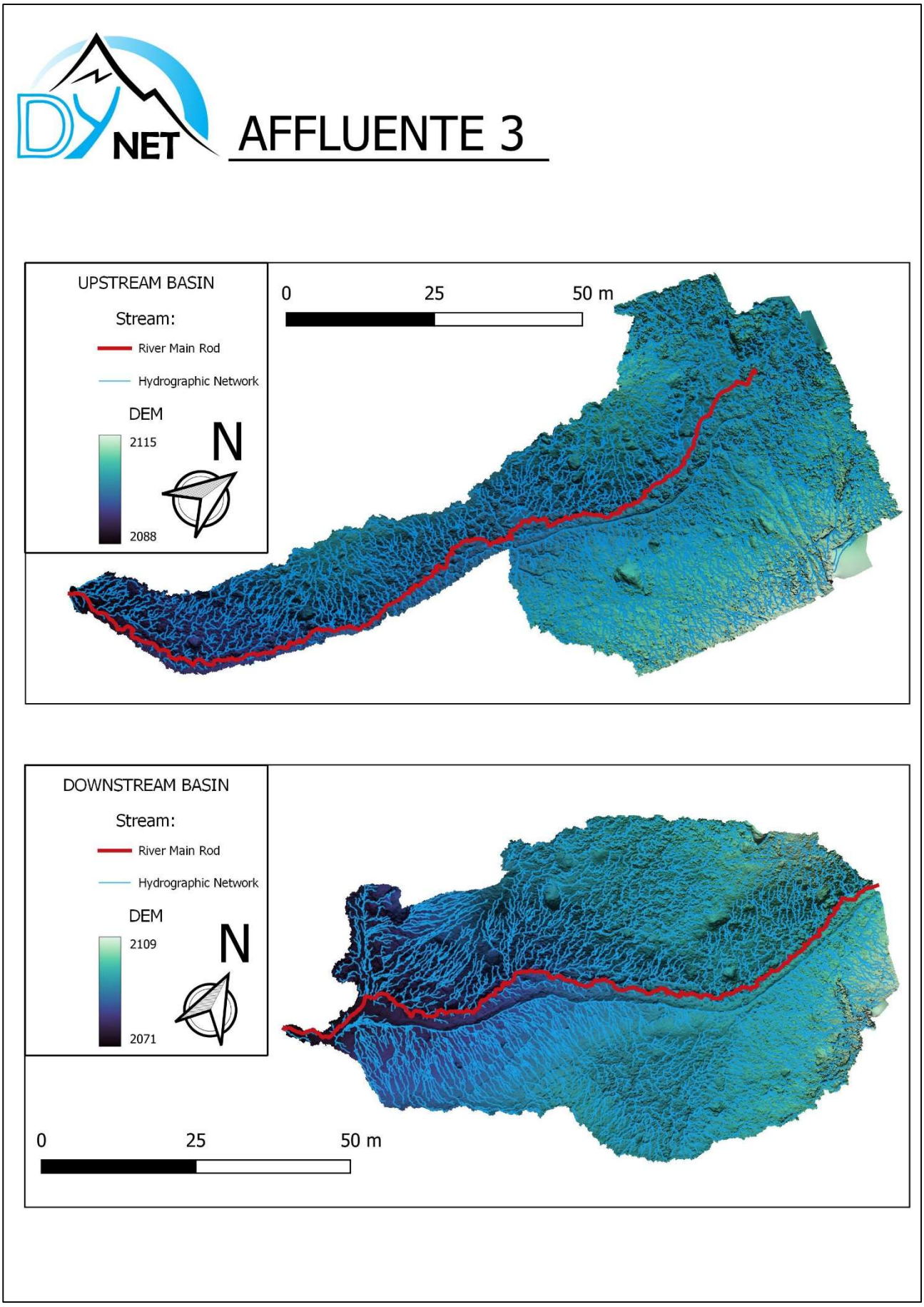

Figure 110: Hydrographic map of "Affluente 3"

Fig. 110 is only a simplification of the basin and drainage network of "Affluente 3", as these data are limited to drone aero-photogrammetric acquisitions and the dense vegetation due to the summer season distorts the ground drainage network. In any case, Fig. 110 provides useful information regarding the location of the main rod, i.e., where the main runoff direction is located, and the areas around it that contribute to runoff.

Tab. 21 and 22 shows the statistics of the surveyed portion of the basin.

Area [m^2]	Perimeter [m]	Min. Altitude [m]	Max. Altitude [m]	Mean Altitude [m]	Altitude's Variance [m^2]	Altitude's Standard Deviation [m]
3'773	507	2'071	2'128	2'092	52	7

Table 21: "Affluente 3 downstream" Basin Statistics

Area [m^2]	Perimeter [m]	Min. Altitude [m]	Max. Altitude [m]	Mean Altitude [m]	Altitude's Variance [m^2]	Altitude's Standard Deviation [m]
3'977	690	2'088	2'115	2'105	20	4

Table 22: "Affluente 3 upstream" Basin Statistics

Finally, thanks to the elevation data of the main rod, the elevation profile was obtained and then modified with a "pit filling" algorithm. Assuming the step can be identified by elevation of drop of 15 cm (or more) within a long distance Δx of 10 cm, the number of jumps was obtained (Fig. 111). I report in Tab. 23 the characteristics of the longitudinal profile of "Affluente 3".

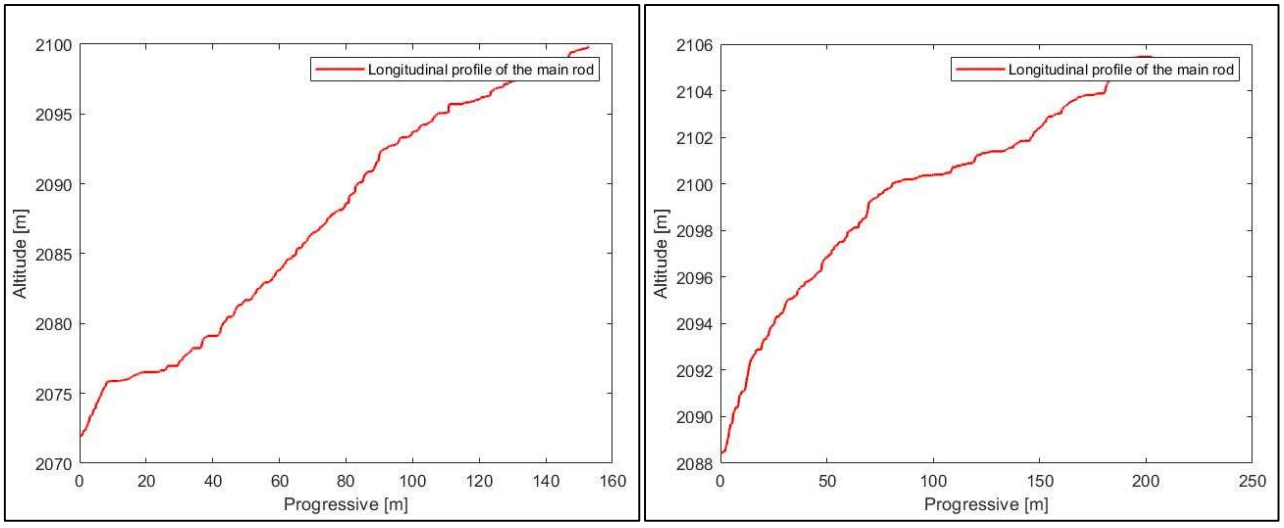

Figure 111: On left side the longitudinal profile of downstream part of "Affluente 3" while on right part the upstream part

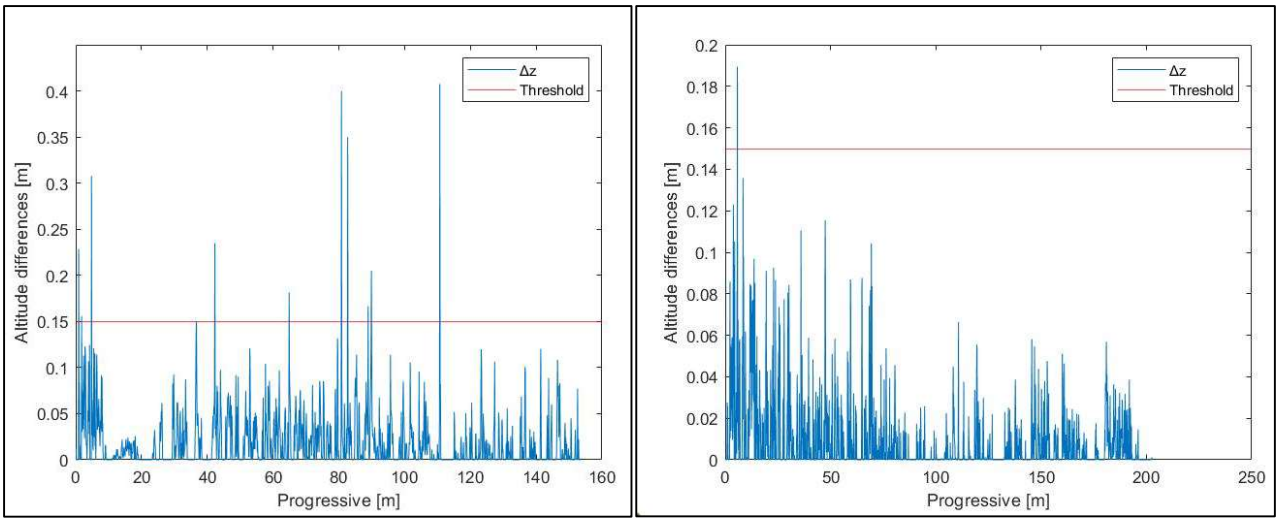

Figure 112: On left side the Step along longitudinal profile of downstream part of "Affluente 3" while on right part the upstream part

The right side of Fig. 112 shows that in the upstream section there are no notable changes in slope for the selected Δx; in fact, as visible from the DEM the upstream part of "Affluente 3" does not show large changes in elevation within the stream bed, except for the area in overlap with the valley part.

Place	Slope	Mean Step Spacing (MSS) [m]	Δx [cm]	Δz [cm]	N°Step
UPSTREAM	0.08	230	10	15	1
DOWSTREAM	0.18	13.63	10	15	11

Table 23:N° of step at "Affluente 3 " for a prescribed Threshold value

The "Affluente 3 upstream" is manly a flat area, the steps along its development are at most in the order of 10 cm and the only relevant jump present is located in the area overlapping with the downstream part where, however, "Affluente 3 upstream" model is affected by DEM distortion. Concerning the "Affluente 3 downstream" model, the presence of the trail tends to divert the tributary's path to a section without steps, where at the end the presence of grass creates a false step.

Figure 113: On the left side the step on the distortion area of "Affluente 3 upstream" while on the rigth side the effect of trail on the downstream part of "Affluente 3"

6.4. Principale Crocefisso

The area named “Principale Crocefisso” is the largest area involved in the project and also the most complex from a morphological point of view being that it crosses several biomes (grassland, rock outcroppings, coniferous forest). Due to its extent it was necessary to split it into two separate files within Metashape, the total survey being based on 221 photos.

The complexity of this survey is not uniquely limited to the amount of photos acquired; a commendable number of markers, reaching up to 58, were essential for proper modeling in order to capture the geometries of the area accurately.

As in “Affluente 3”, given its location within 2 steep slopes, problems arose with RTK signal acquisition solved by performing longer time positioning with the GPS antenna on the markers or by moving the markers a few meters.

Given the amount of photos involved, it was not possible to combine the two models, the results of which will be presented separately, calling, therefore, “Principale Crocefisso Upstream” the area starting from the trail and arriving at the aqueduct intlet, surveyed on 07/08/22 with partially cloudy skies (as notable in the orthophoto in Fig. 130); while “Principale Crocefisso Downstream” will be the area between the trail and the first conifers downstream, the subject of the 07/25/22 campaign under clear sky conditions.

6.4.1. Principale Crocefisso Downstream

The totality of the model consists of 129 photos, divided into 2 chunks separating the survey area in half along the stream flow direction. The chunks will then be combined representing an area of 13'100 m^2.

The sparse cloud (Fig.114) and related survey parameters (Tab.24) are shown below.

Figure 114: Sparse Cloud of "Principale Crocefisso downstream"

Resolution	5280x3956	Tie points	100’610
Flight height [m]	41.9	Projections	333’189
Pixel size [um]	3.28x3.28	Reprojection error	0.594 pixel

Table 24: Sparse Cloud of “Principale Crocefisso downstream" parameters

From the optimization of the alignment, the accuracy of the survey is achieved.

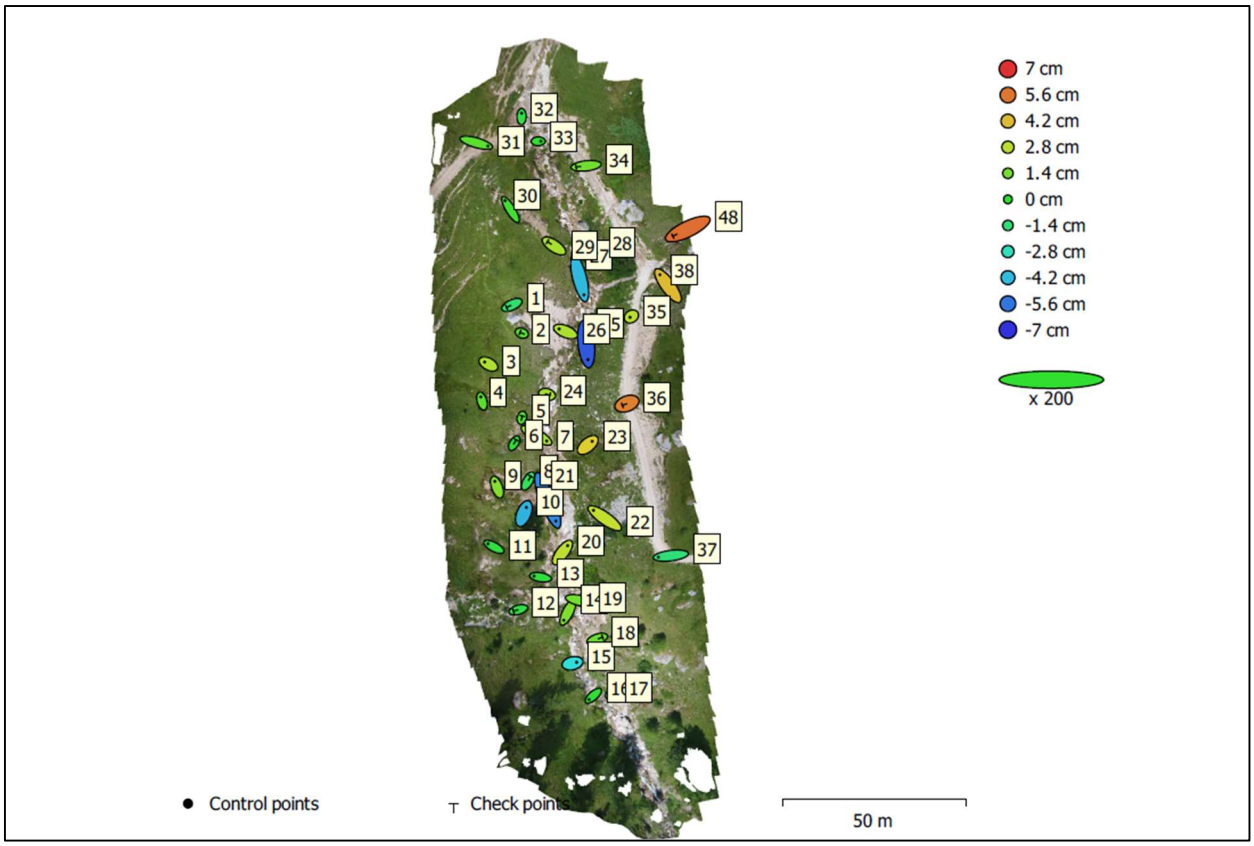

Figure 115: GCP locations and error estimates of "Principale Crocefisso downstream". Z error is represented by ellipse color. X, Y errors are represented by ellipse shape. Estimated GCP locations are marked with a dot or crossing.

Count	X error [cm]	Y error [cm]	Z error [cm]	XY error [cm]	Total [cm]
27	1.79398	2.05273	2.76319	2.72618	3.88166

Table 25: Control points RMSE of "Principale Crocefisso downstream". X - Easting, Y - Northing, Z - Altitude.

Count	X error [cm]	Y error [cm]	Z error [cm]	XY error [cm]	Total [cm]
12	1.74062	0.869956	2.58714	1.94591	3.23726

Table 26: Check points RMSE of "Principale Crocefisso downstream". X - Easting, Y - Northing, Z - Altitude.

Despite the great heterogeneity of the area, thanks to a slower flight and an optimal distribution of markers, it was possible to have a degree of accuracy in the model of less than 5 cm.

This is followed by the restitution of the dense cloud composed of 117'517'291 points, the mesh composed of 1'398'614 vertices and 2'796'629 faces, on which the texture in Fig. 118 was laid.

Figure 116: Dense Cloud of "Principale Crocefisso downstream"

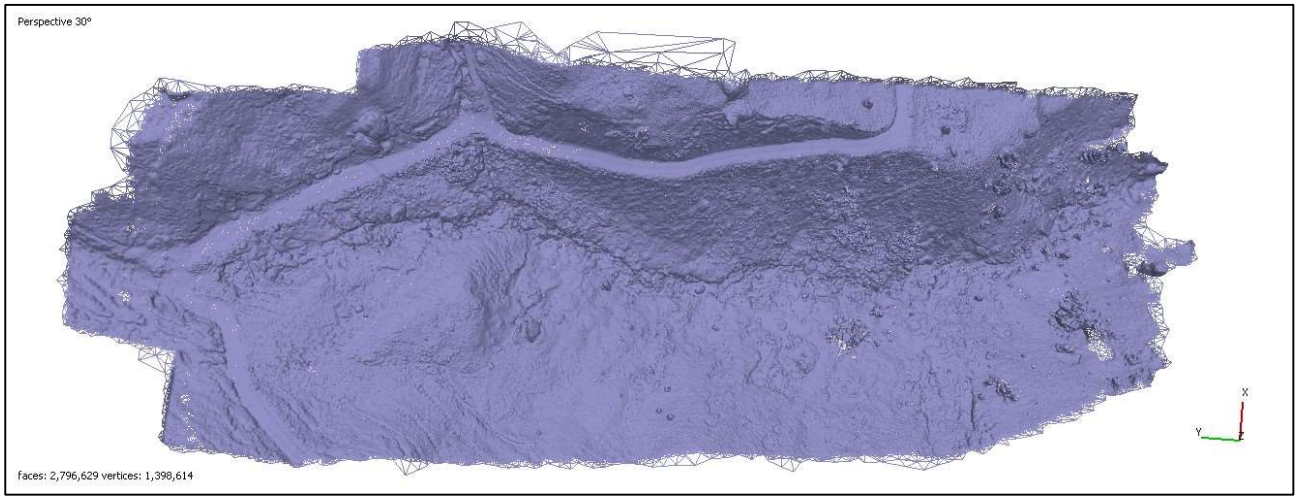

Figure 117: Mesh of "Principale Crocefisso downstream"

Figure 118: Texture of "Principale Crocefisso downstream"

Fig. 119 shows the Orthomosaic representing “Principale Crocefisso downstream” with ground resolution of 8.58 mm/pixel, which provides visual information about the status of the stream on 07/25/22. The Orthomosaic revealed the presence of water, the riverbed and the pattern followed by the watercourse; also clearly visible are the areas around the watercourse.

In Fig. 121, the DEM made with a resolution of 1.72 cm/pixel is shown, from which visual feedback of the distribution of elevations within the survey area can be obtained. It can be seen, thanks also to Fig.121 how the reach “Principale Crocefisso downstream” is located, especially from elevation 2’068 m to 2’028 m within 2 very deep slopes and how the part below 2’060 m is considerably more steep than the part upstream.

On the basis of the cartographic data within the “.tiff file” of the DEM, it was also possible to reconstruct the contour lines of the area shown in Fig. 120 with 2 m step and the hydrographic map in Fig. 122.

Figure 119: Orthomosaic of "Principale Crocefisso downstream" with ground resolution di 8.58 mm/pixel

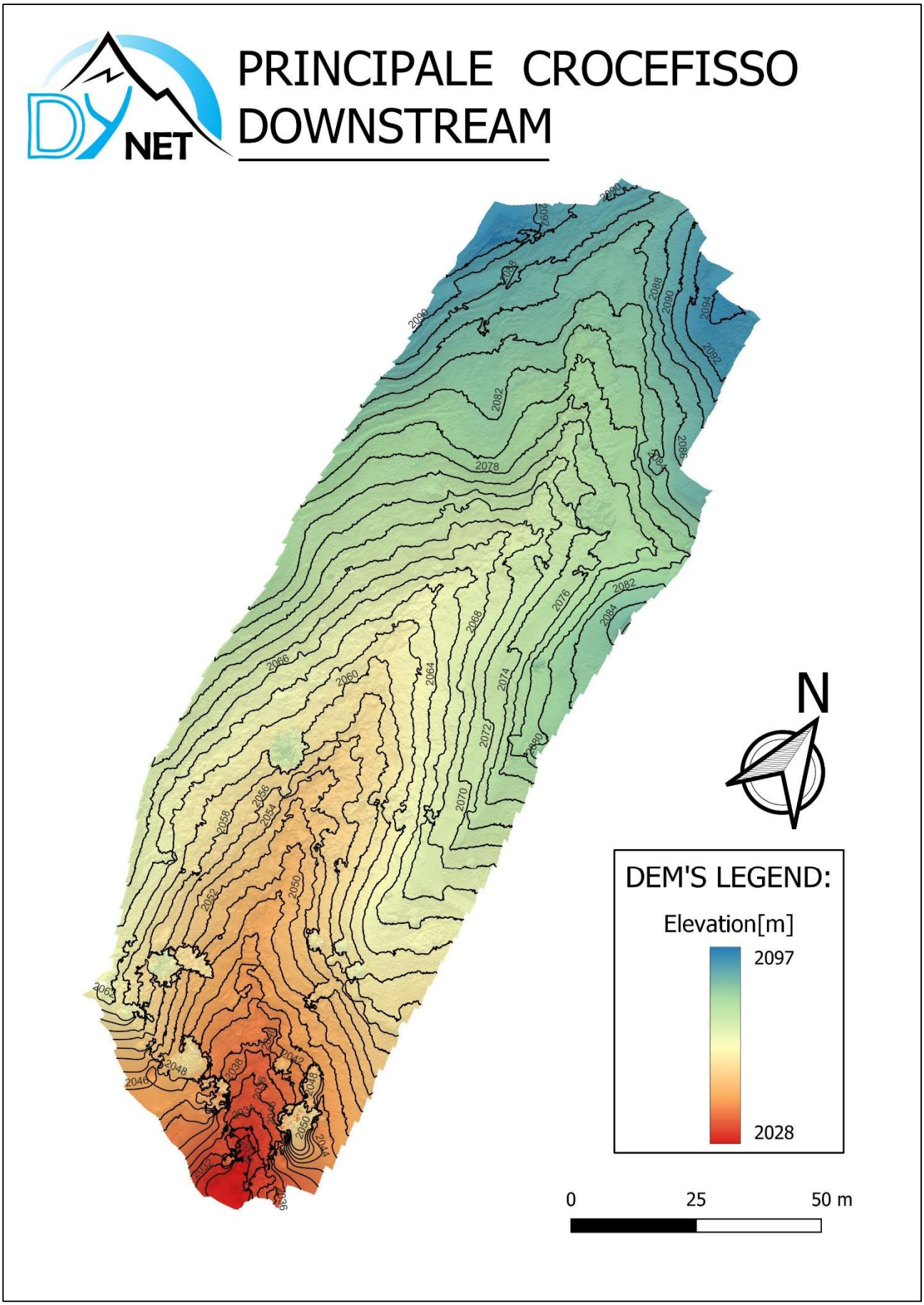

Figure 120: Contour lines of "Principale Crocefisso downstream" with step of 2m

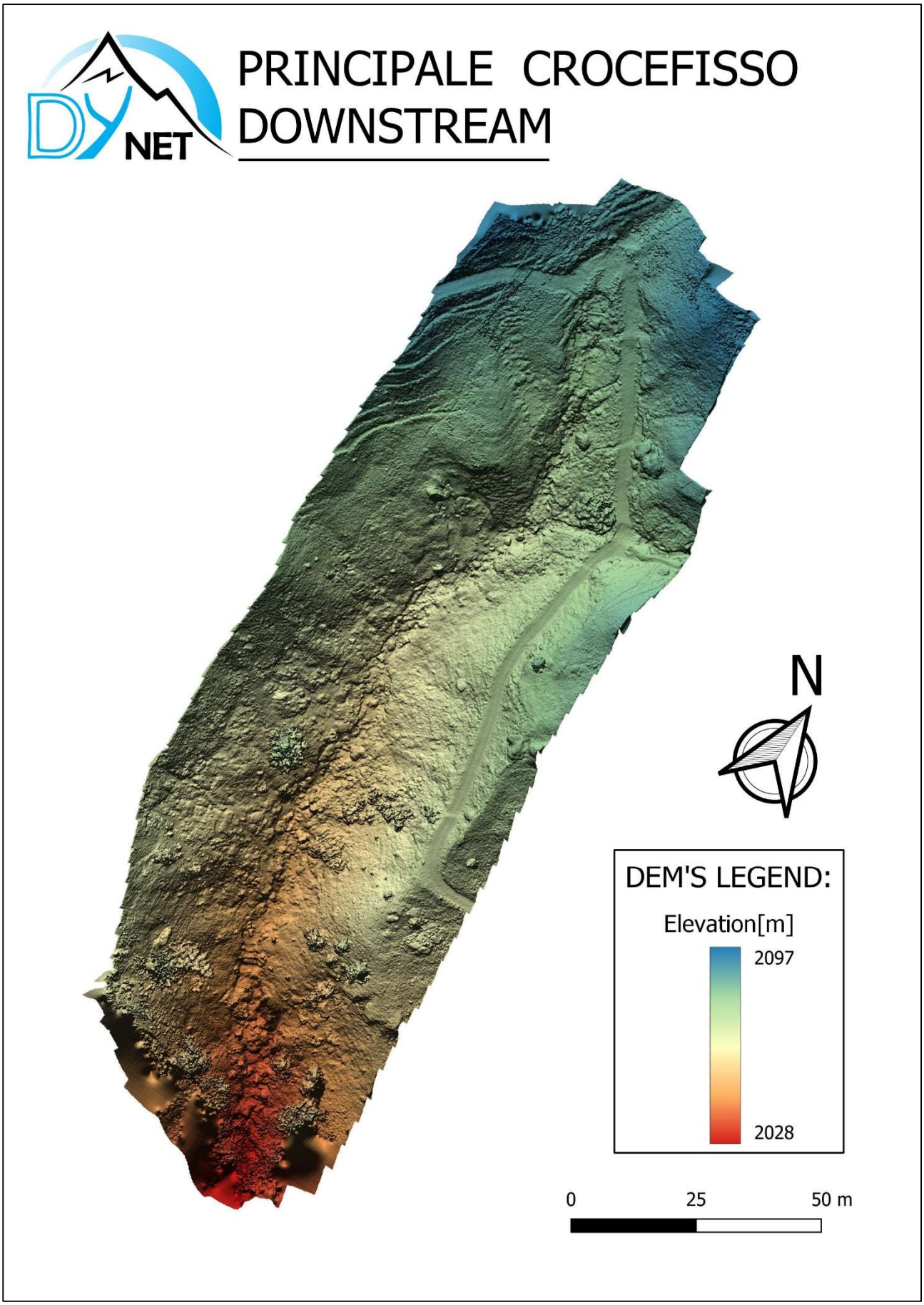

Figure 121: DEM of "Principale Crocefisso downstream" with resolution of 1.72 cm/pixel

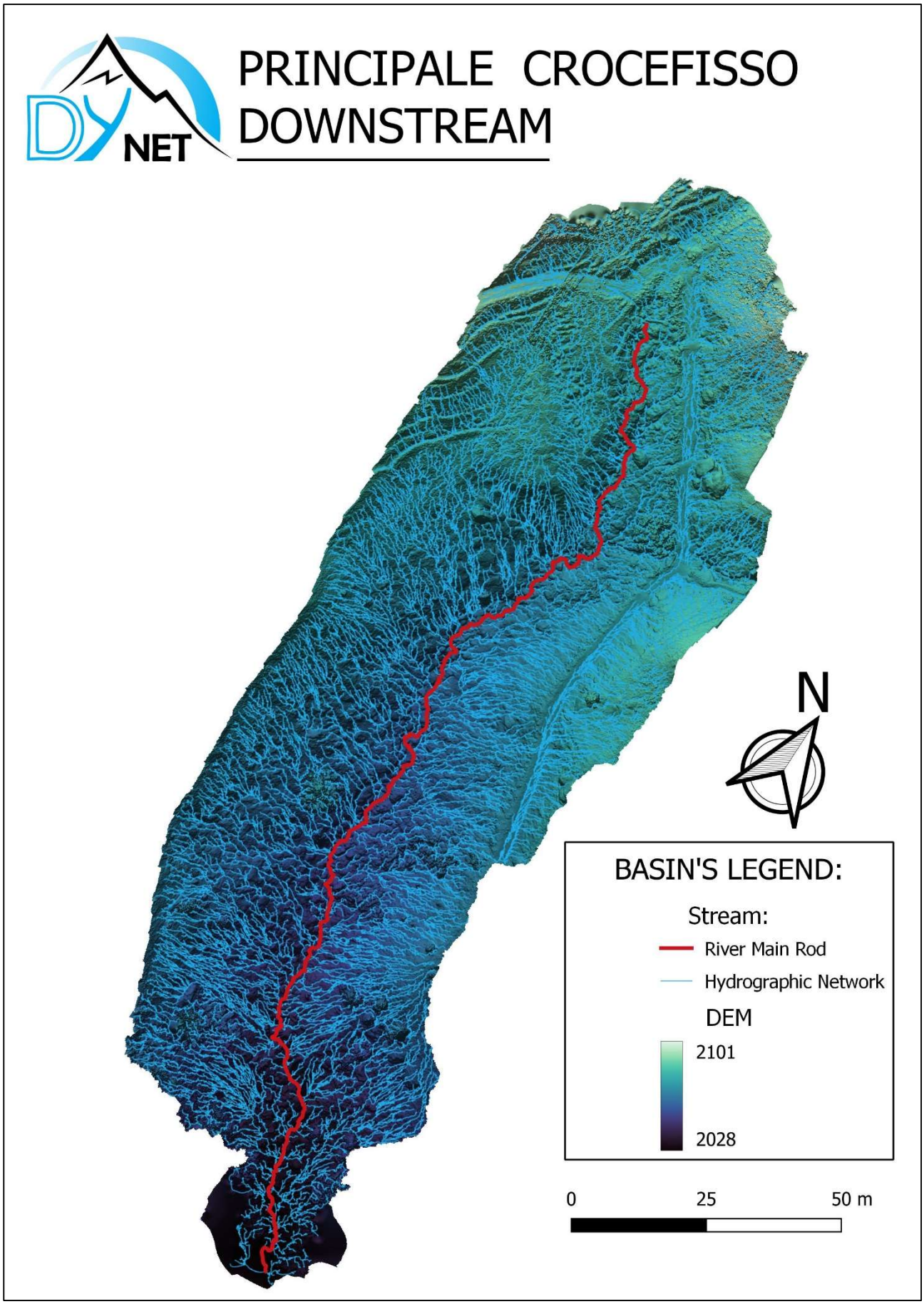

Figure 122: Hydrographic map of "Principale Crocefisso downstream"

Fig. 122 is only a simplification of the basin and drainage network of "Principale Crocefisso downstream", as these data are limited to drone aerophotogrammetric acquisitions. In any case, Fig. 122 provides useful information regarding the location of the main rod, i.e., where the main runoff direction is located, and the areas around it that contribute to the runoff.

Tab. 27 shows the statistics of the surveyed portion of the basin.

Area [m^2]	Perimeter [m]	Min. Altitude [m]	Max. Altitude [m]	Mean Altitude [m]	Altitude's Variance [m^2]	Altitude's Standard Deviation [m]
11'824	876	2'027	2'101	2'068	211	14

Table 27: "Principale Crocefisso downstream" Basin Statistics

Finally, thanks to the elevation data of the main rod, the elevation profile was obtained and then modified with a "pit filling" algorithm. Assuming the step can be identified by elevation of drop of 15 cm (or more) within a long distance Δx of 20 cm, the number of jumps was obtained (Fig. 123). I report in Tab. 28 the characteristics of the longitudinal profile of "Principale Crocefisso downstream".

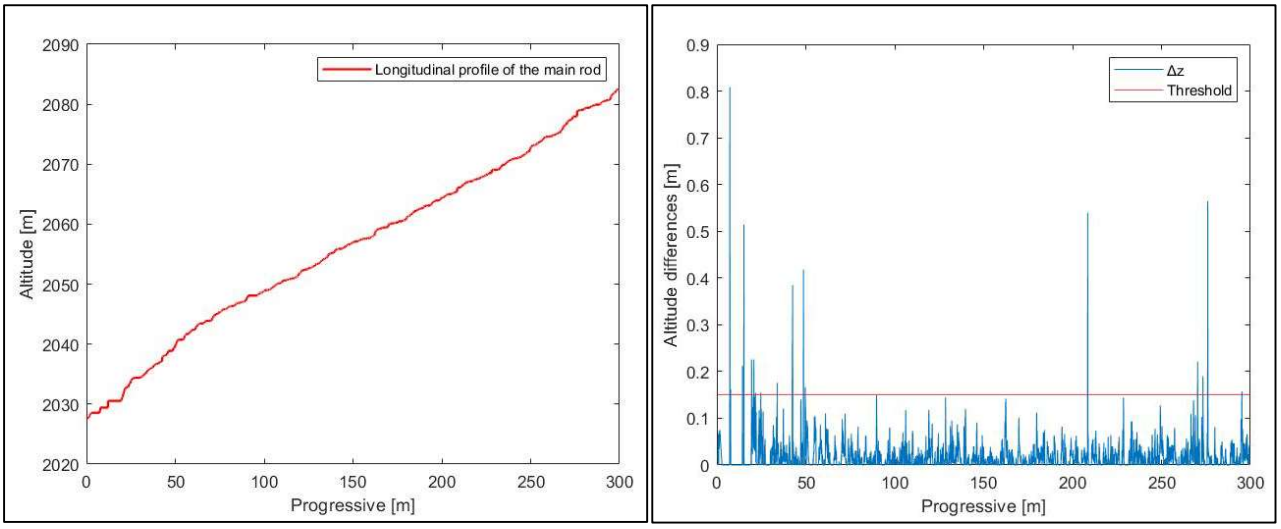

Figure 123:On the left side the longitudinal profile of the section of " Principale Crocefisso downstream " on the right side the steps along the longitudinal profile

Slope	Mean Step Spacing (MSS) [m]	Δx [cm]	Δz [cm]	N°Step
0.18	5.66	20	15	53

Table 28:N° of step at " Principale Crocefisso downstream " for a prescribed Threshold value

The "Principale Crocefisso downstream" model is also affected by DEM distortion, as in "Affluent 3 upstream", resulting in 20 steps being detected instead of the 8 maximum steps actually present in the valley part. The other steps are captured with good accuracy.

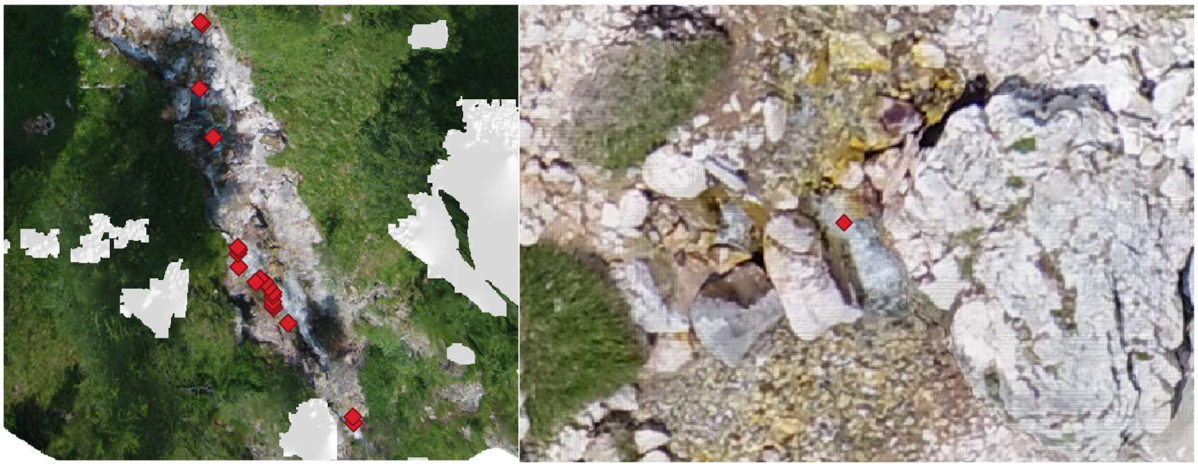

Figure 124: On the left the Problem due to the distorsion of the DEM of "Principale Crocefisso downstream", while on left an example of step-pool found by the algorithm

6.4.2. Principale Crocefisso Upstream

The model consists of 92 photos processed within a single chunk that covers an area of 11'700 m^2.

The sparse cloud (Fig. 125) and related survey parameters (Tab. 29) are shown below.

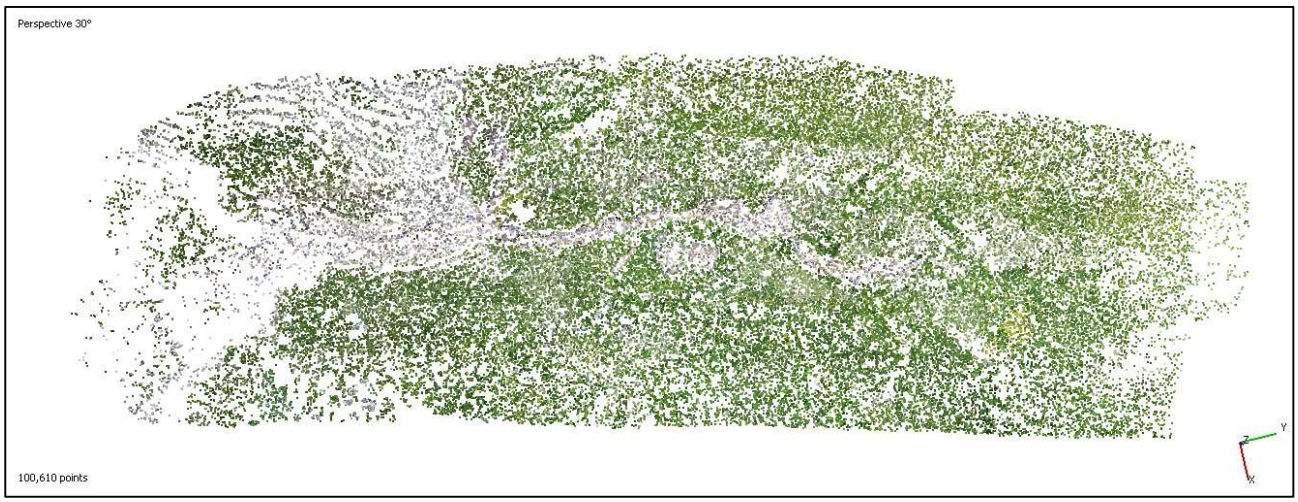

Figure 125: Sparse Cloud of "Principale Crocefisso upstream

Resolution	5280x3956	Tie points	100'610
Flight height [m]	41.9	Projections	330'189
Pixel size [um]	3.28x3.28	Reprojection error	0.594 pixel

Table 29: Sparse Cloud of "Principale Crocefisso downstream" parameters

From the optimization of the alignment, the accuracy of the survey is obtained:

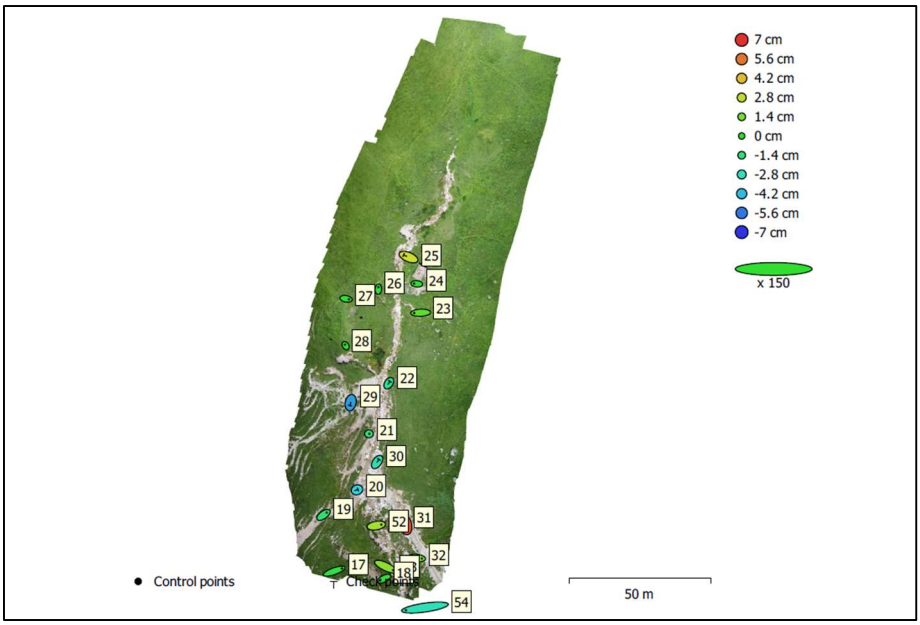

Figure 126: GCP locations and error estimates of "Principale Crocefisso upstream". Z error is represented by ellipse color. X, Y errors are represented by ellipse shape. Estimated GCP locations are marked with a dot or crossing.

Count	X error [cm]	Y error [cm]	Z error [cm]	XY error [cm]	Total [cm]
13	3.22365	0.842134	1.32785	3.33183	3.58668

Table 30: Control points RMSE of "Principale Crocefisso upstream". X - Easting, Y - Northing, Z - Altitude.

Count	X error [cm]	Y error [cm]	Z error [cm]	XY error [cm]	Total [cm]
6	1.07925	1.18356	4.07101	1.60175	4.37478

Table 31: Check points RMSE of "Principale Crocefisso upstream". X - Easting, Y - Northing, Z - Altitude.

This is followed by the rendering of the dense cloud composed of 66'193'546 points, the mesh composed of 208'492 vertices and 416'469 faces, on which the texture in Fig. 129 was laid.

Figure 127: Dense Cloud of "Principale Crocefisso upstream"

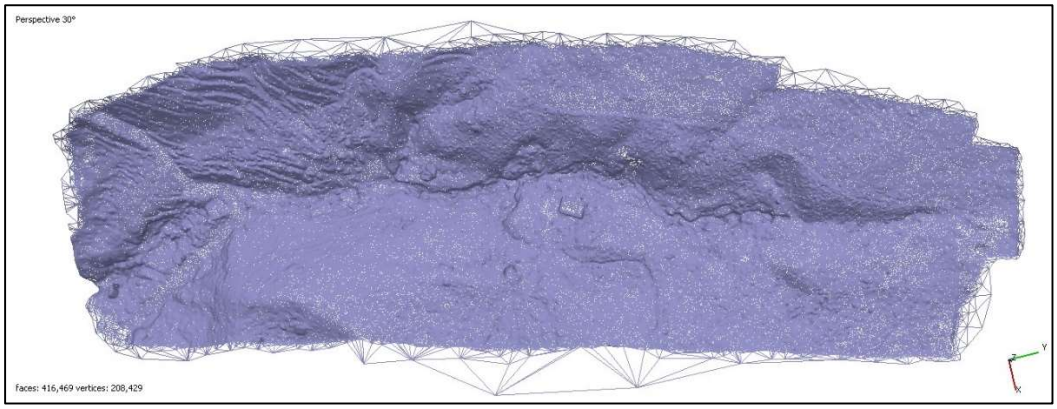

Figure 128: Mesh of "Principale Crocefisso upstream"

Figure 129: texture of "Principale Crocefisso upstream"

Fig. 130 shows the Orthomosaic representing “Principale Crocefisso upstream” with ground resolution of 8.47 mm/pixel, which provides visual information about the status of the stream on 07/08/22. The Orthomosaic revealed the presence of water, the riverbed and the pattern followed by the watercourse; also clearly visible are the areas around the watercourse described above.

In Fig. 132, the DEM made with a resolution of 1.69 cm/pixel is presented, from which visual feedback of the distribution of elevations within the survey area can be obtained. Fig.132 shows how there is a gradual change in elevation, without abrupt changes along the longitudinal profile, just as in “Meteo Valle”. Moreover, it is evident how the valley part of this area is developed within steep slopes, in fact in Fig. 131 the contour lines of the slopes are very close.

On the basis of the cartographic data within the “.tiff” file of the DEM, it was also possible to reconstruct the contour lines of the area shown in Fig. 131 with 2 m step and the hydrographic map in Fig. 133.

Figure 130: Orthomosaic of "Principale Crocefisso upstream" with ground resolution di 8.47 mm/pixel

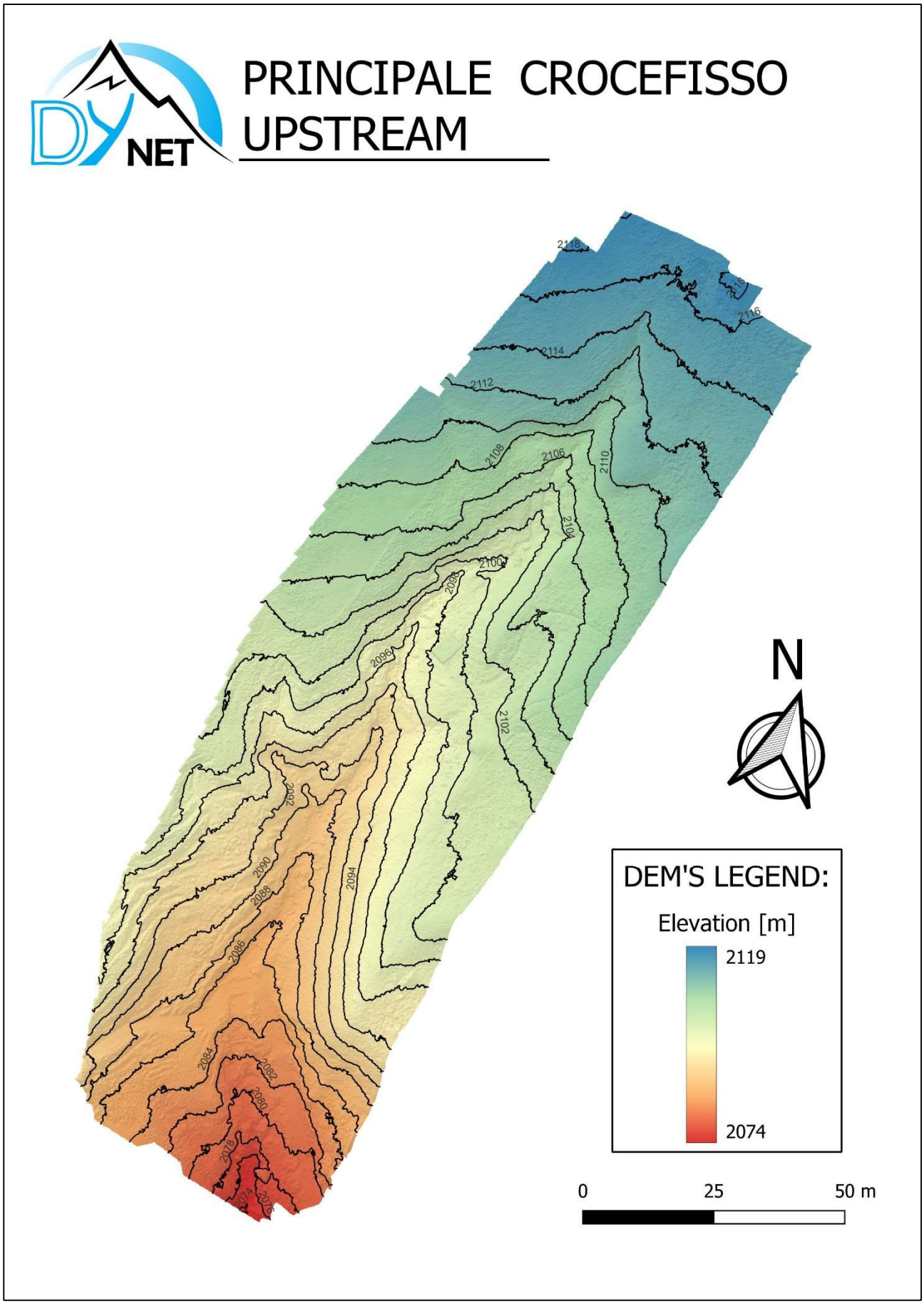

Figure 131: Contour lines of "Principale Crocefisso upstream" with step of 2m

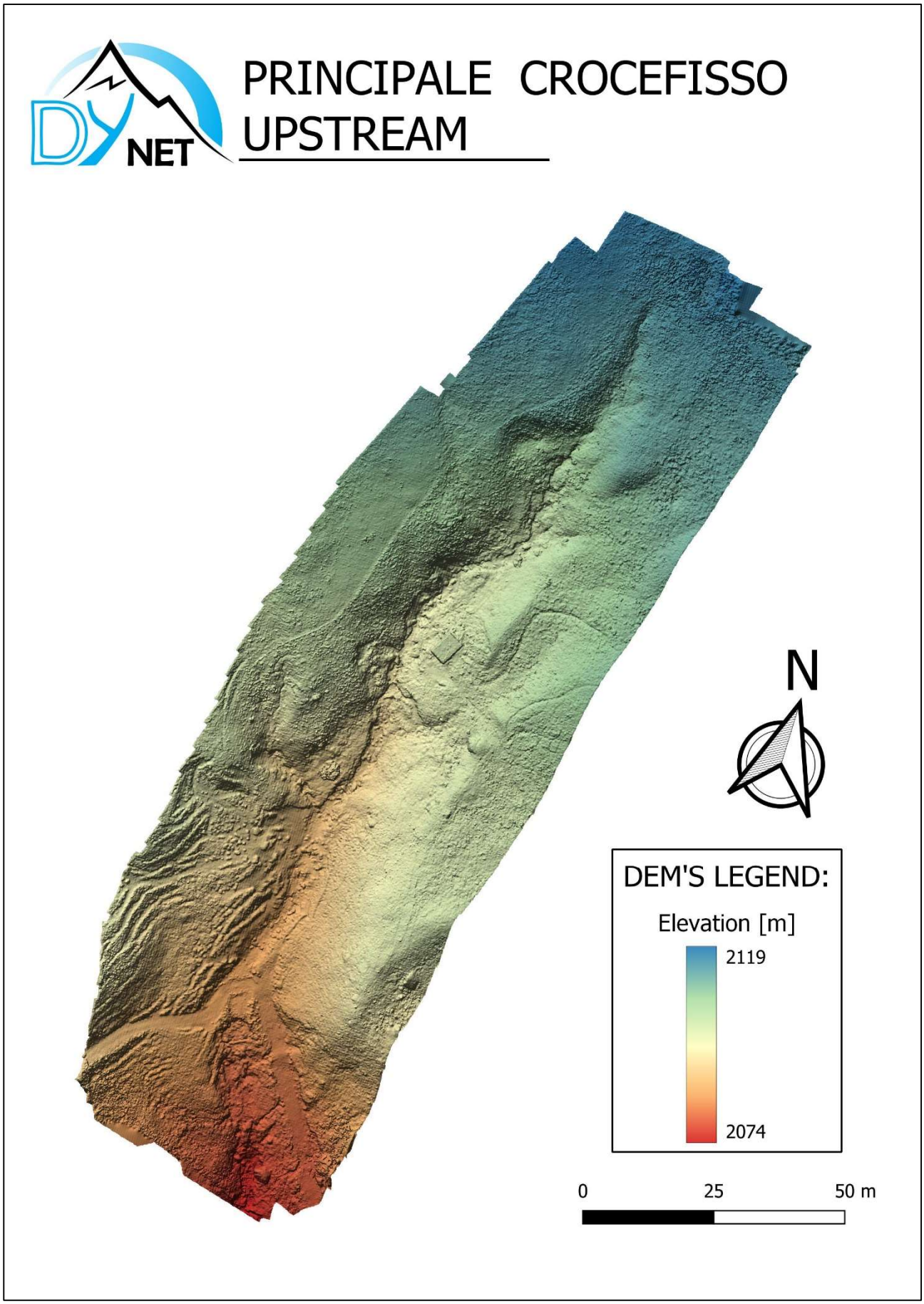

Figure 132: DEM of "Principale Crocefisso upstream" with resolution of 1.69 cm/pixel

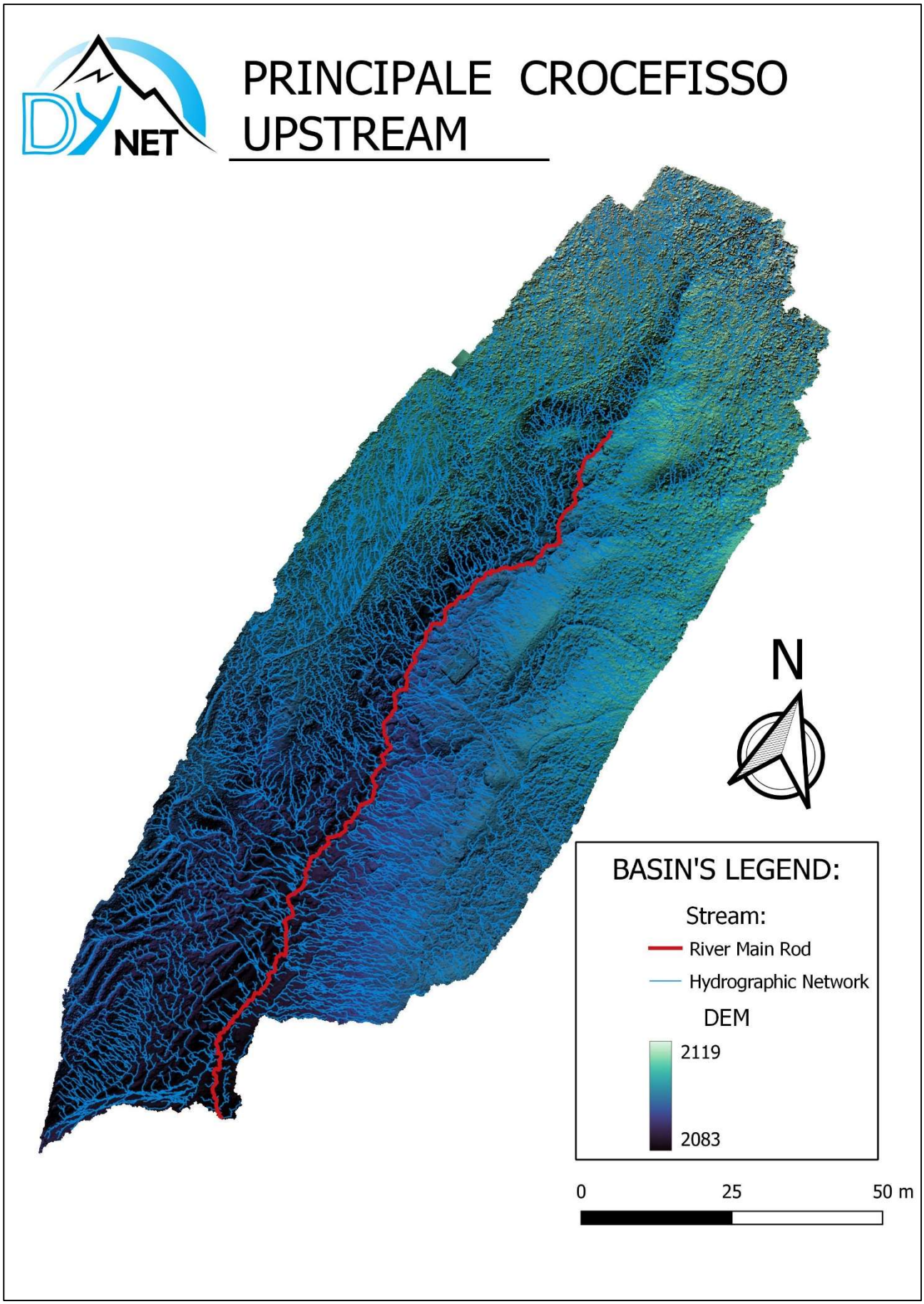

Figure 133: Hydrographic map of "Principale Crocefisso upstream"

Fig. 133 is only a simplification of the basin and drainage network of "Principale Crocefisso upstream", as these data are limited to drone aero-photogrammetric acquisitions and the dense vegetation due to the summer season distorts the ground drainage network. In any case, Fig. 133 provides useful information regarding the location of the main stem, i.e., where the main runoff direction is located, and the areas around it that contribute to runoff.

Tab. 32 shows the statistics of the surveyed portion of the basin.

Area [m^2]	Perimeter [m]	Min. Altitude [m]	Max. Altitude [m]	Mean Altitude [m]	Altitude's Variance [m^2]	Altitude's Standard Deviation [m]
9'428	817	2'083	2'120	2'102	71	8

Table 32: "Principale Crocefisso upstream" Basin Statistics

Finally, thanks to the elevation data of the main rod, the elevation profile was obtained and then modified with a "pit filling" algorithm. Assuming the step can be identified by elevation of drop of 15 cm (or more) within a long distance Δx of 20 cm, the number of jumps was obtained (Fig. 134). I report in Tab. 33 the characteristics of the longitudinal profile of "Principale Crocefisso upstream".

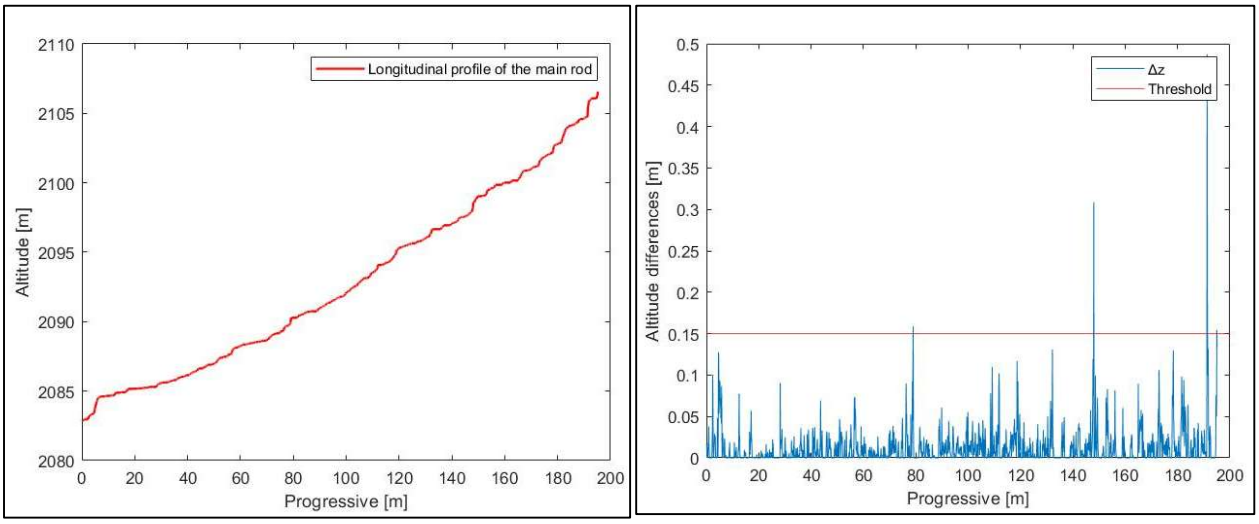

Figure 134: On the left side the longitudinal profile of the section of " Principale Crocefisso upstream " on the right side the steps along the longitudinal profile

Slope	Mean Step Spacing (MSS) [m]	Δx [cm]	Δz [cm]	N°Step
0.13	8.86	20	15	22

Table 33: N° of step at "Principale Crocefisso upstream" for a prescribed Threshold value

In "Principale Crocefisso upstream" the steps, as shows in Fig.134, are often less than 10 cm and the comparison with the DEM and texture navigation also confirm this. The number of steps turns out to be high because in the upstream part of this zone, where the slope is higher, there are 3 steps that are divided by the algorithm into several steps causing 7 fakes. While downstream only 2 steps present double points.

Figure 135: On the left side an example of extra point on downstream part of "Principale Crocefisso upstream" while on right side an example on upstream part

6.5. Principale Ponte

The area of “Principale Ponte” has undergone similar processing as “Principale Crocefisso” in terms of photogrammetric processing, the survey was done in 2 separate non-joining projects called “Downstream Ponte” and “Upstream Ponte”. The motivation for this choice was related to the presence of some conifers positioned orthogonally to the watercourse that do not allow a single flight with the drone over the entire area.

Figure 136: Climatic conditions during the survey at “Principale Ponte”

The area from the morphological point of view is very complex, in fact the upstream part is located between two very steep slopes where the slope located to the east is entirely covered with conifers, while the opposite slope is full of herbaceous vegetation with considerable height. These peculiarities have made surveying in this area more difficult than in any others. The incised nature of the site made GPS signal acquisition impossible in certain parts; this issue greatly constrained the choice on marker placement, which was always constrained to areas where there was signal. Additional limitations for QCPs and GCPs were trees that prevented the drone camera from seeing the ground and tall grass that impeded their placement on the ground.

The dense vegetation in the area, however, did not only make data acquisition difficult, but also its processing. In fact, with the working procedure used in this thesis, where there is no point cloud classification, the maximum elevation data returned by the DEM is distorted by the presence of trees. This is particularly evident when comparing DEMs and contour maps where the elevation difference is on the order of 5/10 m. Because of this, it was decided not to determine the basin statistics but to extract only the main rod.

In addition to natural elements, in the downstream portion, anthropogenic elements also posed an obstacle. In fact, here the Valfredda is crossed by 2 wooden bridges, making it necessary to split the processing in QGIS in order to determine the main rod and its properties. The section upstream from the first of bridges will be processed initially, then the section between the 2 bridges, and finally the final section (always following the processing given in Chap. 5).

It should be pointed out that throughout the survey carried out on 08/26/22 the weather conditions were not optimal. In fact, there were rain and sparse clouds. Despite the bad wheatear conditions, models with an accuracy in the order of 5 cm were obtained.

6.5.1. Ponte Downstream

The totality of the model consists of 111 photos, processed into 2 chunks by separating the area along the main stream drainage direction. The chunks will then be merged to represent an area of 10'400 m^2.

The sparse cloud (Fig. 137) and related survey parameters (Tab. 34) are shown below.

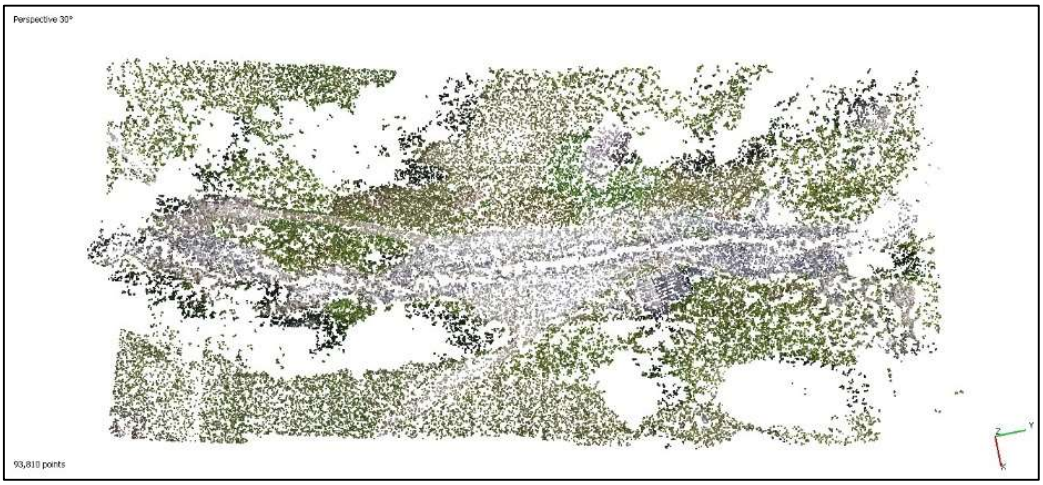

Figure 137: Sparse Cloud of "Ponte downstream"

Resolution	5280x3956	Tie points	93'810
Flight height [m]	46.7	Projections	378'061
Pixel size [um]	3.28x3.28	Reprojection error	0.591 pixel

Table 34: Sparse Cloud of "Ponte downstream" parameters

From the optimization of the alignment, the accuracy of the survey is achieved:

Figure 138: GCP locations and error estimates of "Ponte downstream".
Z error is represented by ellipse color. X,Y errors are represented by ellipse shape.

Estimated GCP locations are marked with a dot or crossing.

Count	X error [cm]	Y error [cm]	Z error [cm]	XY error [cm]	Total [cm]
13	2.94836	2.07692	1.59104	3.60644	3.9418

Table 35: Control points RMSE of "Ponte downstream".
X - Easting, Y - Northing, Z - Altitude.

Count	X error [cm]	Y error [cm]	Z error [cm]	XY error [cm]	Total [cm]
5	2.26022	1.12225	4.06956	2.5235	4.78846

Table 36: Check points RMSE of "Ponte downstream".
X - Easting, Y - Northing, Z - Altitude.

Despite the adverse weather conditions, and natural limitations in marker placement, it was possible to obtain a model with an error of less than 5 cm.

This is followed by the restitution of the dense cloud composed of 118'985'537 points, the mesh composed of 1'104'693 vertices and 2'208'194 faces, on which the texture in Fig. 141 was laid.

Figure 139: Dense Cloud of "Ponte downstream"

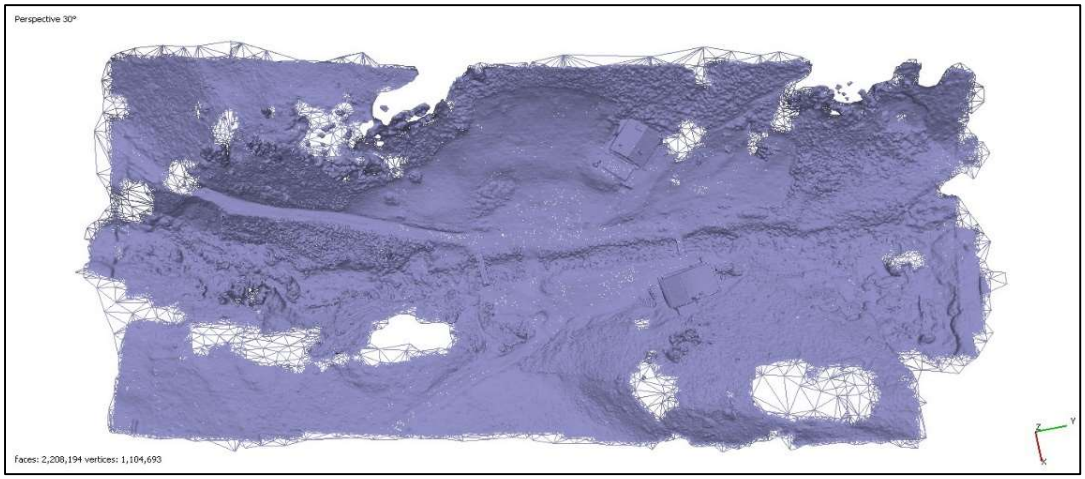

Figure 140: Mesh of "Ponte downstream"

Figure 141: Texture of "Ponte downstream"

Fig. 142 shows the Orthomosaic representing “Ponte downstream” with ground resolution of 7.08 mm/pixel, which provides information about the state of the stream on 08/26/22. The Ortomosaic revealed the presence of water, the riverbed, and the pattern followed by the stream; also clearly visible are the areas around the stream and the 2 bridges that break the longitudinal profile.

In Fig. 144 the DEM made with a resolution of 1.42 cm/pixel is present, from which visual feedback of the distribution of elevations within the survey area can be obtained. Fig.143 indicates how the stream bed has elevation values that are mainly found in the lower part of the DEM legend. This reveals a gradual trend in the height distributions with a tendency to become more inclined in the downstream section after the bridge at 1’932 m. Fig. 143 shows how the upstream part of this area develops within steep slopes, in fact the contour lines of the slopes are very close together.

On the basis of the cartographic data within the “.tiff” file of the DEM, it was also possible to reconstruct the contour lines of the area shown in Fig. 143 with 2 m pitch and the hydrographic map in Fig. 145.

Figure 142: Orthomosaic of "Ponte downstream" with ground resolution di 7.08 mm/pixel

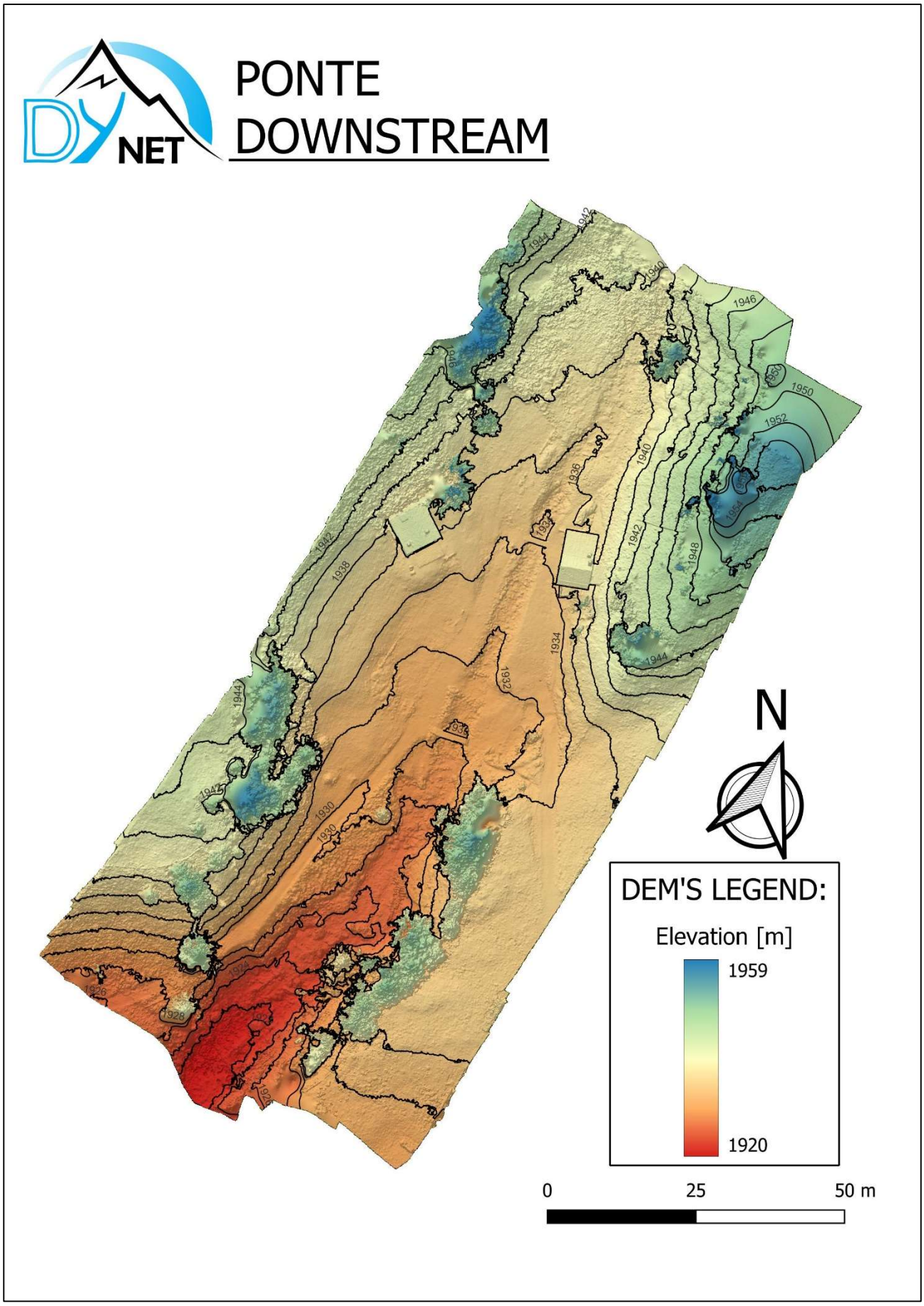

Figure 143: Contour lines of "Ponte downstream" with step of 2m

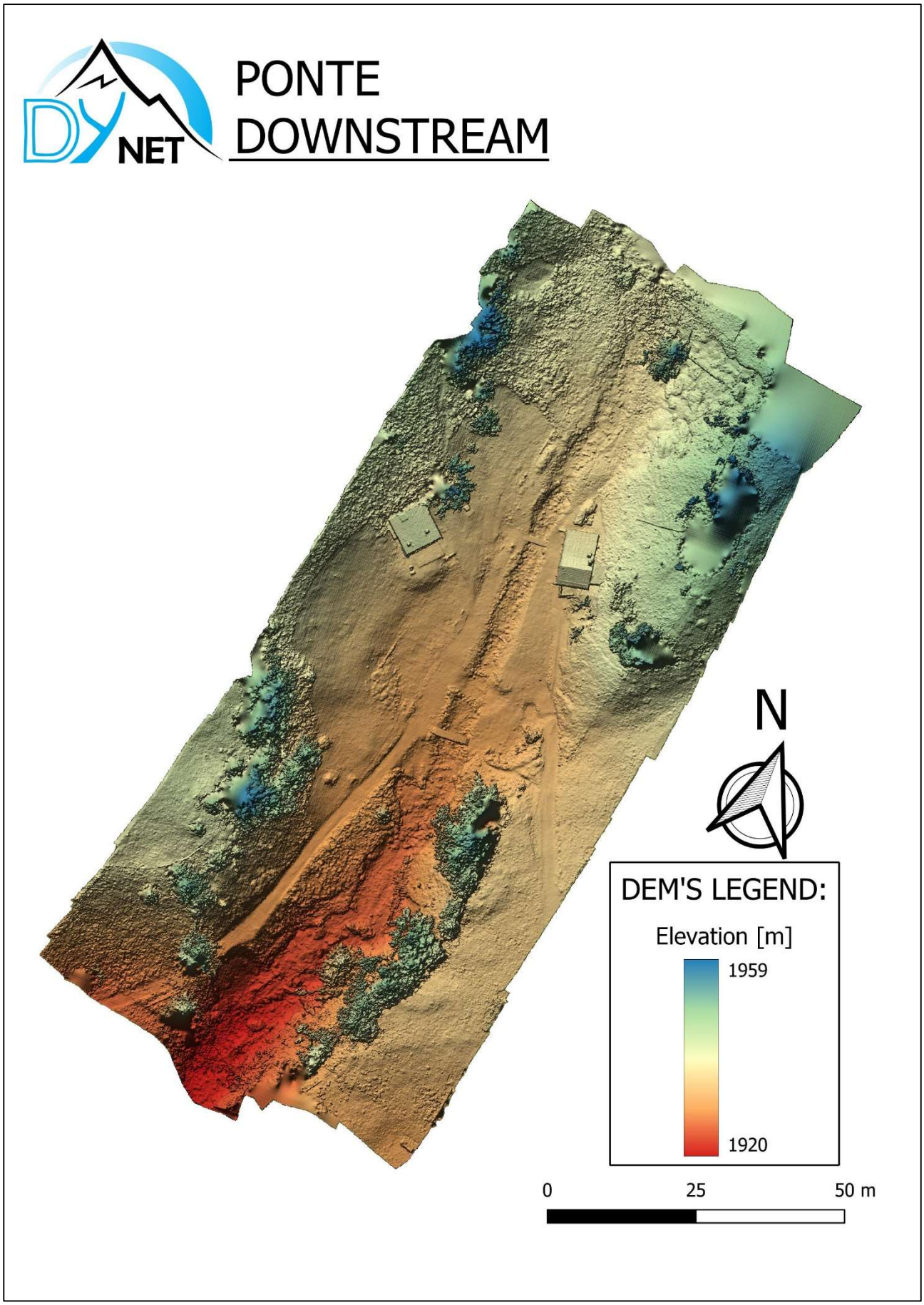

Figure 144: DEM of "Ponte downstream" with resolution of 1.42 cm/pixel

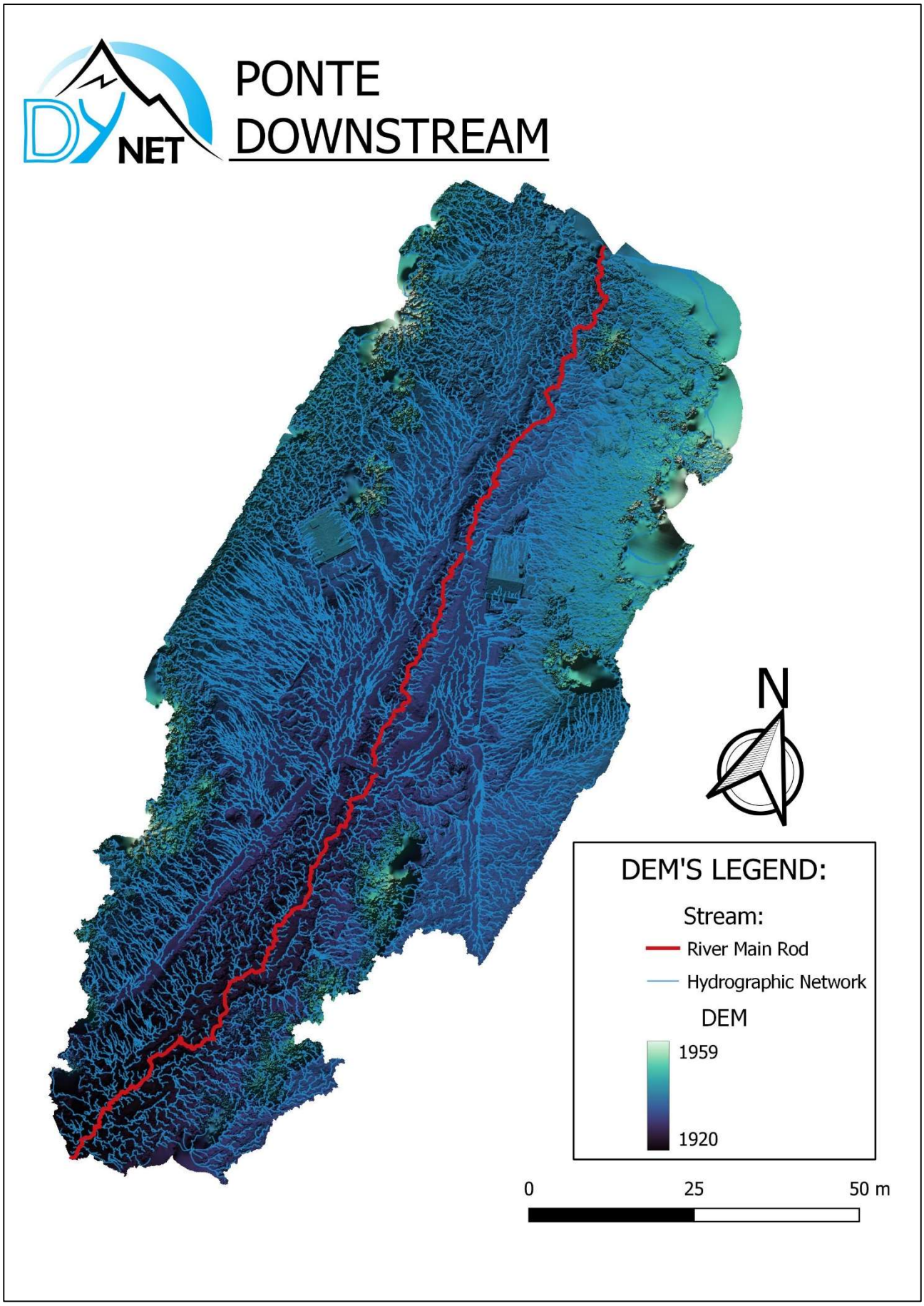

Figure 145: Hydrographic map of "Ponte downstream"

Fig. 145 is only a simplification of the basin and drainage network of "Ponte Downstream", as these data are limited to drone aero-photogrammetric acquisitions and the dense vegetation due to the summer season in combination with the numerous conifers distort the ground drainage network. In any case Fig. 145 provides useful information regarding the location of the main stem, i.e., where the main runoff direction is located, and the areas around it that contribute to the runoff. Fig. 145, also, shows the breakdown of the rod into 3 parts; this is to avoid errors due to the presence of the bridges in the restitution of the longitudinal profile. For better visualization the graphs of the three sections are shown separately.

Perimeter and area of the basin are reported in Tab.37.

Area [m^2]	Perimeter [m]
8'271	823

Table 37: "Ponte downstream" Basin Statistics

Finally, thanks to the elevation data of the main rod, the elevation profile was obtained and then modified with a "pit filling" algorithm. Assuming the step can be identified by elevation of drop of 15 cm (or more) within a long distance Δx of 20 cm, the number of jumps was obtained (Fig. 146-148). I report in Tab. 38 the characteristics of the longitudinal profile of "Ponte downstream".

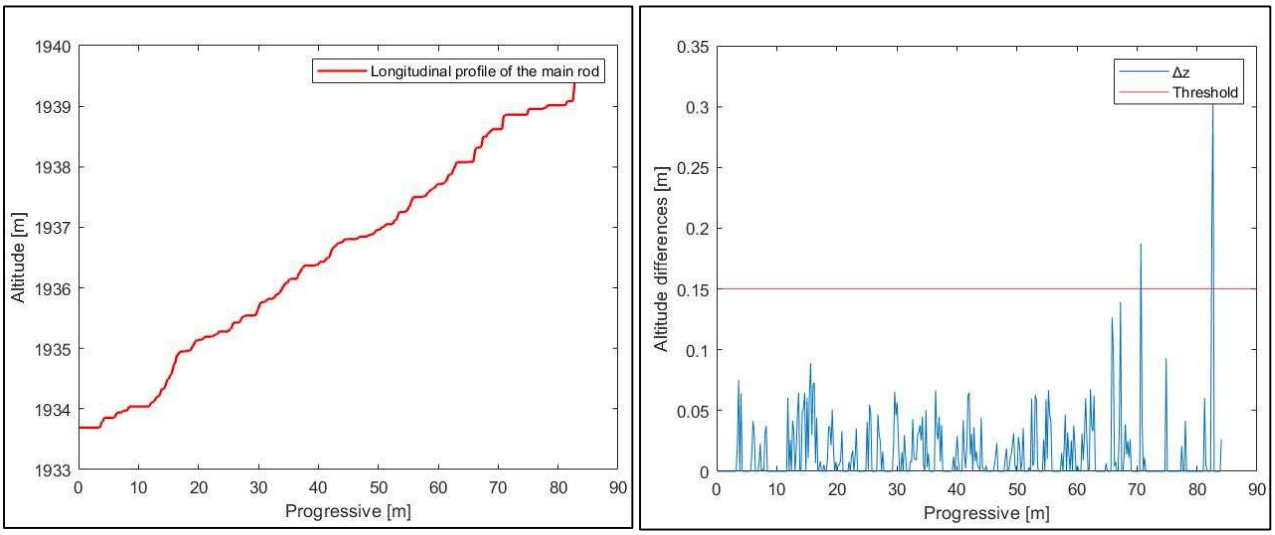

Figure 146: On the left side the longitudinal profile of the section of "Ponte downstream" upstream of the first bridge on the right side the steps along the longitudinal profile

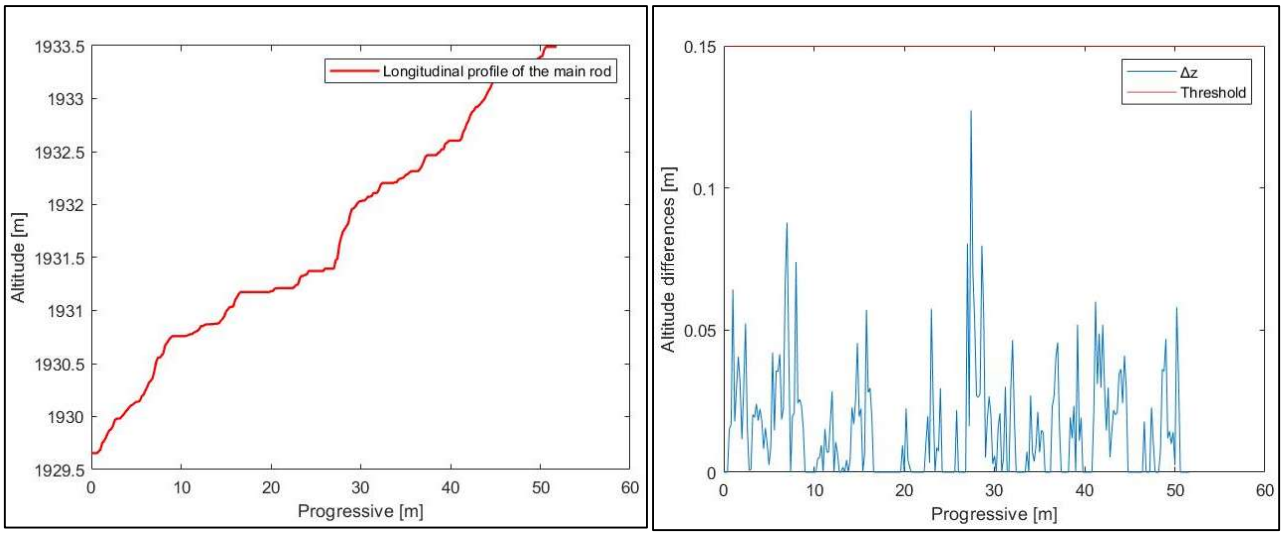

Figure 147: On the left side the longitudinal profile of the "Bridge downstream" section between the two bridges, on the right side the dips along the longitudinal profile

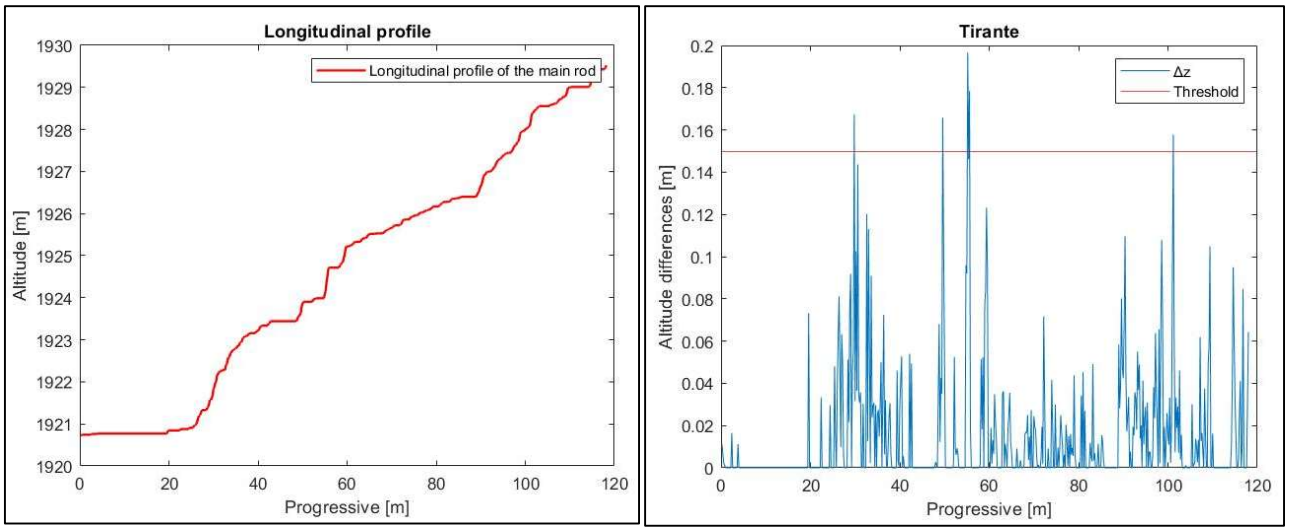

Figure 148: on the left side the longitudinal profile of the last section of "Ponte downstream", right side the steps along the longitudinal profile

Place	Slope	Mean Step Spacing (MSS) [m]	Δx [cm]	Δz [cm]	N°Step
upstream of the first bridge	0.07	30	20	15	3
between the two bridges	0.07	/	20	15	0
last section	0.07	24	20	15	5

Table 38: N° of step at "Principale Crocefisso upstream" for a prescribed Threshold value

This area presents two problems, here listed:

- Distortion of the DEM in the upstream part of the first bridge;
- Problems with the definition of the lowest pixel and thus on the determination of the main drainage profile of the stream due to riffles, long water jets, trees, and boulders fallen into the riverbed.

These problems have caused an overcount of steps. In fact, 4 extra steps have been counted, but 3 present steps were not detected.

Figure 149: On the left side an example of extra points due to distorsion of DEM on "Ponte Downstream", while on the rigth part a missing point

6.5.2. Ponte Upstream

The totality of the model consists of 117 photos, processed into 2 chunks by separating the area along the main drainage direction of the stream. The chunks will then be merged to represent an area of 9'760 m^2.

The sparse cloud (Fig.150) and related survey parameters (Tab.39) are shown below.

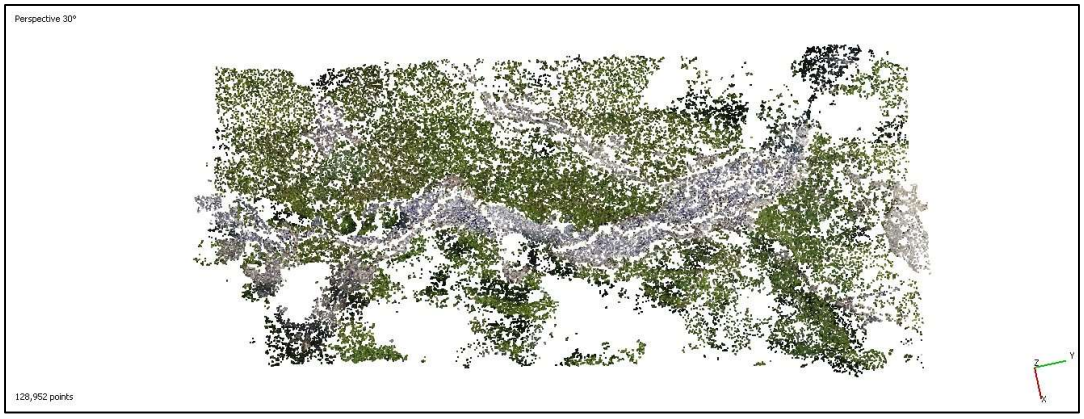

Figure 150: Sparse Cloud of "Ponte upstream"

Resolution	5280x3956	Tie points	128'952
Flight height [m]	45.1	Projections	421'301
Pixel size [um]	3.28x3.28	Reprojection error	0.591 pixel

Table 39: Sparse Cloud of "Ponte upstream" parameters

From the optimization of the alignment, the accuracy of the survey is achieved:

Figure 151: GCP locations and error estimates of "Ponte upstream".
Z error is represented by ellipse color. X, Y errors are represented by ellipse shape.
Estimated GCP locations are marked with a dot or crossing.

Count	X error [cm]	Y error [cm]	Z error [cm]	XY error [cm]	Total [cm]
9	1.30364	2.50746	1.47815	2.8261	3.18932

Table 40: Control points RMSE of "Ponte upstream".
X - Easting, Y - Northing, Z - Altitude.

Count	X error [cm]	Y error [cm]	Z error [cm]	XY error [cm]	Total [cm]
5	3.13411	1.10439	2.7816	3.32299	4.33354

Table 41: Check points RMSE of "Ponte upnstream".
X - Easting, Y - Northing, Z - Altitude.

This is followed by the restitution of the dense cloud composed of 127'397'953 points, the mesh composed of 1'525'478 vertices and 3'049'589 faces, on which the texture in Fig. 154 was laid.

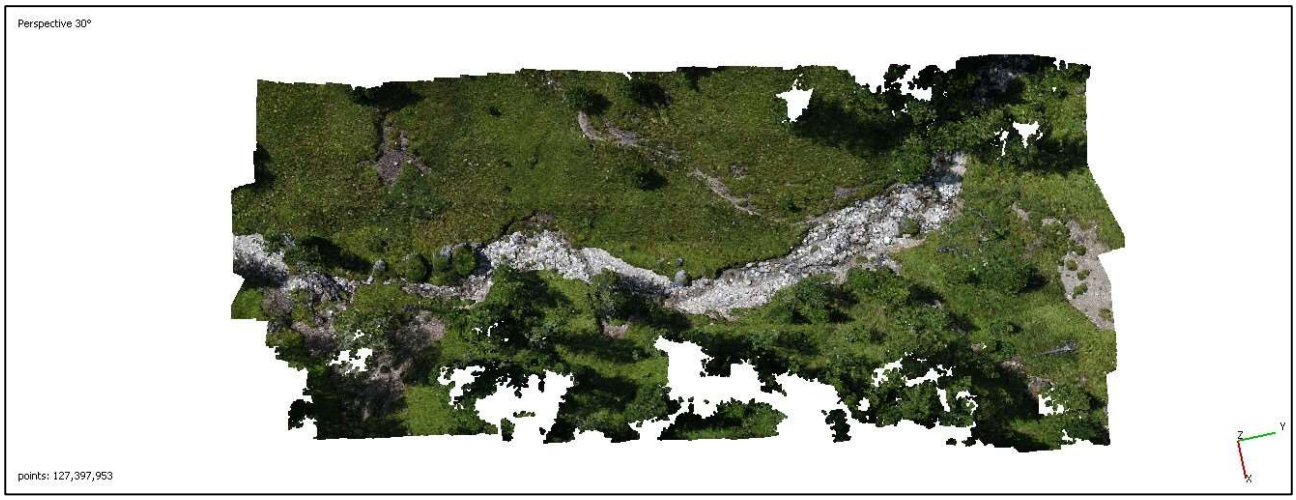

Figure 152: Dense Cloud of "Ponte upstream"

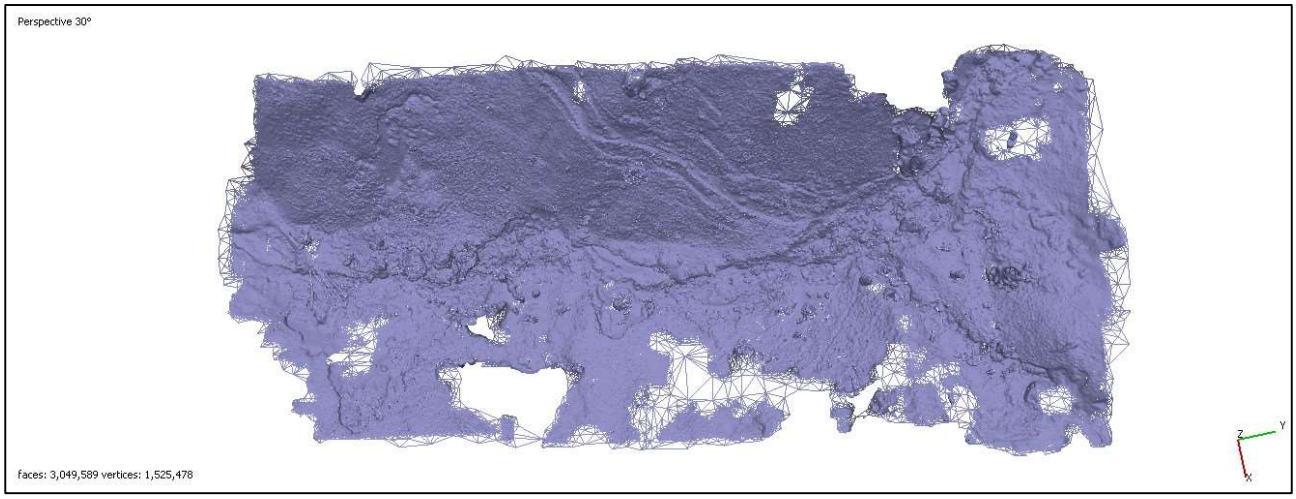

Figure 153: Mesh of "Ponte upstream"

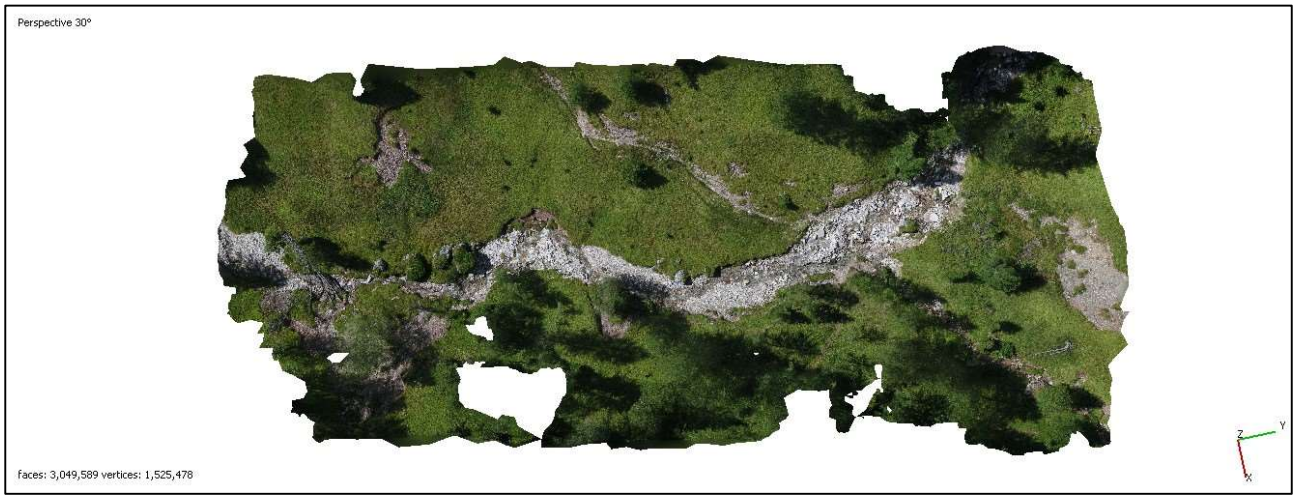

Figure 154: Texture of "Ponte upstream"

Fig. 155 shows the Orthomosaic representing “Ponte upstream” with ground resolution of 6.85 mm/pixel, which provides information on the status of the stream on 08/26/22. The Orthomosaic revealed the presence of water, the riverbed, and the pattern followed by the stream; also clearly visible are the areas around the watercourse i.e., the slope covered by conifers and the slope presided over by tall and dense grass.

In Fig. 157 the DEM made at a resolution of 1.37 cm/pixel is presented, from which visual feedback of the distribution of elevations within the survey area can be obtained. Fig. 157 indicates how the elevation distribution is very heterogeneous in the upstream area, having elevation values between the green and yellow range of the DEM legend. The stream bed is clearly distinguishable being in a more depressed position. Moreover, it is evident how the stream, especially in the downstream part, develops within steep slopes; in fact, in Fig. 156 the contour lines are very close.

On the basis of the cartographic data within the “.tiff file” of the DEM, it was also possible to reconstruct the contour lines of the area shown in Fig. 156 with 2 m pitch and the hydrographic map in Fig. 158.

Figure 155: Orthomosaic of "Ponte upstream" with ground resolution di 6.85 mm/pixel

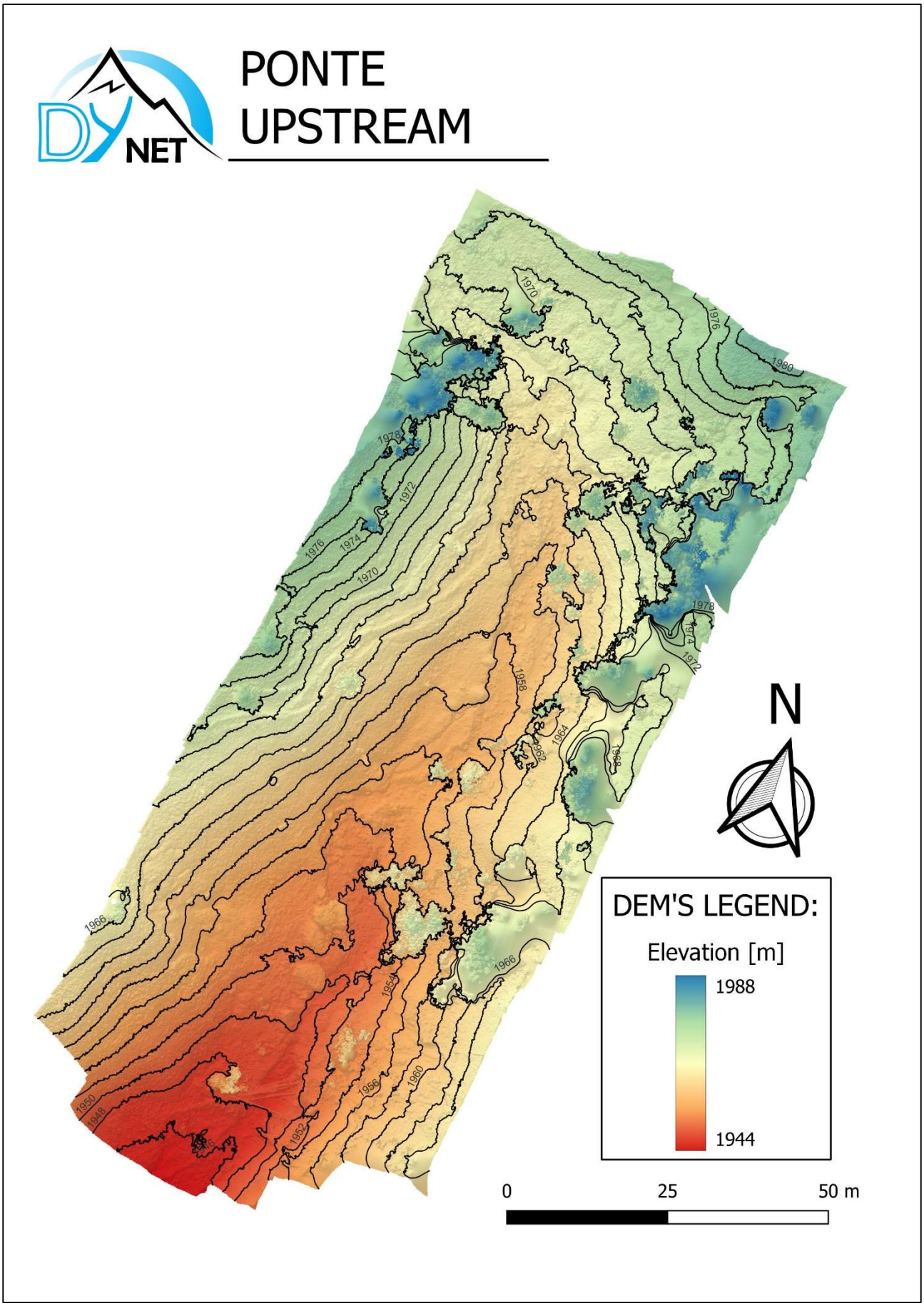

Figure 156: Contour lines of "Ponte upstream" with step of 2m

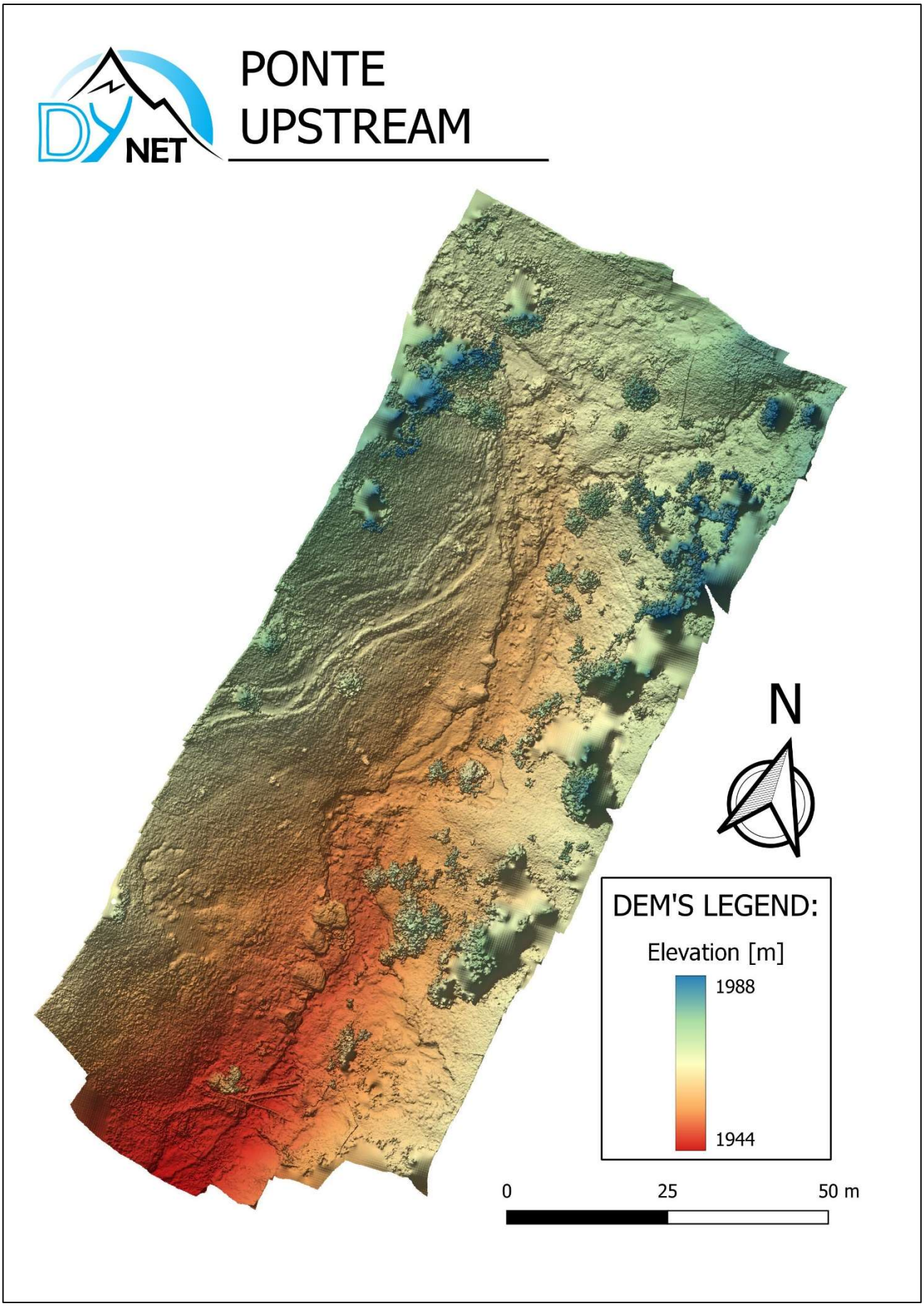

Figure 157: DEM of "Ponte upstream" with resolution of 1.37 cm/pixel

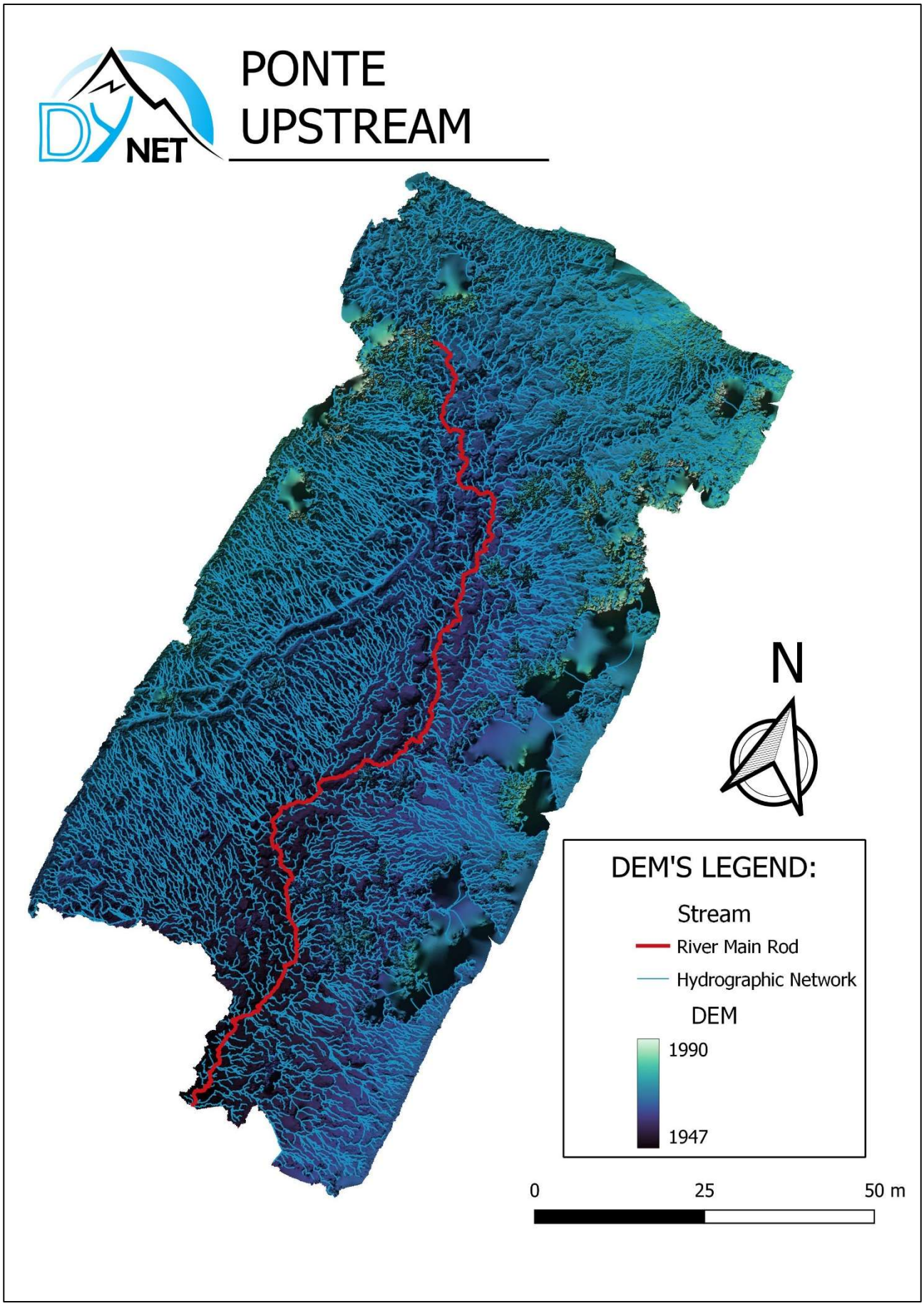

Figure 158: Hydrographic map of "Ponte upstream"

Fig. 158 is only a simplification of the basin and drainage network of "Ponte Upstream", as these data are limited to drone aerophotogrammetric acquisitions, and the dense vegetation due to the summer season in combination with the numerous conifers distorts the ground drainage network. In any case Fig. 158 provides useful information regarding the location of the main rod, i.e., where the main runoff direction is located, and the areas around it that contribute to the runoff.

Perimeter and area of the basin are reported in Tab. 42.

Area [m^2]	Perimeter [m]
7'934	748

Table 42: "Ponte upstream" Basin Statistics

Finally, thanks to the elevation data of the main rod, the elevation profile was obtained and then modified with a "pit filling" algorithm. Assuming the step can be identified by elevation of drop of 15 cm (or more) within a long distance Δx of 20 cm, the number of jumps was obtained (Fig. 159). I report in Tab. 43 the characteristics of the longitudinal profile of "Ponte downstream".

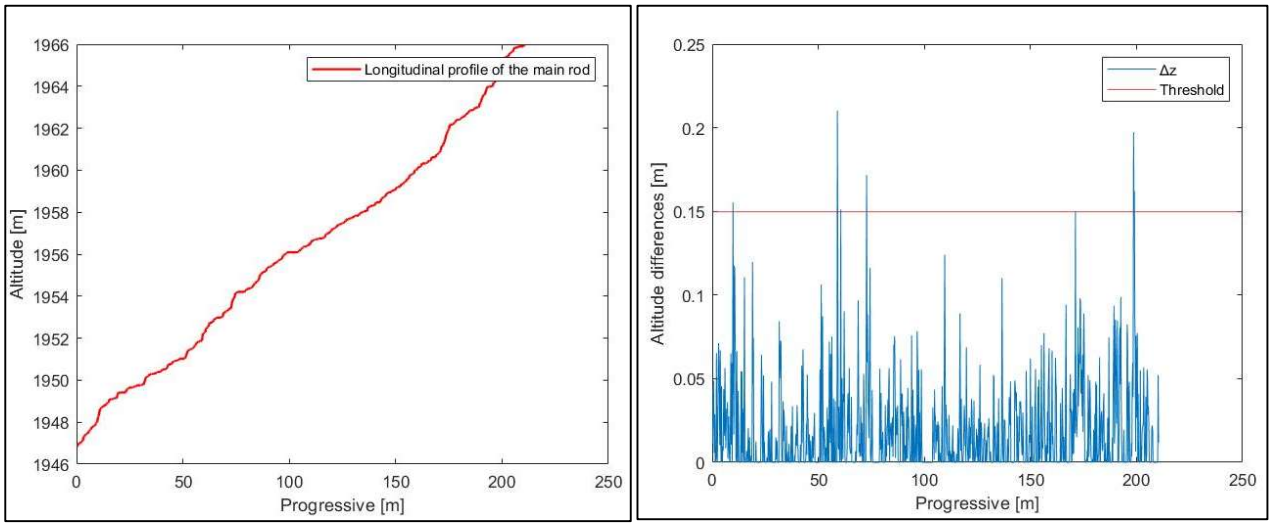

Figure 159: On the left side the longitudinal profile of the section of "Ponte upstream" upstream on the right side the steps along the longitudinal profile

Slope	Mean Step Spacing (MSS) [m]	Δx [cm]	Δz [cm]	N°Step
0.09	26.3	20	15	8

Table 43: N° of step at "Ponte upstream" for a prescribed Threshold value

In the case of "Ponte upstream" the algorithm worked quite well except for a riffle that gives 2 extra points.

Figure 160: Riffle on "Ponte upstream"

6.6. Slope VS Mean Step Spacing

Here, the relationship between the frequency of steps and the mean slope of the reach is analyzed. Tab. 44 summarize the various parameters extrapolated from the Matlab algorithm and reported in the previous chapters.

In Tab.44, the data of various main bridge sub-sections have been combined as follows:

- by summing the number of steps,
- by taking a weighted average over the length to have a single value of slope
- by calculating the mean step spacing over the total length of the section (Upstream+Downstream)

Place	Slope	Mean Step Spacing (MSS) [m]	Δx [cm]	Δz [cm]	Steps	ln(Slope)	ln(MSS) [m]
AFFLUENTE 3 UPSTREAM	0.08	230	10	15	1	-2.48	5.44
AFFLUENTE 3 DOWNSTREAM	0.18	13.63	10	15	11	-1.70	2.61
AFFLUENTE 1	0.29	2.93	10	15	105	-1.24	1.08
PRINCIPALE CROCEFISSO UPSTREAM	0.13	8.86	20	15	22	-2.04	2.18
PRINCIPALE CROCEFISSO DOWNSTREAM	0.18	5.66	20	15	53	-1.70	1.73
PRINCIPALE PONTE	0.08	27.29	20	15	17	-2.51	3.31
METEO VALLE	0.06	230	20	15	1	-2.81	5.44

Table 44: Characteristics of all streams

Fig. 161 shows the mean step spacing as a function of the mean slope in a log-log plot and allows a visible trend in the arrangement of the points to be detected. As the mean step distance increases, there is a decrease in the slope value. This refers back to Judd (1964) who states that there is an inverse relationship between the slope of the section and mean step spacing. In support of the validity of the inverse relationship between mean step spacing and slope, the linear correlation coefficient is also shown in Fig. 161, which turns out to be 0.79.

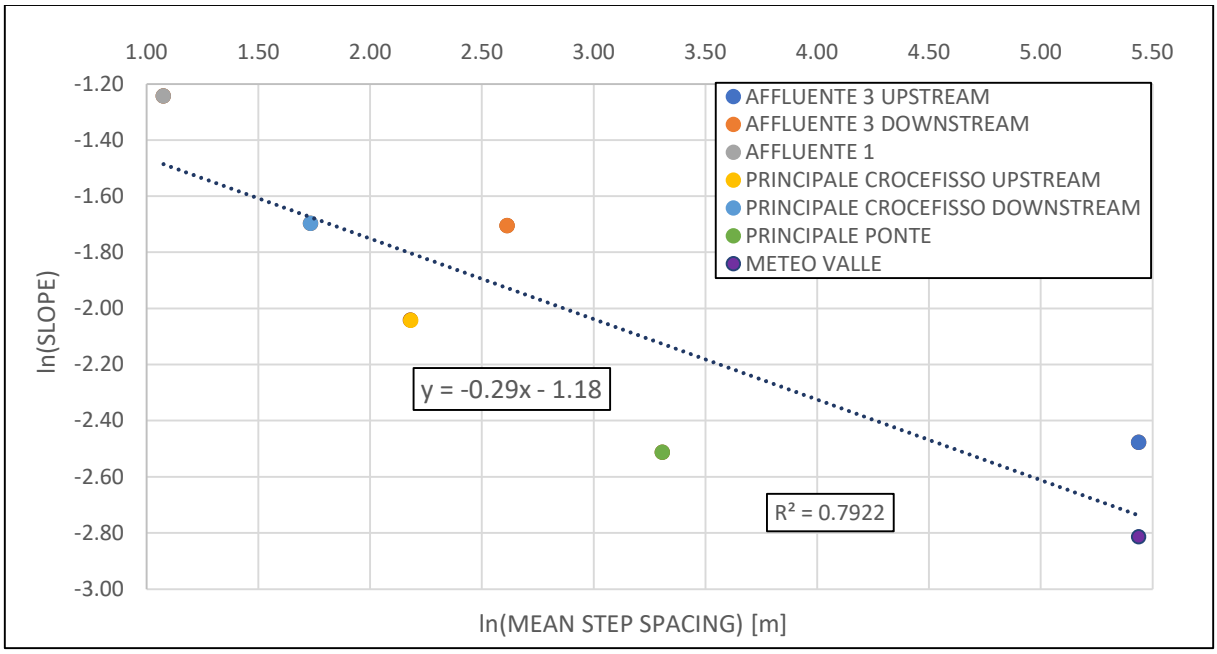

Figure 161: Diagram ln(slope) VS ln(Mean Step Spacing) for all streams

7. Conclusion and Future Developments

Through the succession of survey campaigns carried out within the Valfredda basin, with the combination of GNSS and SAPR methodology, it was possible to determine the morphological characteristics of the analyzed areas such as elevations, slopes, profiles and presence of jumps in the stream and to create graphical elaborations to support and supplement these observations. Where possible, additional data were extracted such as: drainage area, perimeter, and max/min/average elevation; data, however, to be considered with caution, since they are limited to drone acquisitions and extracted as extra information from the workflow propaedeutic to the determination of the main rod in the various considered segments of the stream.

The high accuracy achieved in the various models is further evidence of the robustness of the methodologies used in the field, which led, under optimal conditions, to errors of less than 5 cm at all times. However, it is important to emphasize that mountain environments and the stream beds are ever changing systems, and these accuracies should be referred to the date of the survey.

As for the identification of the jumps, 210 steps were detected in the 5 reaches analyzed. The mean spacing of steps decreased with the slope in accordance with Judd (1964). The procedure of step identification has various issues related to the resolution of the DEM, interferences and the morphological complexity of mountain streams.

A fairly recurrent adversity within the survey phase was the placement of markers, which being printed on sheets of paper could not be well placed on the ground in the presence of tall grass. This issue is not to be underestimated, in fact "Affluent 1" has recorded the highest error rate in GCPs and QCPs for this exact reason.

In order to limit the error that results from the suboptimal placement of markers, within the survey area, one could think of using markers printed on more rigid materials (plastic, wood or iron for example). This would allow the markers to be located solidly on the ground and thus making possible the correct positioning of the GPS antenna. To be considered, however, is that the change of material affects the price, and given the amount of GCP and QCP used, it is to be seen whether the increase in price is worth the increase in final accuracy. An alternative to this could be provided by markers located on tripods, but they may be even more expensive.

As for the procedure undertaken in QGIS, which is used to extract the main rod data, additional optimization and extraction algorithms could be integrated to improve network extraction, or an alternative route could be taken in ArcGIS via TAUDEM for obtaining such data. To be able to extract a more realistic drainage network, it would be optimal to perform the photogrammetric flight at the end of the thawing season. In fact, in this season, the vegetation is less dense, which makes it easier to determine more accurately the deepest pixel for drainage network extraction purposes. However, the drainage network remains a data to be considered with caution, being limited to the portion of the basin surveyed by the drone. Carrying out the field operations during other seasons would also facilitate the GPS surveys, as with low vegetation there is a chance to place the markers in a more distributed way, without having to change the material on which they are printed.

The results obtained in this thesis are to be strictly referred to the year in which the survey operations were carried out; this can set the basis for future studies on the morphological evolution of the basin, through future survey campaigns that can be compared with those that took place in 2022 and if desired also compared with the data acquired in 2018, pre-VAIA, by selecting either the portions of the DEM of the affected areas or by trying to re-extract the data from the sparse cloud. Comparison with the 2018 Data could provide information regarding the morphological changes of the basins as consequence of extreme events.

8. Reference

- Ambrogio Manzino, Fabio di Marco, *Fotogrammetria Diretta da Drone per la Misura e il Monitoraggio delle Frane,* Politecnico di Torino, Corso di Laurea Magistrale in Ingegneria Civile, 2019-2020.

- Andrea Burbello, Andrea Menin, *Metodologie GNSS per il Monitoraggio di Dissesti Idrogeologici, "Caso Studio: Frana di Rovegliana (VI)"*, Department of Civil, Environmental and Architectural Engineering, University of Padova, Luglio 2020, pg. 5-20.

- Carozzani A., Botter G., Durighetto N., *Quantifying the role of steps in carbon dioxide emissions in a mountain headwater stream"*, Department of Civil, Environmental and Architectural Engineering, University of Padova, 2020-2021

- Chartrand S., Jellinek M., Whiting P., and Stamm J., *Geometric scaling of step-pools in mountain streams: Observations and implications,* (2011).

- Chin A., *On the origin of step–pool sequences in mountain stream* (1999).

- Chin A. and Wohl E.*, Toward a theory for step pools in stream channels. Progress in Physical Geography*, (2005).

- Chin A. and Phillips D. J., *The self-organization of step-pools in mountain streams,* (2007)

- Church M. and Zimmerman A., *Form and stability of step-pool channels: Research progress. Water Resources Research,* (2007).

- Curran C. J. And Wilrock R. P., *Characteristic dimensions of the step-pool bed configuration: An experimental study,* (2005).

- Durighetto N., Vingiani F., LE Bertassello, Camporese M., Botter G., *Dinamica della rete di drenaggio intrastagionale in un bacino idrografico delle Alpi italiane,* Erc Dynet, 23 Marzo 2020.

- D'Agostino V. and Lenzi M. A. *Origine e dinamica della morfologia a gradinata (step pool) nei torrenti alpini ad elevata pendenza,* (1997).

- Grant G., Swanson F., and Wolman M., *Pattern and origin of stepped-bed morphology in high-gradient streams, western cascades, oregon.* (1990).

- Judd, Harl Elmer, *A study of bed characteristics in relation to flow in rough, high-gradient, natural channels,* (1964)

- Marco Pinto, Antonio Zanutta, Marco Dubbini, *Rilievo Fotogrammetrico da Drone per la Generazione di Modelli Termici di Porzioni di Territorio,* Alma Mater Studiorum, University of Bologna, Department of Civil, Chemical, Environmental and of Material, 2016.

- Massimo Micieli, *Aerofotogrammetria con i Droni, "Mappatura e modellazione 3D del Territorio con tecniche aerofotogrammetriche da SAPR (Sistemi Aeromobili a Pilotaggio Remoto)"*, Dario Flaccovio Editore, Marzo 2019, pg.17-28/63-69/81-86/108-119.

- Massimo Fabris, *Slides of Land Surveying and Geographical Information System (GIS)*, 2020-2021.
- Montgomery D. and Buffington J., *Channel-reach morphology in mountain drainage basins. Geological Society of America Bulletin,* 1997
- Richardson K. And Carling P. A., *Morphology and origin of alluvial step-pools: A synthesis of experimental and field data from formative flows,* (2021).
- Turcotte B. and Morse B. A, *Global River ice classification model. Journal of Hydrology*, (2013).
- Wertz J. B., *The flood cycle of ephemeral mountain streams in the southwestern united states,* (1966).
- < Erc Dynet> [Online]. Link: *https://www.erc-dynet.it/* (consulted July 2022).
- <Asi, Agenzia Spaziale Italiana> [Online]. Link: *https://www.asi.it/tlc-e-navigazione/galileo/#:~:text=Galileo%2C%20interamente%20concepito%20per%20usi,una%20precisione%20mai%20raggiunta%20prima.* (consulted July 2022).
- < CIRGEO-Centro Interdipartimentale di Ricerca Geomatica, Unipd> [Online]. Link: *https://samv.elearning.unipd.it/pluginfile.php/35101/mod_resource/content/1/Corso%20GPS%20x%20Topografia%202014-2015.pdf* (consulted July 2022).
- <Manuale Utente di QGIS> [Online]. Link: *https://docs.qgis.org/3.22/it/docs/user_manual/preamble/foreword.html* (consulted July 2022).
- <Agisoft Metashape> [Online]. Link: *https://www.agisoft.com/* (consulted June 2022).
- <Agisoft Metashape User Manual> [Online]. Link: *https://www.agisoft.com/pdf/metashape-pro_1_7_en.pdf* (consulted June 2022).
- <DJI> [Online]. Link: *https://www.dji.com/it* (consulted June 2022).
- <LGS GNSS Comparison Chart> [Online]. Link: *https://www.metrica.gr/images/downloads/Leica-LGS-GNSS-Comparison-Chart-GS07-LR.pdf* (consulted July 2022).
- <Agordino Dolomiti> [Online]. Link: *https://www.agordinodolomiti.it/index.php/cosa-vedere/natura/valfredda/* (consulted July 2022).
- <3d metrica, "Target Artificiali per il rilievo Aerofotogrammetrico"> [Online]. Link: *https://3dmetrica.it/target-artificiali-rilievo-aerofotogrammetrico/* (consulted August 2022).
- <3d metrica, "Quanto è preciso un rilievo col drone"> [Online]. Link: *https://3dmetrica.it/precisione-di-un-rilievo-con-il-drone/* (consulted August 2022).
- <3d metrica, "DTM VS DSM VS DEM"> [Online]. Link: *https://3dmetrica.it/dtm-dsm-dem/* (consulted August 2022).

- <3d metrica, “Una foto dall’alto non è un Ortofoto”> [Online]. Link: *https://3dmetrica.it/ortofoto/* (consulted August 2022).

- <3d metrica, “Aerofotogrammetria di terreni inclinati”> [Online]. Link: *https://3dmetrica.it/aerofotogrammetria-su-terreni-inclinati/* (consulted August 2022).

- <professione3d, “GCP e QCP”> [Online]. Link: *https://www.professione3d.it/2020/02/06/gcp-e-qcp/* (consulted August 2022).

- <MAULab-Politecnico di Bari> [Online]. Link: *https://www.youtube.com/playlist?list=PLuD7r-nekk9ZJpMM_jwvSPNWC4ae46nBp* (consulted July 2022).

- <Paolo Corradeghini, 3dmetrica, “Agisoft Metashape - Inserisci i punti di controllo e verifica l'accuratezza“> [Online]. Link: *https://www.youtube.com/watch?v=8BpOfscNYn4&ab_channel=PaoloCorradeghini* (consulted July 2022).

- <Paolo Corradeghini, 3dmetrica, “Agiosft Metashape - Ottimizza l'allineamento con i punti di controllo”> [Online]. Link*: https://www.youtube.com/watch?v=-mqTBSBEjxQ&ab_channel=PaoloCorradeghini* (consulted July 2022).

- <Paolo Corradeghini, 3dmetrica, “Agisoft Metashape - Posiziona i marker nelle foto, bandiere e scorciatoie”> [Online]. Link*: https://www.youtube.com/watch?v=m-OpWZNCjtY&ab_channel=PaoloCorradeghini (*consulted June 2022).

- <Paolo Corradeghini, 3dmetrica, ”Agisoft Metashape - Genera il DEM e crea le curve di livello” > [Online]. Link: *https://www.youtube.com/watch?v=4_FyIwDSd7A&ab_channel=PaoloCorradeghini* (consulted June 2022).

- <Paolo Corradeghini, 3dmetrica, “Agisoft Metashape - Crea una mesh dalle mappe di profondità“> [Online]. Link: *https://www.youtube.com/watch?v=9Kt_lTAYrD4&ab_channel=PaoloCorradeghini* (consulted June 2022).

- <Paolo Corradeghini, 3dmetrica, “Agisoft Metashape - Genera la texture“> [Online]. Link: *https://www.youtube.com/watch?v=KBQXDodhh0w&ab_channel=PaoloCorradeghini* (consulted June 2022).

- <Paolo Corradeghini, 3dmetrica, Agisoft Metashape - Texture, metodi di fusione e risoluzione”> [Online]. Link: *https://www.youtube.com/watch?v=gRDUxxZvw6s&t=763s&ab_channel=PaoloCorradeghini* (consulted June 2022).

- <Paolo Corradeghini, 3dmetrica, “Agisoft Metashape - Ortofoto ed impostazioni“> [Online]. Link: https://www.youtube.com/watch?v=ExF3xygWCUU&t=1358s&ab_channel=PaoloCorradeghini (consulted June 2022).

- <Paolo Corradeghini, 3dmetrica, “Agisoft Metashape – esportare l’Ortomosaico“> [Online]. Link: *https://www.youtube.com/watch?v=xImwRSoE1V0&t=3s&ab_channel=PaoloCorradeghini* (consulted June 2022).

- <Paolo Corradeghini, 3dmetrica, "QGIS - DEM migliora la vista con la modalità Hillshade"> [Online]. Link: *https://www.youtube.com/watch?v=kOn7KXTUIRI&ab_channel=PaoloCorradeghini* (consulted June 2022).

- <Manuale di MATLAB> [Online]. Link: *http://www.attuariale.eu/MatFin/Mini%20Manuale%20Matlab%201.0.pdf* (consulted August2022).

- <MATLAB> [Online]. *Link: https://it.mathworks.com/products/matlab.html* (consulted August2022).

- <Lezioni di QGIS per l'ingegneria idraulica> [Online]. Link: *https://www.youtube.com/watch?v=fcObVecB2Hk&list=PLBdIETf5FiOMqmj-8ZNW-85hrcEJwREvn&ab_channel=SoluzioniIngegneristiche* (consulted August2022).

9. Appendix

```
clear all
close all
clc

% Name of the file to be processed
filename = "quote20.csv";

% threshold on the difference [m]
q = 0.15;


%####################
%####################

% import
df = readtable(filename);
z0 = table2array(df(2:height(df),"clipBasin"));
x0 = table2array(df(2:height(df),"tratto"));
est = table2array(df(2:height(df),"x"));
nord = table2array(df(2:height(df),"y"));

% x axis
x = cumsum(x0);

% correct quota
for i = 1:length(z0)-1
    if z0(i+1) < z0(i)
        z0(i+1) = z0(i);
    end
end

% plot longitudinal profile
figure(1)
plot(x,z0, 'red', 'LineWidth',1.4)
title('Longitudinal profile')
xlabel('Progressive [m]')
ylabel('Altitude [m]')
legend('Longitudinal profile of the main rod')

% build difference in quota
z1 = z0(1:length(z0)-1);
z2 = z0(2:length(z0));
dz = z2-z1;
% difference in length
x1 = x(1:length(x0)-1);
x2 = x(2:length(x0));
dx = x2-x1;

% slope
slope = mean(dz./dx);

% plot tirante
figure(2)
plot(x(1:length(x)-1),dz)
hold on
yline(q,'red')
title('Tirante')
xlabel('Progressive [m]')
```

```
ylabel('Altitude differences [m]')
legend('?z', 'Threshold')

% check jump counts
counts = sum(abs(dz)>=q);

% jump coordinates
fprintf("Coord. salti\n")
jump_positions = double.empty(0);
for i= 1:length(z0)-1
    if dz(i)>=q
        fprintf(string(est(i)) +" "+ string(nord(i))+ " " + string(z0(i))+"\n");
        jump_positions = [jump_positions; x(i)];
    end
end

% evaluate jump distances
jump_distance = double.empty(0);
for i = 1:length(jump_positions)-1
    jump_distance = [jump_distance; jump_positions(i+1)-jump_positions(i)];
end

% average jump distance
mean_jump_dist = mean(jump_distance);
if isnan(mean_jump_dist)
    mean_jump_dist = "not defined";
end

if isnumeric(mean_jump_dist)
    % scatterplot
    figure(3)
    plot(mean_jump_dist,slope,'-o')
    hold on
    %title('Title')
    xlabel('Mean jump distance [m]')
    ylabel('Slope')
end

% output
fprintf("Numero di differenze di quota maggiori o uguali a " + string(q) + ...
    " m: " + string(counts) + " su " + string(height(dz)) + ...
    "\nPendenza: " + string(slope) + ", frequenza di salti: " + mean_jump_dist +
...
    "\n File analizzato: " + filename + "\n")
```